Optimizing a Transition Edge Sensor detector system for low flux infrared photon measurements at the ALPS II experiment

Dissertation

zur Erlangung des Doktorgrades
an der Fakultät für Mathematik,
Informatik und Naturwissenschaften
Fachbereich Physik
der Universität Hamburg

vorgelegt von

José Alejandro Rubiera Gimeno

aus

Havanna, Kuba

Hamburg

2024

Hiermit erkläre ich an Eides statt, dass ich die vorliegende Dissertationsschrift selbst verfasst und keine anderen als die angegebenen Quellen und Hilfsmittel benutzt habe.

I hereby declare, on oath, that I have written the present dissertation by my own and have not used other than the acknowledged resources and aids.

Hamburg, den 10. Juni 2024 José Alejandro Rubiera Gimeno

Gutachter der Dissertation:	Dr. Axel Lindner Prof. Dr. Erika Garutti
Zusammensetzung der Prüfungskommission:	Prof. Dr. Florian Grüner Prof. Dr. Erika Garutti Dr. Andreas Ringwald Prof. Dr. Johannes Haller Dr. Axel Lindner
Vorsitzender der Prüfungskommission:	Prof. Dr. Florian Grüner
Datum der Disputation:	25. Juli 2024
Vorsitzender des Fach-Promotionsausschusses Physik:	Prof. Dr. Markus Drescher
Leiter des Fachbereichs Physik:	Prof. Dr. Wolfgang J. Parak
Dekan der Fakultät MIN:	Prof. Dr.-Ing. Norbert Ritter

ABSTRACT

This thesis investigates the optimization of a Transition-Edge Sensor (TES) for the Any Light Particle Search II (ALPS II) experiment. The ALPS II experiment searches for axions and axion-like particles, which are predicted by several beyond-standard model theories and are good candidates for dark matter. The TES is a superconducting detector sensitive to temperature-induced resistance changes. For ALPS II, the TES must be able to detect low-energy photons (1.165 eV) with high efficiency, good energy resolution and extremely low background rates in the order of one 1064 nm photon-like event every two days. Towards the goal of reducing the background rate, this thesis focuses on the understanding of the background and the optimization of the data analysis in an effort to reject them.

A two-fold approach was developed to simulate the background observed when the TES is decoupled from the optical fiber used in the TES characterization. On the one hand, a Geant4-based framework was built to compute the energy deposition produced by muons from cosmic rays and radioactivity from the zirconia fiber sleeve used to couple the detector to the experimental setup. On the other hand, a COMSOL Multiphysics simulation was designed to model the TES physics. This was used to assess the effects of the energy depositions on the TES. The radioactivity in the zirconia was identified as the dominant intrinsic background source.

When the optical fiber is coupled to the TES, an additional background component appears with respect to the aforementioned, predicted to be composed of Black Body Radiation (BBR). A framework was developed to simulate the BBR and compute the expected background rates in the TES. The uncertainties in the simulation results were mainly given by the bending of the optical fiber used to transmit the light to the TES. However, the importance of fiber bending for the rejection of low-energy BBR photons was demonstrated. Furthermore, this simulation demonstrated that BBR-induced background could be mitigated by enhancing the TES energy resolution.

Consequently, another simulation tool was developed in order to understand the effect of the baseline noise on the TES energy resolution. The TES signal was modeled as the superposition of a non-distorted 1064 nm pulse and the baseline noise. Using this method, the obtained energy resolution was equal to the one computed from the measured data. This demonstrated that the energy resolution in the TES system is mainly governed by the electronic noise and not by variations in the photon absorption process in the TES.

Finally, a frequency domain-based analysis was implemented to optimize the analysis and improve the energy resolution. Combining this analysis with the choice of the pulse height to describe the energy of the photon incident in the TES allowed an overall enhancement of the energy resolution by a factor of 2. Additionally, a pulse-finding algorithm based on signal deconvolution was implemented to determine the arrival times of pulses and the identification of pile-up. This algorithm improved fitting procedure stability and speed and enabled the rejection of false triggers and the identification of pulses with energies as low as 0.3 eV. The joint analysis optimization reduced the measured extrinsic background rates in the 1064 nm photon signal region by one order of magnitude.

ZUSAMMENFASSUNG

Diese Arbeit befasst sich mit der Optimierung eines Transition-Edge-Sensors (TES) für das Any Light Particle Search II (ALPS II)-Experiment. Das ALPS II-Experiment sucht nach Axionen und Axion-ähnlichen Teilchen, die von mehreren über das Standardmodell hinausgehenden Theorien vorhergesagt werden und gute Kandidaten für die dunkle Materie sind. Der TES ist ein supraleitender Detektor, der empfindlich auf temperaturbedingte Widerstandsänderungen reagiert. Für ALPS II muss der TES in der Lage sein, Photonen niedriger Energie (1.165 eV) mit hoher Effizienz, guter Energieauflösung und extrem niedrigen Untergrundraten in der Größenordnung von einem 1064 nm photonähnlichen Ereignis alle zwei Tage zu erkennen. Mit dem Ziel, die Untergrundrate zu reduzieren, konzentriert sich diese Arbeit auf die Untersuchung des Untergrunds und die Optimierung der Datenanalyse, um diesen zu unterdrücken.

Es wurde ein zweiteiliger Ansatz entwickelt, um den Untergrund zu simulieren, der gemessen wird, wenn der TES von der bei der TES-Charakterisierung verwendeten optischen Faser abgekoppelt wird. Einerseits wurde ein Geant4-basiertes Modell erstellt, um die Energiedeposition durch Myonen aus kosmischer Strahlung und die Radioaktivität aus der Zirkonium-Faserhülse zu berechnen, die zur Kopplung des Detektors an den Versuchsaufbau verwendet wird. Andererseits wurde eine COMSOL-Multiphysics-Simulation entwickelt, um die TES-Physik zu modellieren. Diese wurde verwendet, um die Auswirkungen der Energiedepositionen auf den TES zu untersuchen. Dabei wurde die Radioaktivität im Zirkonium als die dominierende intrinsische Untergrundquelle identifiziert.

Wenn die optische Faser an den TES angeschlossen wird, tritt zusätzlich zur oben genannten eine Untergrundkomponente auf, die voraussichtlich aus Schwarzkörperstrahlung (BBR) besteht. Es wurde ein Modell entwickelt, um die BBR zu simulieren und die erwarteten Untergrundraten im TES zu berechnen. Die Unsicherheiten in den Simulationsergebnissen waren hauptsächlich auf die Krümmung der optischen Faser zurückzuführen, die zur Transmission des Lichts an den TES verwendet wird. Der Einfluss der Krümmung der optischen Faser auf die Ablehnung von BBR-Photonen mit niedriger Energie wurde jedoch nachgewiesen. Dar-über hinaus zeigte diese Simulation, dass der durch BBR verursachte Untergrund durch eine Verbesserung der TES-Energieauflösung reduziert werden könnte.

Daher wurde ein weiteres Simulationstool entwickelt, um die Auswirkungen des Basislinienrauschens auf die TES-Energieauflösung zu verstehen. Das TES-Signal wurde als Überlagerung eines unverzerrten 1064-nm-Pulses und des Basislinienrauschens modelliert. Mit dieser Methode war die erzielte Energieauflösung gleich der aus den Messdaten berechneten. Dies zeigte, dass die Energieauflösung im TES-System hauptsächlich durch das elektronische Rauschen und nicht durch Variationen im Photonenabsorptionsprozess im TES bestimmt wird.

Schließlich wurde eine Frequenzbereich-basierte Auswertung implementiert, um die Analyse zu optimieren und die Energieauflösung zu verbessern. Die Kombination dieser Analyse mit der Verwendung der Pulshöhe zur Beschreibung der Energie des im TES einfallenden Photons ermöglichte eine allgemeine Verbesserung der Energieauflösung um einen Faktor zwei. Zusätzlich wurde ein auf Signalentfaltung basierender Pulsfindungsalgorithmus implementiert, um die Ankunftszeiten der Pulse zu bestimmen und eine Pulsanhäufung zu identifizieren. Dieser Algorithmus verbesserte die Stabilität und Geschwindigkeit der Fits und ermöglichte das Unterdrücken falscher Trigger und die Identifizierung von Pulsen mit Energien von nur 0.3 eV. Die gesamte Optimierung der Analyse reduzierte die gemessenen extrinsischen Untergrundraten im 1064 nm-Photonensignalbereich um eine Größenordnung.

Contents

CHAPTER

1

INTRODUCTION

> La confusión está clarísima.
>
> Les Luthiers

Contents

The nature of dark matter remains one of the most intriguing questions in physics. Dark matter is estimated to constitute approximately 27 % of the universe's mass-energy composition and 85 % of the universe's mass [1]. Its presence is inferred from gravitational effects on visible matter, radiation, and the universe's large-scale structure. One effect includes the rotation curves of galaxies, which cannot be explained by the mass of visible matter alone [2], and the bending of light due to gravitational lensing observed in deep space [3].

Several particles have been proposed as candidates for dark matter, with the axions standing out due to their unique theoretical foundation. The axion theory was not initially motivated by the dark matter problem but was proposed as a solution to the strong CP problem of quantum chromodynamics (QCD). Roberto Peccei and Helen Quinn proposed a solution involving a new symmetry, now known as the Peccei-Quinn symmetry [4]. When spontaneously broken, this symmetry predicted the existence of a new particle: the axion [5]. It was named after a brand of laundry detergent since it would "clean up" the strong CP problem.

The axion was initially expected to interact at energy levels accessible to early experiments [6]. The non-detection of the axion led to the suggestion that the axion could be very light and weakly interacting [7, 8]. These characteristics make the axion an excellent candidate for dark matter. If axions exist, they could be produced in abundance during the early universe, remaining today as a cold dark matter component [9].

Axions have inspired the broader category of hypothetical particles known as axion-like particles (ALPs). ALPs are similar to axions in that they are light and weakly interacting, but they are not necessarily tied to the strong CP problem. These particles are postulated by Beyond Standard Model theories [10].

A particular approach to attempt to detect axion/ALPs is the light shining through a wall (LSW) experiment. A LSW experiment exploits the predicted ability of axions and ALPs to oscillate into photons in the presence of a magnetic field [10]. Photons are generated and directed towards a barrier that they cannot penetrate. Under the influence of a strong magnetic field, these photons would oscillate into axion/ALPs, and they would be capable of passing through the barrier due to their very weak interaction. On the other side of the barrier, these axion/ALPs can be converted back into photons in the presence of another magnetic field. The detection of these reconverted photons would prove the existence of axion/ALPs.

The Any Light Particle Search II (ALPS II) experiment refines the concept of LSW with a sophisticated setup involving lasers and optical cavities. The likelihood of converting a photon into axion/ALPs within a magnetic field, and vice-versa, is enhanced by the use of optical cavities. One of the challenges of ALPS II lies in detecting the reconverted photons, which are expected at low energies (1.165 eV) and at a very low rate (roughly one photon per day). This requires the use of a highly sensitive detector such as a Transition Edge Sensor (TES). To achieve high-significance detection, a very low background level is required.

This thesis focuses on the understanding of the different kinds of background appearing in measurements with the TES. Furthermore, in this work, the analysis of the TES data is optimized with respect to [11] towards a further reduction of the background rates. Therefore, the thesis is structured in the following way:

- The next sections in this chapter (chapter 1) expands on the topic of axions and ALPs, and briefly describes the ALPS II experiment.

- Chapter 2 will discuss the main aspects of the TES physics model and will describe the experimental setups used to measure the data analyzed in this work and the setup that might be used for ALPS II.

- Chapter 3 introduces the simulation of the TES intrinsic background, i.e. when the TES is decoupled from the optical fiber used in the TES characterization. For this, a more complicated model compared to chapter 2 is introduced. The measured background rates in the TES are compared with the simulation predictions.

- In chapter 4, the simulation of Black Body Radiation as a new population of background events with respect to chapter 3 is discussed. This population appears when the aforementioned optical fiber is coupled to the TES. Furthermore, the results of this simulation are compared to the measured background.

- The contribution of the baseline noise in the TES to the energy resolution is assessed in chapter 5. For this purpose, the TES signal is simulated, and the results are discussed.

- Finally, in chapter 6, the optimization of the analysis of the TES data is explained. The consequences for the elements discussed in previous chapters and the background rates measured with the TES are evaluated.

1.1 Axions and Axion-like particles

The strong CP problem arises from the fact that, theoretically, QCD allows a violation of CP symmetry given by the term $\mathscr{L}_{\mathrm{CP-viol}}$ described in Eq. 1.1, in the QCD Lagrangian [12].

$$\mathcal{L}_{\mathrm{CP-viol}} = \frac{\alpha_S}{8\pi}\theta G^a_{\mu\nu}\tilde{G}^{a,\mu\nu} \tag{1.1}$$

In this equation, G corresponds to the gluonic field, α_S is the strong coupling constant, and θ is an angle parameter. The effective angle $\bar{\theta} = \theta - \mathrm{argDet}[\mathcal{M}_q]$, defined after a rotation to consider the phases of the quark masses, described by $\mathcal{M}_q$, induces a neutron's electric dipole moment given by $|d_n| \sim \bar{\theta} \cdot 2 \cdot 10^{-16} e \cdot \mathrm{cm}$ [13].

The experimental upper limit $|d_n| < 1.8 \cdot 10^{-26} e \cdot \mathrm{cm}$ [14], imposes $\bar{\theta}$ to be very small: $|\bar{\theta}| < 9 \cdot 10^{-11}$. This upper limit requires fine-tuning the relation between the angle θ and the phases of the quark bare masses. This fine-tuning, unexplained by QCD, is known as the strong CP problem and was shown in [12].

The axion is an elegant solution to the strong CP problem. The proposed model involves a new $U_{PQ}(1)$ symmetry known as the Peccei-Quinn symmetry [4]. As a result, the term θ in Eq. 1.1 is transformed into $\theta \rightarrow \theta - a/f_a$, where a is the axion field and f_a is known as an "axion decay constant", related to the scale of PQ symmetry breaking. The axion field dynamically evolves and settles to a value that cancels the original θ term and effectively drives the CP-violating term to zero [15, 16]. The axion acquires mass through spontaneous symmetry breaking of the introduced Peccei-Quinn symmetry and the non-perturbative effects of QCD [17], and its mass is given by Eq. 1.2.

$$m_a^2 = \frac{m_u m_d}{(m_u + m_d)^2}\frac{m_\pi^2 f_\pi^2}{f_a^2} \tag{1.2}$$

where m_u, m_d and m_π are the masses of the up quark, down quark and the pion, respectively, and f_π is the pion decay constant. Therefore, the axion mass m_a is directly related to the axion decay constant f_a.

The two main axion models are the Kim-Shifman-Vainshtein-Zakharov (KSVZ) and the Dine-Fischler-Srednicki-Zhitnitsky (DFSZ) models, which propose different mechanisms for how axions couple to the Standard Model particles. The KSVZ axion interacts with standard model particles through an additional heavy quark that carries a PQ charge [7]. On the other hand, the DFSZ model extends the Higgs sector by including two Higgs doublets and involves a direct interaction of the axion with these Higgs fields as well as the leptons and quarks [8]. In both axion models, the mass of the axion m_a is directly proportional to its coupling to photons $g_{a\gamma\gamma}$, as shown in Fig. 1.1.

Axion-like particles (ALPs) extend the concept of the axion with a mass that does not depend on the coupling constant with photons. They can be pseudo-scalar or scalar bosons as postulated by several Beyond Standard Model theories [10]. They are strongly motivated theoretically since, in string theory, a rich spectrum of light pseudo-scalars arise [18]. Moreover, a weak coupling with standard model particles is expected. This includes, for instance, the interaction with photons and electrons, which may be described by the definition of an effective Lagrangian [17, 19].

Axions are considered excellent candidates for dark matter due to their weak interaction with ordinary matter. Based on the timing of the Peccei-Quinn symmetry breaking, two cosmological scenarios appear for dark matter models: pre-inflationary and post-inflationary. Both models provide mechanisms by which axions could constitute the dark matter density observed in the universe, as referenced in current astrophysical data [9]. Furthermore, axion and ALPs are well motivated by astrophysical observations. In the evolution of stars, several hints appear in the form of excessive cooling, not explained by stellar models [20]. For instance, studying stars on the horizontal branch in globular clusters hints at an energy loss through axion/ALP emission and gives an estimate for $g_{a\gamma\gamma} \approx 1.8 \cdot 10^{-11}$ GeV^{-1} [20]. Moreover, some studies also observe an excess in the photons arriving on the Earth with an energy higher than 1 TeV. The propagation of these photons should be highly suppressed due to their conversion to electron-positron pair. The excess of photons could be explained by their conversion to axions, which can travel long distances without interacting, and then reconversion to photons with the same energy, both happening while traveling through the extragalactic magnetic field background [21, 22].

The main mechanism exploited for the direct detection of axion/ALPs is their predicted interaction with photons through the Sikivie effect. The Sikivie effect consists of the oscillation of an axion/ALPs into a photon in the presence of a magnetic field. With this, three main categories of direct axion/ALPs detection experiment can be defined:

- Haloscopes: They are designed to detect axionic dark matter that may be present in the Milky Way's halo. Therefore, they depend on the assumption that the dark matter halo consists mainly of axions. These experiments typically use a strong magnetic field and a microwave cavity to convert axions into detectable photons through the Sikivie effect [23]. The axion-photon conversion rate within the cavity is enhanced if the cavity's resonant frequency matches the axion mass.

- Helioscopes: These experiments utilize strong magnets pointed at the Sun to convert solar axions back into X-rays, which can then be detected by X-ray detectors [23]. The concept is similar to haloscopes but targets solar axions/ALPs rather than those from dark matter. In contrast to the haloscope, this search does not require axion dark matter, although it still depends on the model of axion flux arriving from the Sun.

- LSW experiment: They represent a model-independent approach to search for axion/ALPs. In the LSW approach, a photon is converted into an ALP by interacting with a magnetic field (Primakoff effect) and vice versa (Sikivie effect) [24, 25].

The next section discusses the theoretical basis of a LSW experiment.

1.2 Light shining through a wall experiment

This section briefly discusses the theoretical description of LSW experiments as in [27]. The coupling of the ALP field ϕ to photons at low energies can be described by an effective Lagrangian:

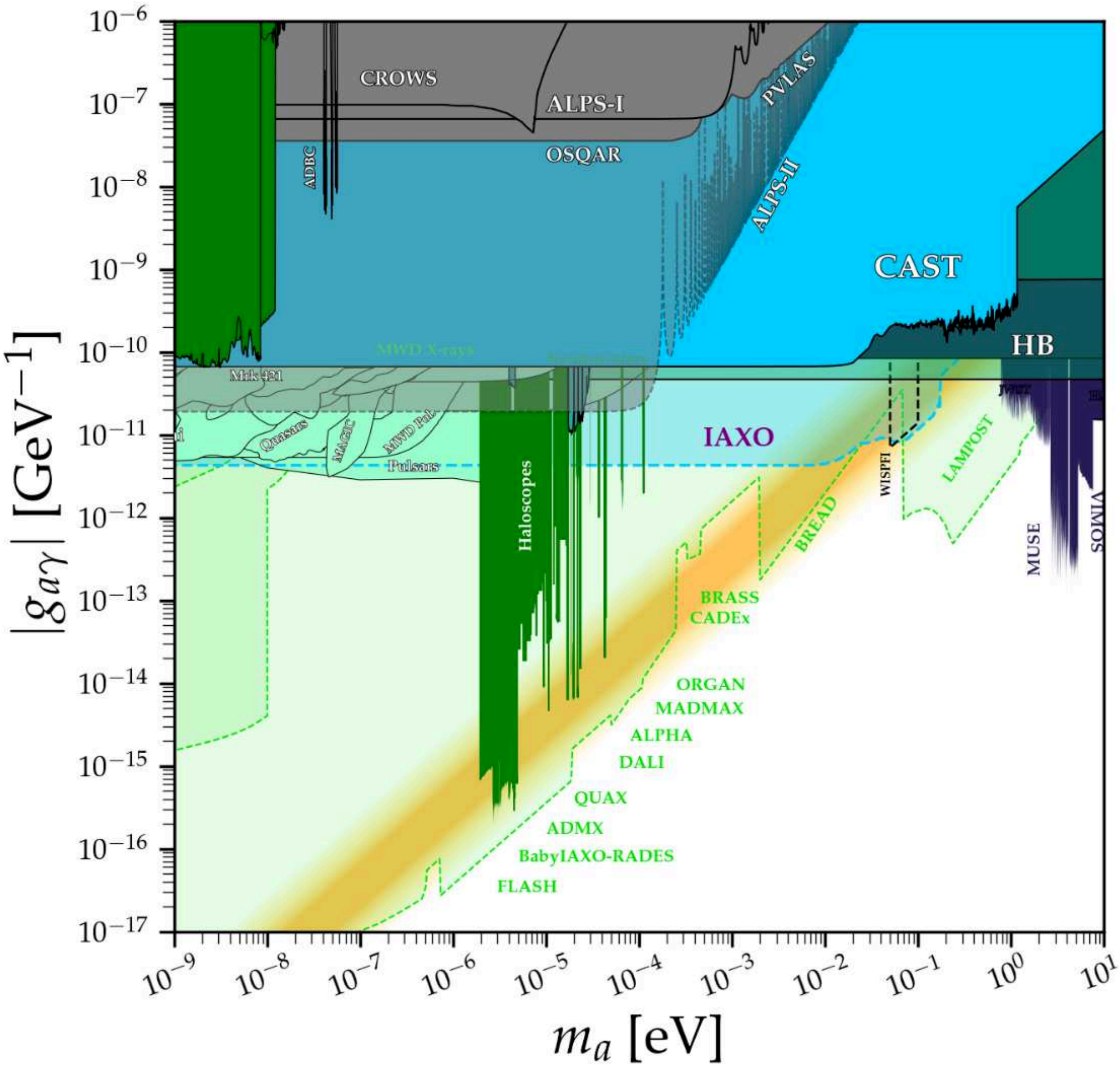

Figure 1.1: Current limits in the parameter space of $g_{a\gamma\gamma}$ vs. m_a. In gray, the model-independent limits set by LSW experiments are shown; in light blue, the limits set by helioscopes, mainly dominated by CERN Axion Solar Telescope (CAST) and in green, the limits imposed by haloscopes. The limits given in the light regions, delimited by the dashed lines, show the projection for future experiments for the three colors representing the three main categories of axion experiments. Image build using the repository in [26].

$$\mathcal{L} = -\frac{1}{4}F^{\mu\nu}F_{\mu\nu} + \frac{1}{2}(\partial_\mu\phi\partial^\mu\phi - m_\phi^2\phi^2) - \frac{1}{4}g_{a\gamma\gamma}\phi F^{\mu\nu}\tilde{F}_{\mu\nu} \tag{1.3}$$

where $F^{\mu\nu}$ and $\tilde{F}^{\mu\nu}$ describe the photon field, m_ϕ is the ALP mass and $g_{a\gamma\gamma}$ the coupling of the ALP to photons.

The one-dimensional case can be assumed in the conversion of a photon into an axion. In that case, a photon beam with angular frequency ω propagates in the x-axis in a medium with an index of refraction n, and a strong magnetic field transverses the photon beam and is much higher than the magnetic component of the photon beam. Moreover, it is considered that the photon beam propagates also as a plane wave with an electric field

$\vec{E}(\vec{x},t) = \vec{e}_z E_0 \exp\{i\omega(nx - t)\}$ and the magnetic field $\vec{B}(\vec{x}) = \vec{e}_z B f(\vec{x})$, where $f(x)$ is a function that describes the variation of the magnetic field along the x-axis. Then, the solution of the equation of motion derived from Eq. 1.3 is given by:

$$\phi(x,t) = \frac{i g_{a\gamma\gamma}}{2k_\phi} B\omega \exp\{-i(\omega t - 2k_\phi x)\} \int f(x') \exp\{-iqx'\}\, dx' \tag{1.4}$$

where $k_\phi = \sqrt{\omega^2 - m_\phi}$ and q is the momentum transferred to the magnetic field corresponding to:

$$q = n\omega - \sqrt{\omega^2 - m_\phi^2} \approx \omega(n-1) + \frac{m_\phi^2}{2\omega} \tag{1.5}$$

The process of conversion of a photon to ALP and ALP to a photon is symmetric. Therefore, the probabilities of these processes $P_{\gamma\to a}$ and $P_{a\to\gamma}$ are equivalent and can be computed from Eq. 1.4, which results in Eq. 1.6.

$$P_{\gamma\to a} = P_{a\to\gamma} = \frac{\omega}{4k_\phi}(g_{a\gamma\gamma}BL)^2 |F(qL)|^2 \tag{1.6}$$

F(qL) is a form factor that describes the magnetic field of length L and is defined by:

$$F(qL) \equiv \frac{1}{L}\int f(x') \exp\{-iqx'\}\, dx' \tag{1.7}$$

In the case of a homogeneous magnetic field, the form factor is:

$$|F_{\text{single}}(qL)| = \left| \frac{2}{qL} \sin\left(\frac{qL}{2}\right) \right| \tag{1.8}$$

Generalizing for a group of magnets with a gap Δ between magnets and considering that, in the magnet region, the magnetic field is homogeneous, the form factor becomes:

$$|F(qL)| = \left| \frac{2}{qL} \sin\left(\frac{qL}{2}\right) \frac{\sin\left(\frac{qN}{2}(\frac{L}{N} + \Delta)\right)}{\sin\left(\frac{q}{2}(\frac{L}{N} + \Delta)\right)} \right| \tag{1.9}$$

In the vacuum, $n = 1$, and a small momentum transfer $qL/2 \ll 1$ which corresponds to small masses $m_\phi \ll 8.9 \cdot 10^{-4}\text{eV}\sqrt{[\omega/\text{eV}][\text{m}/L]}$, the maximum of the conversion/reconversion probability $P_{a\to\gamma}$ occurs:

$$P_{\gamma\to a} = P_{a\to\gamma} = \frac{1}{4} g_{a\gamma\gamma}^2 B^2 L^2 \tag{1.10}$$

Finally, as mentioned before, in a LSW experiment, first the conversion of photons to ALPs happens and then the reconversion of the ALPs to photons. The probability of both processes for a single photon occurring is:

$$P_{\gamma\to a\to\gamma} = \frac{1}{16} g_{a\gamma\gamma}^4 B^4 L^4 \tag{1.11}$$

The probability depends on the fourth power of the coupling of ALP to photons, making it extremely challenging to explore low couplings. The use of optical cavities significantly enhances the probability and is the approach implemented in the ALPS II experiment, which will be described in the next section.

1.3 ALPS II experiment

Any Light Particle Search II is a LSW experiment located at the Deutsches Elektronen-Synchrotron (DESY) [28]. A scheme of this experiment is shown in Fig. 1.2.

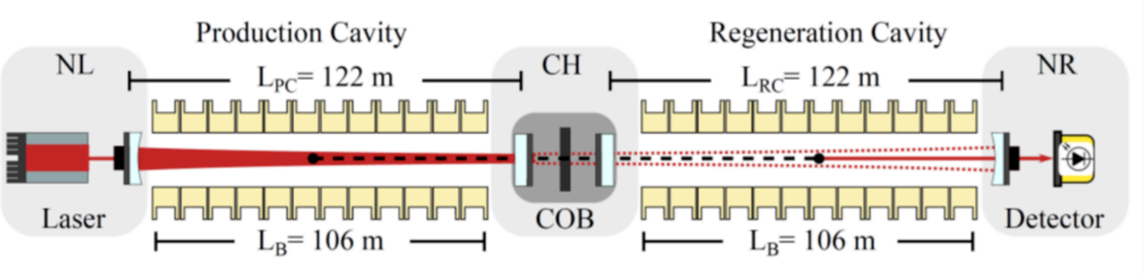

Figure 1.2: Scheme of the ALPS II experiment. From left to right, the main elements are shown together with the location inside the north section of the old HERA accelerator. North-left (NL): High-power laser used as a source of photons. Production cavity, between NL and CH: Zone where the photon beam is amplified and the photons are converted to ALPs interacting with the magnetic field generated by 12 dipole magnets. Central Hall (CH): The central optical bench (COB) location. Regeneration cavity, between CH and NR: Zone where the ALP field is amplified and the ALPs are converted back to photons interacting with the magnetic field generated by another set of 12 dipole magnets. North right (NR): Location of the detector to measure the regenerated photons (in the case of the heterodyne system). Image taken from [29].

The working principle is described in the following:

1. Photon production: A 1064 nm laser injects a photon rate corresponding to a power of approximately $P_L = 30$ W into the production cavity.
2. Conversion to axion/ALP: Inside a production cavity the photons could convert to ALPs by interacting with a strong magnetic field $B = 5.3$ T generated by the dipole magnets from the former Hadron-Elektron-Ring-Anlage (HERA) accelerator [30] with a total magnetic length of $L_B = 105.6$ m. The production cavity is an optical cavity that will enhance the ALP-photon conversion probability targeting a build-up factor $\beta_{PC} = 5 \cdot 10^3$ [31].
3. Wall: The axions/ALPs will travel from the production cavity to the regeneration cavity through a light-tight wall comprising a remotely operated shutter.
4. Reconversion to photon: Inside a regeneration cavity, ALPs could reconvert to photons by interacting with a magnetic field from another array of magnets identical to the ones in the previous step. The regeneration cavity is an optical cavity which will also enhance the ALP-photon reconversion probability targeting a build-up factor $\beta_{RC} = 4 \cdot 10^4$ [31].
5. Photon detection: The regenerated photons are guided towards the detection system and are measured.

In order to achieve the targeted build-up factors, the production and regeneration cavities need to be resonant with the frequency of the 1064 nm laser [32] with an offset in the frequency between the cavities resonant frequency of less than 1.5 Hz [33]. The choice of wavelength is given by a compromise between keeping the sensitivity to an axion/ALP mass as high as possible and the possibility of using high-quality mirrors which can withstand high power intensities [28]. Furthermore, ALPS II benefits from the existing expertise for 1064 nm optics from the gravitational wave interferometer community.

The improved scheme described before will enhance the sensitivity to the coupling constant by 10^3 compared to previous LSW experiments [34, 35]. ALPS II targets to be sensitive to $g_{a\gamma\gamma} = 2 \cdot 10^{-11}$ GeV^{-1}, which will allow to explore the region in the parameter space with the presence of hints from the astrophysical anomalies in stellar evolution [36], and the TeV transparency of photons [21], explained in section 1.1. Furthermore, the monopole-philic axion model proposed in [16] presents a QCD axion with a stronger coupling to photons than other axion models with the same mass. This axion overlaps with ALPS II in the region $g_{a\gamma\gamma} > 2 \cdot 10^{-11}$ GeV^{-1} of the parameter space meaning that ALPS II could be able to detect it.

ALPS II recently finished the first scalar and pseudo-scalar long data-taking periods in a configuration without the production cavity. This configuration was chosen to test the control and optical systems and assess the level of stray light [31]. Even with the reduced sensitivity due to the lack of a production cavity, it is expected to set unprecedented limits for a LSW experiment in the parameter space of ALP mass and $g_{a\gamma\gamma} > 6 \cdot 10^{-10}$ GeV^{-1} [37], improving by a factor of 30 with respect to its predecessor ALPS I.

Considering an ALP with coupling $g_{a\gamma\gamma} = 2 \cdot 10^{-11}$ GeV^{-1} motivated by the hints from the astrophysical anomalies aforementioned, the expected rate of reconverted photons can be calculated as:

$$n_{\gamma\to a\to\gamma} = 3.75 \cdot 10^{-19} \mathrm{s}^{-1} \frac{P_L}{1\mathrm{W}} \beta_{PC}\beta_{RC} \left(\frac{g_{a\gamma\gamma}}{10^{-10}\mathrm{GeV}^{-1}} \frac{B}{1\mathrm{T}} \frac{L_B}{10\mathrm{m}}\right)^4 \sim 10^{-5}\mathrm{s}^{-1} \tag{1.12}$$

The rate $n_{\gamma\to a\to\gamma}$ would then be in the order of one reconverted photon per day. Detecting this rate requires a very sensitive detector, which can also achieve low background levels. Two detection schemes have been proposed for this: heterodyne detection [38] and photon counting with a TES [39]. They will be described in the following.

1.3.1 Heterodyne detection scheme

Heterodyne detection is based on the interference of two signals, one with known power P_{LO} and a weak signal with power P_{sig} to be measured . The reference signal is commonly called a "local oscillator" (LO), and it is required to have a fixed offset in frequency f_0 and phase $\Delta\phi$ from the signal that is going to be measured. In this condition, both signals create a beat note of power P_d [40]:

$$P_d = P_{LO} + P_{sig} + 2\sqrt{P_{LO}P_{sig}} \cos(2\pi f_0 t + \Delta\phi) \tag{1.13}$$

The resulting beat note can be measured with a photodiode and demodulated to the frequency f_0. In the fundamental limit, the limiting factor in this measurement is the shot noise of the photodiode, which is produced due to the photon counting (Poisson) statistics. If the demodulation is performed for a time $\mathrm{T_{dem}}$, the apparent rate of photons is given by $\mathrm{n_{dem}}$:

$$\mathrm{n_{dem}} = \frac{\mathrm{P_{sig}}}{h\nu} + \frac{1}{\eta \mathrm{T_{dem}}} \tag{1.14}$$

where h is the Plack constant, ν is the photon frequency and η is the quantum efficiency of the photodiode [40]. Eq. 1.14 shows that for $\mathrm{T_{dem}}$ long enough, the second term corresponding to the shot noise can be integrated away, allowing the measurement of the signal's power $\mathrm{P_{sig}}$.

The heterodyne detection system has demonstrated good performance during the first ALPS II data takings with reduced sensitivity and is in good condition for the future ALPS II data taking at full sensitivity.

1.3.2 Single photon detection scheme

A tungsten Transition Edge Sensor (TES) system is under investigation as a photon-counting detector. This presents different systematics than the heterodyne system. It also requires a different optics setup [28] without a local oscillator and using 532 nm light for cavity control. It is foreseen as confirmation/cross-checking of the ALPS II results, using the heterodyne system, or as a backup in case the heterodyne system fails to meet the requirements. A TES is a cryogenic microcalorimeter operated in the transition region between superconducting and normal conducting states [41]. It is able to detect single photons with an efficiency higher than 95 % [42].

The current requirements for 5-sigma detection, during 20 days of data taking, of an axion/ALP with a coupling constant of $g_{a\gamma\gamma} = 2 \cdot 10^{-11}$ GeV^{-1} with this system are listed below [43]:

1. Sensibility to very low rates (1-2 photons a day).
2. Low energy photon detection (1064 nm equivalent to 1.16 eV).
3. Low background rate: $r < 7.7 \cdot 10^{-6}$cps $\sim$ 1 photon (1064 nm - like) every 2 days. A good energy resolution (better than 10 %) is required for background discrimination, including the 532 nm light for cavity control. An energy resolution better than 10 % allows a suppression of 532 nm by 10^{-10}. This requirement considers a 532 nm photon rate at 10^5 photons per second, just below the TES saturation.
4. High detection efficiency > 50 % (whole optical system).
5. The system should allow at least 20 days of continuous data-taking.

The TES is on a good track to meet the ALPS II requirements, already proven points 1, 2 and 5. However, further optimization is needed. This is part of the current efforts of the TES group at DESY. This thesis was developed within those efforts, mostly focused on the reduction of the background rate (point 3). The results will be shown in the next chapters.

CHAPTER

2

TRANSITION EDGE SENSOR SETUP

Contents

A Transition Edge Sensor (TES) is a type of superconducting detector operated in the transition region between superconducting and normal conducting states [41]. When working in this region, an energy deposition produces a rise in temperature, translating to a drastic change in the sensor's resistance, which produces a current pulse that can be measured. The TES studied in this thesis consists of a tungsten film provided by the National Institute of Standards and Technology (NIST) of dimensions 25 µm × 25 µm × 20 nm, with a critical temperature of around 140 mK. It is sensitive to energies in the order of 1 eV and optimized for efficient detection of 1064 nm photons. This chapter will briefly discuss the description of a TES, following the approach in [41]. Afterwards, the experimental setup used to measure the data analyzed in the next chapters will be discussed. A more realistic model of the TES under study in this thesis will be described in Chapter 3.

2.1 Physics of the TES

The most common method to model a TES combines an electrical and thermal circuit, as shown in Fig. 2.1a. The electrical circuit is composed of a current source I_{BIAS}, a shunt resistance R_{SH}, a coil with inductance L used for readout and the resistance $R(T, I)$ of the TES, at temperature T and current I flowing through it. Due to the coil, the circuit can also have a parasitic resistance R_{PAR} in the TES line. In the case of a voltage-biased TES, the shunt resistance satisfies $R_{SH} \ll R_N$ (current-biased: $R_{SH} \gg R_N$), where R_N is the resistance of the TES at the normal state. The voltage-biased circuit can also be represented by its Thevenin-equivalent, as shown in Fig. 2.1b, consisting of a bias voltage $V = I_{BIAS}R_{SH}$ and a load resistor $R_L = R_{SH} + R_{PAR}$, substituting I_{BIAS}, R_{SH} and R_{PAR} to simplify calculations.

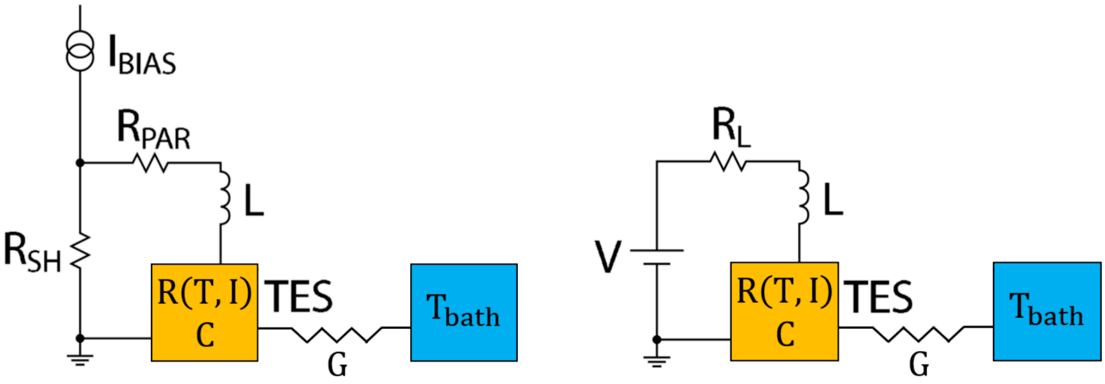

(a) (b)

Figure 2.1: (a) Model of the electrical and thermal circuits in the TES. The TES is kept hotter than the thermal bath due to the heat produced by the Joule power and the weak thermal link, with thermal conductance G defined in section 2.1.1, with the bath. (b) Same model as before, but the electrical circuit is replaced by its Thevenin equivalent.

According to Kirchhoff's law, the sum of the voltages in the electrical circuit depicted in Fig. 2.1b is zero. Then, Eq. 2.1 describes the electrical differential equation of the TES.

$$L\frac{dI}{dt} = V - IR_L - IR(T, I) \tag{2.1}$$

The temperature T of the TES is influenced by the power dissipated to the thermal bath P_{bath}, the Joule power $P_J = I^2R(T, I)$ produced at the TES and an external power P, associated to e.g. noise. The thermal differential equation is given by Eq. 2.2, where C is the heat capacity of the TES and any possible absorber connected to it.

$$C\frac{dT}{dt} = -P_{bath} + P_J + P \tag{2.2}$$

The power flowing from the TES to the thermal bath can be described by a power law dependence $P_{bath} = K\left(T^n - T^n_{bath}\right)$, where K is a proportionality factor and n depends on the nature of the thermal link to the heat bath, for instance, electron-phonon coupling.

The differential equations 2.1 and 2.2 present several nonlinear terms, which make them difficult to solve analytically. The terms can be linearized considering small signals, which will be developed in the following.

2.1.1 Small Signal Theory

In the small signal limit, small variations of the current $\delta I = I - I_0$ and the temperature $\delta T = T - T_0$ of the TES are defined from a steady state defined by temperature T_0, current I_0 and resistance R_0. That means that the resistance dependence of the TES can be linearized as in Eq. 2.3, where α and β are the temperature sensitivity and the current sensitivity defined in Eq. 2.4 and 2.5, respectively.

$$R(T,I) \approx R_0 + \left.\frac{\partial R}{\partial T}\right|_{I_0} \delta T + \left.\frac{\partial R}{\partial I}\right|_{T_0} \delta I = R_0 + \alpha\frac{R_0}{T_0}\delta T + \beta\frac{R_0}{I_0}\delta I \tag{2.3}$$

$$\alpha \equiv \left.\frac{\partial \log R}{\partial \log T}\right|_{I_0} = \frac{T_0}{R_0}\left.\frac{\partial R}{\partial T}\right|_{I_0} \tag{2.4}$$

$$\beta \equiv \left.\frac{\partial \log R}{\partial \log I}\right|_{T_0} = \frac{I_0}{R_0}\left.\frac{\partial R}{\partial I}\right|_{T_0} \tag{2.5}$$

The Joule power is expanded to the first order around T_0 and I_0 in Eq. 2.6, with a steady state Joule power dissipation given by $P_{J_0} = I_0^2 R_0$:

$$\begin{gathered} P_J = I^2 R(T,I) \approx I_0^2 R_0 + 2I_0R_0\delta I + I_0^2\left.\frac{\partial R}{\partial T}\right|_{I_0}\delta T + I_0^2\left.\frac{\partial R}{\partial I}\right|_{T_0}\delta I \\ P_J \approx P_{J_0} + I_0R_0(2+\beta)\delta I + \alpha\frac{P_{J_0}}{T_0}\delta T \end{gathered} \tag{2.6}$$

A similar procedure is done with the power transmitted to the thermal bath in Eq. 2.7, defining $G \equiv \partial P_{bath}/\partial T|_{T_0} = nKT_0^{n-1}$ as the thermal conductance seen in Fig. 2.1 and the power flow around the steady state $P_{bath_0} = K(T_0^n - T_{bath}^n)$:

$$P_{bath} = K(T^n - T_{bath}^n) \approx K(T_0^n - T_{bath}^n) + nKT_0^{n-1}\delta T \tag{2.7}$$

Furthermore, small variations of the power $\delta P = P - P_0$ and $\delta V = V - V_0$ are considered. As in the steady state of the TES, $V_0 = I_0R_L + I_0R_0$ and $P_{bath_0} = P_{J_0} + P_0$, the linearized form of Eq. 2.1 and 2.2 corresponds to Eq. 2.8 and 2.9 respectively.

$$\frac{d\delta I}{dt} = -\frac{R_L + R_0(1+\beta)}{L}\delta I - \frac{\mathscr{L}_I G}{I_0 L}\delta T + \frac{\delta V}{L} \tag{2.8}$$

$$\frac{d\delta T}{dt} = \frac{I_0R_0(2+\beta)}{C}\delta I - \frac{1-\mathscr{L}_I}{\tau}\delta T + \frac{\delta P}{C} \tag{2.9}$$

Where $\tau \equiv C/G$ is defined as the natural thermal time constant and $\mathscr{L}_I \equiv P_{J_0}\alpha/GT_0$ is the low-frequency feedback loop gain under constant current. If $I_0 = 0$, the thermal circuit is decoupled from the electrical circuit. If the temperature changes by ΔT, it will recover to the equilibrium following an exponential function with a decay time given by τ. On the other hand, for $I_0 \neq 0$, a temperature change produces a change in the current due to the change in the resistance of the TES, which then will affect the temperature as a consequence of a change in the Joule power. This process is known as Electrothermal feedback (ETF).

In voltage-biased conditions ($R(T,I) \gg R_L$), an increase in temperature reduces the Joule power, acting as a restoring force. Therefore, there is a negative ETF. High values of $\mathscr{L}_I$ ($\mathscr{L}_I \gg 1, \beta$) indicate a strong negative ETF, being advantageous for a TES by giving a faster response, stable operation and becoming self-calibrating. The latter advantage will be described at the end of this section. In current-biased conditions ($R(T, I) \ll R_L$), the ETF is positive, producing instabilities in the system.

Eq. 2.8 and 2.9 can be represented as a matrix (Eq. 2.10) and solved by diagonalization to decouple the system of equations as done in [44].

$$\frac{d}{dt}\begin{pmatrix}\delta I\\ \delta T\end{pmatrix} = -\begin{pmatrix}\frac{R_L+R_0(1+\beta)}{L} & \frac{\mathscr{L}_I G}{I_0 L}\\ -\frac{I_0 R_0(2+\beta)}{C} & \frac{1-\mathscr{L}_I}{\tau}\end{pmatrix}\begin{pmatrix}\delta I\\ \delta T\end{pmatrix} + \begin{pmatrix}\frac{\delta V}{L}\\ \frac{\delta P}{C}\end{pmatrix} \tag{2.10}$$

2.1.2 Response to a small energy deposition

A small energy deposition in the TES produces a small change in the temperature. If no other disturbances are considered, then Eq. 2.10 can be solved, neglecting $\delta P = 0$ and $\delta V = 0$, becoming the homogeneous form of the equation. That means that the solution is:

$$\begin{pmatrix}\delta I\\ \delta T\end{pmatrix} = A_+ \exp\{-\lambda_+ t\}\mathbf{v}_+ + A_- \exp\{-\lambda_- t\}\mathbf{v}_- \tag{2.11}$$

where $A_\pm$ are unitless constants, $\lambda_\pm$ the eigenvalues and $\mathbf{v}_\pm$ the eigenvectors of the homogeneous form of Eq. 2.10. Two time constants $\tau_\pm$ can be defined from the eigenvalues, which are given by Eq. 2.12:

$$\frac{1}{\tau_\pm} \equiv \lambda_\pm = \frac{1}{2\tau_{el}} + \frac{1}{2\tau_I} \pm \frac{1}{2}\sqrt{\left(\frac{1}{\tau_{el}} - \frac{1}{\tau_I}\right)^2 - 4\frac{R_0}{L}\frac{\mathscr{L}_I(2+\beta)}{\tau}} \tag{2.12}$$

τ_{el} is the bias circuit electrical time constant, which arises from the exponential decay of δI in the limit when $\mathscr{L}_I = 0$. τ_I is the current-biased thermal time constant and represents the exponential decay of δT when $\delta I = 0$. Both constants τ_{el} and τ_I are defined in Eq. 2.13.

$$\tau_{el} = \frac{L}{R_L + R_0(1+\beta)}, \quad \tau_I = \frac{\tau}{1-\mathscr{L}_I} \tag{2.13}$$

Considering the energy deposition E produces a temperature change given by $\Delta T = E/C$, the initial values of the temperature and current change from the steady state are $\delta T(0) = \Delta T$ and $\delta I(0) = 0$. Therefore, the solution of the homogeneous equation of Eq. 2.10 is the change in temperature in Eq. 2.14 and the change in current in Eq. 2.15.

$$\delta T(t) = \begin{cases}\left[\left(\frac{1}{\tau_I} - \frac{1}{\tau_-}\right)\exp\left\{-\frac{t}{\tau_+}\right\} - \left(\frac{1}{\tau_I} - \frac{1}{\tau_+}\right)\exp\left\{-\frac{t}{\tau_-}\right\}\right]\frac{\Delta T}{1/\tau_+ - 1/\tau_-}, & t \geq 0\\ 0, & \text{else}\end{cases} \tag{2.14}$$

$$\delta I(t) = \begin{cases}A\left(\exp\left\{-\frac{t}{\tau_+}\right\} - \exp\left\{-\frac{t}{\tau_-}\right\}\right), & t \geq 0\\ 0, & \text{else}\end{cases} \tag{2.15}$$

where A depends on the physics parameters as:

$$A = \left(\frac{\tau_I}{\tau_+} - 1\right)\left(\frac{\tau_I}{\tau_-} - 1\right)\frac{C\Delta T}{(2+\beta)\, I_0 R_0 \tau_I^2}\frac{1}{1/\tau_+ - 1/\tau_-} = \frac{\mathscr{L}_I}{I_0 L \tau}\frac{C\Delta T}{1/\tau_+ - 1/\tau_-} \tag{2.16}$$

The left part is the most used conventionally.

If L is sufficiently small, the condition $\tau_+ \ll \tau_-$ is fulfilled and Eq. 2.12 becomes equivalent to Eq. 2.17. The parameters τ_+ and τ_- then describe the rise and decay times of the pulse of current in Eq. 2.15.

$$\tau_+ \to \tau_{el}, \quad \tau_- \to \tau \frac{1+\beta+R_L/R_0}{1+\beta+R_L/R_0+(1-R_L/R_0)\mathscr{L}_I} \tag{2.17}$$

As aforementioned, in the strong negative ETF limit, $\mathscr{L}_I \gg 1, \beta$. Therefore, $\tau_- \ll \tau$ and the decay time of the current pulse becomes much shorter than the natural thermal decay time. The energy removed from the TES by ETF is given by Eq. 2.18 and converges to the deposited energy E by conservation of energy as the ETF becomes stronger.

$$E_{ETF} = -\int_0^\infty V_{TES}(t)\delta I(t)\, dt \approx -V\int_0^\infty \delta I(t)\, dt \tag{2.18}$$

E_{ETF} is only a function of the measured current in time and the voltage bias. Therefore, the initial deposited energy E measured with this magnitude is self-calibrating in the strong negative ETF.

2.1.3 Complex impedance

In Eq. 2.10, the voltage variations can be considered to find the corresponding response of the TES. Applying a Fourier transformation, the resulting matrix is given by Eq. 2.19, containing no derivative terms and depending on the angular frequency ω.

$$\begin{pmatrix} \frac{1}{\tau_{el}} + i\omega & \frac{\mathscr{L}_I G}{I_0 L} \\ -\frac{I_0 R_0 (2+\beta)}{C} & \frac{1}{\tau_I} \end{pmatrix} \begin{pmatrix} I_\omega \\ T_\omega \end{pmatrix} = \begin{pmatrix} \frac{V_\omega}{L} \\ 0 \end{pmatrix} \tag{2.19}$$

Solving for I_ω, the complex impedance Z_{omega} is computed as the ratio between the voltage V_ω and the current I_{omega}. The dependence of the complex impedance with the TES physical parameters is shown in Eq. 2.20.

$$Z_\omega = \frac{V_\omega}{I_\omega} = R_L + i\omega L + Z_{TES} = R_L + i\omega L + R_0\left(1+\beta+\frac{\mathscr{L}_I}{1-\mathscr{L}_I}\frac{2+\beta}{1+i\omega\tau_I}\right) \tag{2.20}$$

The measurement of the complex impedance consists of introducing a known input signal in the bias of the TES and recording the response of the TES to such signal. The resulting data can be fit to Eq. 2.20, allowing the extraction of the TES physical parameters as done in [45]. An example of such fit is shown in Fig. 2.2a.

The main difficulty in this measurement is that the response of the TES must be much higher than the noise level, but at the same time, the variations in the input signal with respect to the bias voltage should not be high enough to move the TES to another working point. Nevertheless, it could be performed in this thesis TES system using a network analyzer as done in [46].

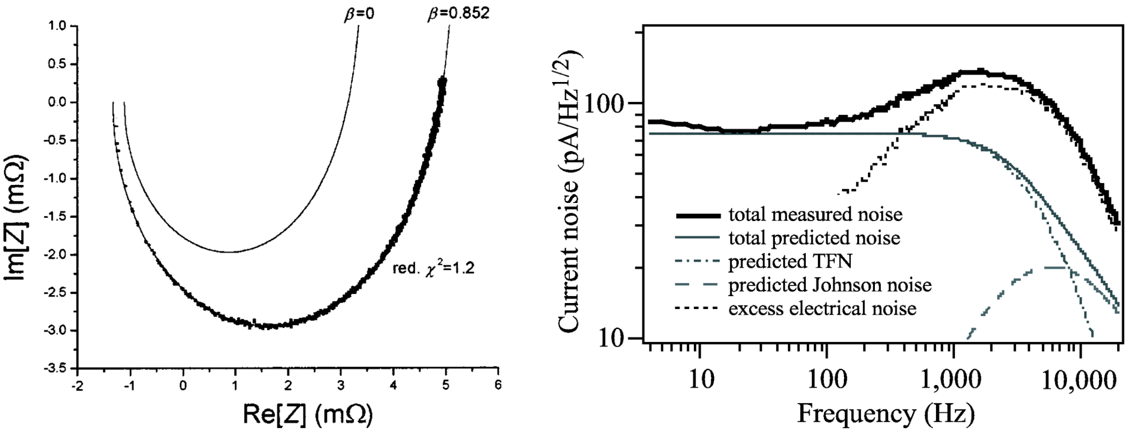

(a) (b)

Figure 2.2: (a) Complex impedance measured for a Mo/Au X-Ray TES and fit of Eq. 2.20 to data. Figure taken from [45]. (b) Measured noise in a TES with the noise components predicted by theory and appearance of excess noise. Plot taken from [41].

2.1.4 Thermal and electronic noise

Analogously to the complex impedance, the response of the TES to a sinusoidal power fluctuation $\delta P = \delta P_0 \exp\{i\omega t\}$ can be found using Eq. 2.10, and neglecting the voltage fluctuations it becomes Eq. 2.21.

$$\frac{d}{dt}\begin{pmatrix}\delta I\\ \delta T\end{pmatrix} = -\begin{pmatrix}\frac{R_L+R_0(1+\beta)}{L} & \frac{\mathscr{L}_I G}{I_0 L}\\ -\frac{I_0 R_0(2+\beta)}{C} & \frac{1-\mathscr{L}_I}{\tau}\end{pmatrix}\begin{pmatrix}\delta I\\ \delta T\end{pmatrix} + \begin{pmatrix}0\\ \frac{\delta P_0}{C}\end{pmatrix}\exp\{i\omega t\} \tag{2.21}$$

The solution is found in a manner similar to that of an energy deposition. The responsivity of the TES is defined as the current and temperature fluctuation due to a power fluctuation and can be calculated from the solution of Eq. 2.21. The power-to-current responsivity $s_I(\omega)$ and power-to-temperature responsivity show a dependency on the TES parameters given by Eq. 2.22 and Eq. 2.23, respectively.

$$s_I(\omega) = -\frac{1}{I_0 R_0}\frac{1}{2+\beta}\frac{(1-\tau_+/\tau_I)(1-\tau_-/\tau_I)}{(1+i\omega\tau_+)(1+i\omega\tau_-)} \tag{2.22}$$

$$s_T(\omega) = \frac{1}{G}\frac{\tau_+\tau_-}{\tau^2}\frac{(\tau/\tau_+ + \tau/\tau_- + \mathscr{L}_I - 1 + i\omega\tau)}{(1+i\omega\tau_+)(1+i\omega\tau_-)} \tag{2.23}$$

The predicted noise in a TES is a combination of the thermodynamic fluctuations associated with the electrical resistances (Johnson or Nyquist noise) and fluctuations the associated with the thermal impedance (thermal fluctuation noise (TFN)). It constitutes a fundamental limit on the noise equivalent power and, therefore, the energy resolution of the TES.

The power spectral density (PSD) of the Johnson-Nyquist noise is given by Eq. 2.24 as the sum of the noise in the TES and the load resistance.

$$S_J(\omega) = 4k_B I_0^2\frac{(1+\omega^2\tau_I^2)}{\mathscr{L}_I}(T_0 R_0 \xi(I) + T_L R_L(\mathscr{L}_I - 1)^2)|s_I(\omega)|^2 \tag{2.24}$$

The term $\xi(I)$ is a factor that describes the non-linear fluctuations of the TES. In the linear approximation, $\xi(I) = 1$ and, in the quadratic approximation, $\xi(I) = 1 + 2\beta$. The TFN's PSD is described by Eq. 2.25, where the term $F(T_0, T_{bath})$ is a correction due to nonlinear thermal conductance and can be approximated to 1/2.

$$S_{TFN}(\omega) = 4k_B T_0^2 G \cdot F(T_0, T_{bath}) |s_I(\omega)|^2 \tag{2.25}$$

According to [47], the energy resolution of a calorimeter in thermal equilibrium can be computed from the noise as:

$$\Delta E_{FWHM} = 2\sqrt{2\ln 2}\left(\int_0^\infty \frac{4 s_I(f)}{S_J(f) + S_{TFN}(f)}\, df\right)^{-1/2} \tag{2.26}$$

Therefore, the noise imposes a fundamental limit to the energy resolution of a TES, computed with Eq. 2.26, which reduces to Eq. 2.27 in a strong negative ETF.

$$\Delta E_{FWHM} = 2\sqrt{2\ln 2}\sqrt{4k_B T_0^2 \frac{C}{\alpha}\sqrt{\frac{n}{2}}} \tag{2.27}$$

The energy resolution worsens when the working temperature and the heat capacity of the TES increases and improves with a higher temperature sensitivity.

Overall, in TES systems, an excess noise contribution appears and is associated with electrical noise, given that it has the same frequency dependency as the Johnson-Nyquist noise. Fig. 2.2b shows an example of the expected noise contributions for a TES and the appearance of excess noise. The excess noise results in a worse energy resolution than predicted in Eq. 2.27.

The baseline noise will be simulated in chapter 5 to evaluate its contribution to the energy resolution of the TES under study in this thesis.

2.2 Main components of setup for TES characterization

The TES in this thesis is a tungsten film provided by NIST, of dimensions 25 μm × 25 μm × 20 nm. Its critical temperature is tuned to $T_c \approx 140$ mK, by mixing two crystal structures of tungsten during the fabrication process [48]. The TES is also optimized for the detection of 1064 nm photons with high quantum efficiency, i.e. the ratio between the number of photons absorbed in the TES and the photons arriving at the TES. Section 4.1.2 will discuss this in more detail.

A dilution refrigerator allows to achieve the necessary working temperatures for the TES, reaching approximately 25 mK at the coldest stage. A Superconducting Quantum Interference Device (SQUID) readout system reads the TES signal at very low noise levels. It produces a voltage signal that can be read with an oscilloscope, but a Data Acquisition (DAQ) system based on an Alazar card is used for long data-taking runs.

The dilution refrigeration, SQUID and DAQ systems will be discussed in sections 2.2.1, 2.2.2 and 2.2.3 respectively.

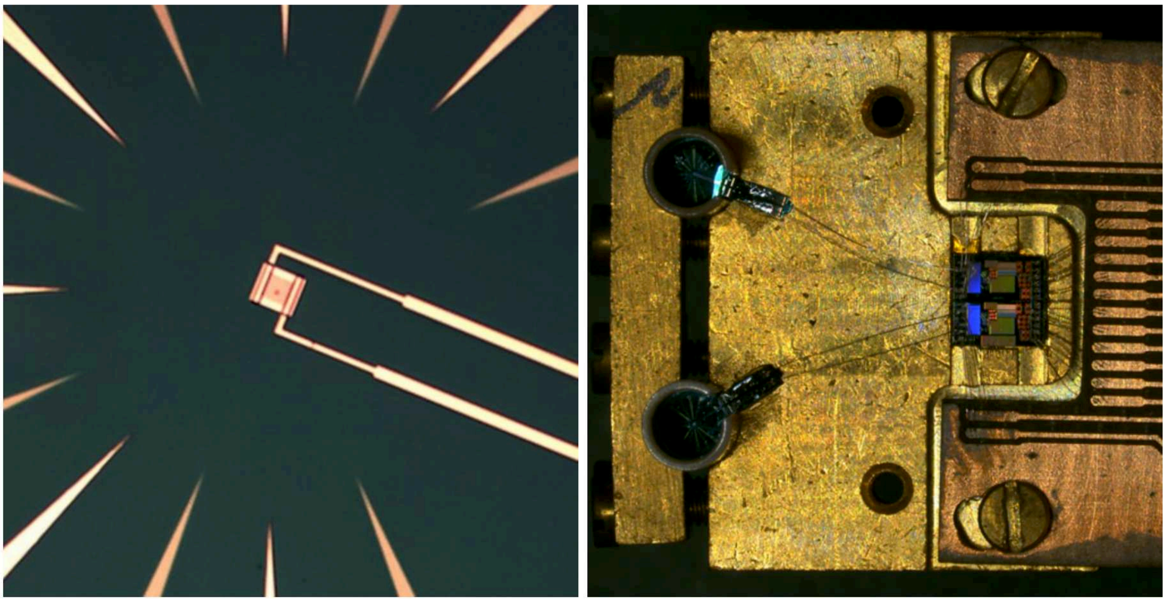

(a) (b)

Figure 2.3: (a) Picture of the TES (square in the center) deposited in a silicon substrate. The rails connected to the TES allow the biasing and reading of the TES signal. Image taken from [11]. (b) TES module assembled by Physikalisch-Technische Bundesanstalt (PTB) with two TES chips (rackets on the left) bonded to two SQUID chips (squares on the right).

2.2.1 Dilution refrigerator

A dilution refrigerator is a cooling system that provides continuous cooling to millikelvin temperatures. It exploits the properties of a mixture of the helium isotopes ^{3}He and ^{4}He in a closed system where the ^{3}He absorbs heat as it passes from a concentrated phase into a dilute phase with more ^{4}He. In the case of a dry dilution refrigerator, the heat absorbed during this phase transition is extracted through a cycle of evaporating and condensing the ^{3}He, facilitated by mechanical cryocoolers [49].

The cryostat used in this thesis is an SD dilution refrigerator system from BlueFors that can reach temperatures as low as 20 mK in the coldest stage without any experimental components. A scheme with the main components in the cryostat is shown in Fig. 2.4a. The system was described in detail in [11].

2.2.2 SQUID readout

The SQUID technology combines two quantum effects: flux quantization and Josephson tunnelling. The magnetic flux in a superconducting loop can only be integer numbers of a flux quantum $\Phi_0 = h/2e$; this is known as flux quantization. A Josephson junction consists of two superconductors coupled by a weak link, e.g. an insulator. When a current is applied in the junction the Cooper pairs tunnel through the barrier separating the two superconductors (Josephson tunneling). A voltage appears across if this current is higher than the junction's critical current. A shunt resistance is added to the junction to eliminate hysteresis in this effect.

In a dc SQUID such as the ones in the TES module, two shunted identical Josephson

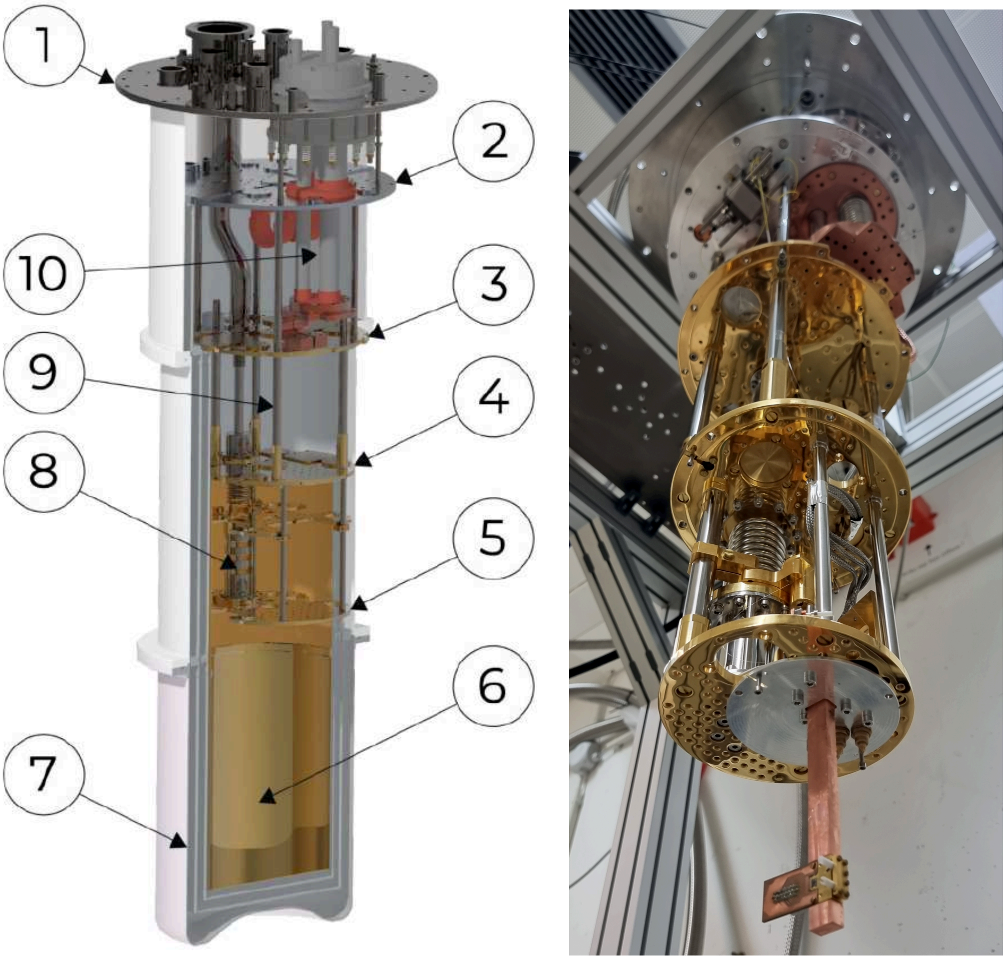

(a) (b)

Figure 2.4: (a) Scheme of the main cryostat elements: (1) Top flange at room temperature, (2) 40 K and (3) 4.2 K stages, both cooled by a pulse tube (10), (4) 1 K stage, (5) 25 mK stage, (6) space for experimental setup, (7) vacuum can and multiple radiation shields, (8) dilution unit, and (9) heat switches. Figure from Bluefors. (b) Picture of the open cryostat. The TES module is located in the bottom stage of the cryostat (25 mK) attached to a cold finger at (6).

junctions are connected in parallel in a superconducting loop [50]. With a bias current higher than the critical current for the two junctions ($I_b > 2I_c$), the voltage across the junctions oscillates with the magnetic flux in the loop with period Φ_0, as shown in Fig. 2.5a. The SQUID transfer function is defined as the maximum value of the variation of the voltage with respect to the flux and the bias current, $V_\Phi = \max(|\partial V/\partial\Phi|)$.

The SQUID is usually operated in a working point W where the $|\partial V/\partial\Phi|$ is highest as shown in Fig. 2.5a. The relation between V and Φ becomes non-linear very rapidly. To linearize the SQUID response, a flux-locked loop (FLL) is used as seen in Fig. 2.5b. The deviation of V from a voltage V_b is amplified, integrated and fed back via a resistor R_f through a coil with a mutual inductance M_f with the SQUID.

From Fig. 2.5b, it is seen that $\delta V_{out} = R_f \delta I_f$ and the flux at the SQUID is $\Phi = M_f \delta I_f$.

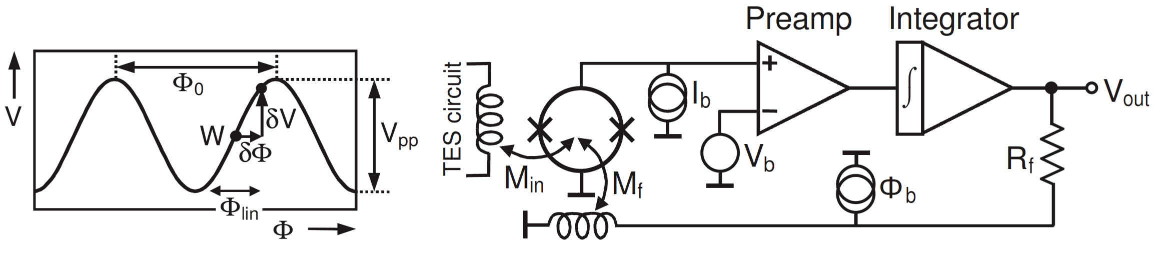

(a) (b)

Figure 2.5: (a) V-Φ characteristic of a dc SQUID. It shows a modulation with period Φ_0. The working point of the SQUID is usually chosen where the value of $|\partial V/\partial\Phi|$ is maximum. Figure from [11]. (b) Scheme representing a dc SQUID layout. The SQUID senses the magnetic flux from the TES circuit. The signal produced by the SQUID is amplified and integrated. The output from the amplifiers can be read, and also is fed back to the SQUID in the flux-locked loop (FLL) mode. Taken from [51].

The TES circuit can be coupled to the SQUID via a mutual inductance M_{in}, then the flux at the SQUID is $\Phi = M_{in}\delta I_{TES}$. Therefore, the flux at the SQUID can be written as $\Phi = M_f\delta I_f = M_{in}\delta I_{TES}$, which means that the output voltage V_{out} from the SQUID is related to the current circulating through the TES via Eq. 2.28 and only depends on constant circuit parameters.

$$\delta I_{TES} = \delta V_{out}\frac{M_{in}^{-1}}{R_f M_f^{-1}} \tag{2.28}$$

On the other hand, the bandwidth of the SQUID readout is limited by the amplifier and integrator in Fig. 2.5b. If G_S represents the gain between the integrator output and the voltage before the amplifier, then the gain of the amplifier and the integrator is given by $G_a = 1/G_S$ and can be computed with $1/G_a = G_S = V_\Phi/R_f M_f^{-1}$. The bandwidth of a system f_{3dB} is commonly defined as the frequency where the power of the signal is halved. The bandwidth of the SQUID readout is given by Eq. 2.29, where the Gain Bandwidth Product (GBWP) of the amplifier and the integrator can usually be adjusted.

$$f_{3dB} \approx G_S \mathrm{GBWP} \tag{2.29}$$

The response of the SQUID readout in the frequency domain will be given by the closed-loop gain $|G_{FLL}(f)|$ with a delay time t_d that takes into account dynamic errors and phase shifts in the circuit components [52]. It can be modelled with Eq. 2.30.

$$|G_{FLL}(f)| = \frac{1}{\sqrt{1 + \frac{f}{f_1}\left(\frac{f}{f_1} - 2\sin(2\pi f t_d)\right)}} \tag{2.30}$$

At low values of $f_1 t_d \ll 0.08$ [52], the FLL can be approximated to a first-order low-pass response with $f_{3dB} = f_1$.

In this thesis, a two-stage SQUID system is used, i.e. a first SQUID reads the signal from the TES, and the second amplifies the signal from the first one. The SQUIDs were provided by Physikalisch-Technische Bundesanstalt (PTB). Furthermore, PTB assembled them in a module together with the TES as shown in Fig. 2.3b.

2.2.3 Alazar DAQ

An oscilloscope can measure and visualize the SQUIDs output as a voltage signal. However, for ALPS II, a data-taking time of several days is envisioned. These long data-taking runs require a more advanced DAQ system. A model ATS9626 Alazar card is currently implemented. It is able to take data at a sampling rate of up to 250 MS/s from two voltage inputs in a range between -1.25 V and 1.25 V. The voltage is converted into a 16-bit integer, equivalent to a precision of $3.8 \cdot 10^{-5}$V.

The software to execute the data acquisition is named AlazarGui and was initially implemented in [53]. The acquisition is usually done in continuous or pseudo-triggered mode for a given time t. The data is collected continuously in the continuous mode until t is reached. At a high sampling rate, the amount of data grows very rapidly with the acquisition time. Therefore, this mode is not used to collect more than a few seconds. For long acquisition times, the pseudo-triggered mode is preferred. The data is acquired in sections and saved in the computer's memory, and then the software checks where the data is lower than a negative trigger threshold. At those points, a number of samples before (preSamples) and after (postSamples) the trigger point are collected. When a section is fully checked, it is discarded, and new memory is made available to store the next data section. At the end of the acquisition, the result is the collection of M trigger windows with a number of samples N = preSamples + postSamples.

The data collected in both acquisition modes is saved inside a TTree in a ROOT file [54], together with metadata such as the acquisition time and the timestamp of every trigger window.

Several upgrades were implemented in the AlazarGui within this thesis and are currently under testing. They are covered in appendix D.

2.3 Experimental setups

When the cryostat reaches stable operating conditions, with its coldest stage at 25 mK, both the SQUIDs and the TESs can be activated and utilized. As aforementioned, the SQUIDs are locked in the FLL mode, where they are most linear. The procedure to lock the SQUIDs was described in detail for this system in previous theses [11, 51]. The TES working point (WP) is defined as the ratio between the resistance of the TES R_0 at the steady state and the TES resistance R_N when it is in the normal conducting state. The TES WP can be set by applying a bias current I_{BIAS}, as defined in Fig. 2.1a. The TES WP is selected as the one with the best energy resolution and signal-to-noise ratio.

I-V curves

To find the correspondence between the bias current I_{BIAS} and the TES WP, a scan over the values of I_{BIAS} is done using a function generator. The measured dependence of the WP with I_{BIAS} is shown in Fig. 2.6a as an example.

Response to 1064 nm photons

The TES is characterized according to its response to 1064 nm photons, the same wavelength used in ALPS II. A 1064 nm laser is implemented as a photon source, and its light is

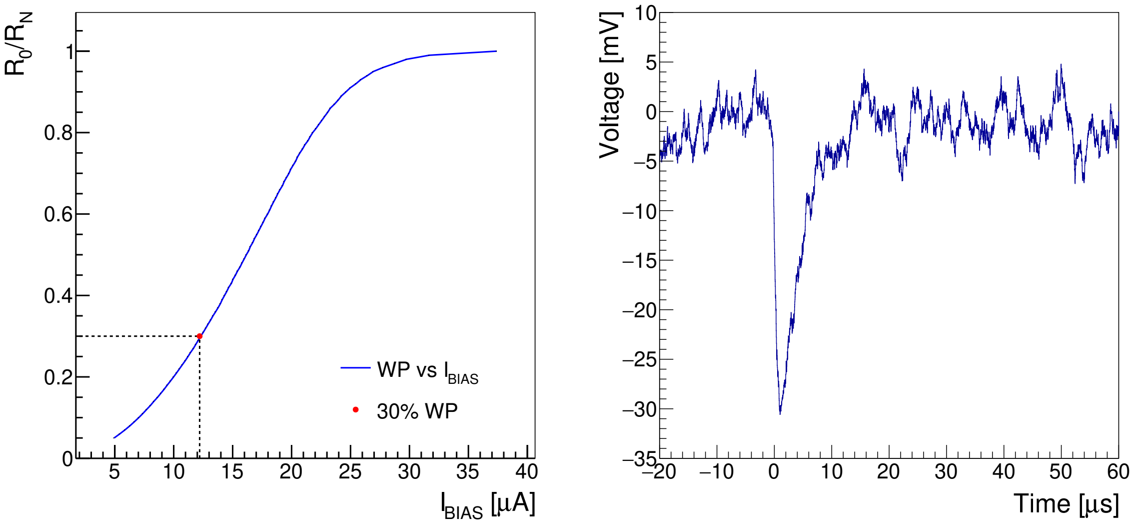

(a) (b)

Figure 2.6: (a) Measured dependence of the TES WP with the bias current. A WP at 30 % of the normal resistance is usually chosen as it optimizes the signal-to-noise ratio. (b) Single 1064 nm photon measured at a 30 % WP, SQUID GBWP of 1.5 GHz and a sampling rate of 50 MHz with the AlazarGui.

sent to the TES through an optical fiber. A high flux of photons saturates the TES. Therefore, several stages of attenuation are located in the path between the laser and the TES. Usually, a rate of 1000 photons per second arriving at the TES is chosen to prevent a large contribution of pile-ups while minimizing the acquisition time. For the characterization a sample of size between 1000 and 10000 pulses is enough for good statistics. This means that in a few seconds, enough photon pulses are collected. Therefore, the DAQ system can operate in continuous or pseudo-triggered modes. If the second is chosen, the trigger threshold is set low enough to avoid triggering noise and high enough to ensure high efficiency for 1064 nm photon pulses. A measured 1064 nm photon is shown in Fig. 2.6b.

This measurement will be key in the following chapters of this thesis. In chapter 3, the measurement data will be used to calibrate and compare simulation results. In chapter 4, as a guide for background rejection and assessment of the expected background in ALPS II. Finally, in chapter 5 and 6, the energy resolution of the TES is computed and a signal simulation is implemented from this data.

Linearity measurement

The linearity of the TES is defined as how linear is its response to photons at different wavelengths. The setup is similar to the one previously described for 1064 nm photons. In this case, a 642 nm laser and a white light source with a 750 nm filter were used as a source of photons, while a spectrometer was used to be sure that the proper wavelength was sent to the TES. The results of this measurement will be discussed in chapter 6.

Intrinsic background measurement

The intrinsic background (intrinsics) measurement is performed by disconnecting the optical fiber from the TES. In this way, the TES is completely in the dark, protected from the exterior environment by the shields of the cryostat. To assess the background rates over long periods of time, the pseudo-triggered mode of the DAQ must be used. If the trigger threshold is chosen as the same used for 1064 nm photon samples, a trigger rate in the order of 10^{-2} cps is usually measured. The analysis and simulation of the recorded events in this background measurement will be performed in chapter 3. The origin of these background events will also be discussed.

Extrinsic background measurement

The extrinsic background (extrinsics) measurement is performed by connecting one end of the optical fiber to the TES while leaving the other end outside of the cryostat covered with a fiber cap and in the dark. The data acquisition conditions are the same as for the intrinsics measurement, but the rate increases as a consequence of additional sources of background, such as thermal radiation and light from the laboratory room leaking into the fiber. The computation of the predicted rates for the additional background and the analysis of the recorded events in the extrinsics measurement will be discussed in chapter 4.

Efficiency measurement

The setup to measure the efficiency of our system is based on a setup from PTB [55]. It consists of the splitting of the light from a 1064 nm laser towards a calibrated photodiode (used as a reference) and towards a stage of attenuation, which is connected to the TES. The photon rate at the TES is measured, and the results are converted to power and compared with the reference. The attenuation stage is also characterized to compare the photon rate at the TES and the power in the photodiode. The preliminary results of this measurement were published in [56].

CHAPTER

3

SIMULATION OF INTRINSIC BACKGROUND

Contents

The observation of background events on the order of 10^{-2} cps in the intrinsic measurement setup is associated with radioactivity and cosmic muons interacting with the TES [11, 51]. A simulation of these background events requires the ability to model the transport of radiation and the physics of the TES. This chapter proposes a simulation consisting of the combination of the software COMSOL Multiphysics [57] and Geant4 [58] for this purpose. The first results of this simulation are compared to measured background data.

3.1 Populations of intrinsic background events

As explained in section 2.3, during the intrinsic background measurement, the TES should be isolated from external influences by the aluminum can and the shields of the cryostat. However, a background rate in the order of 10^{-2} cps is measured if the trigger threshold in the DAQ system is set at about 75 % of the pulse height of 1064 nm pulses. In a previous thesis, it has been demonstrated that the dark count rate can be reduced to meet the ALPS II requirements by means of a cut-based analysis while still maintaining high light acceptance of more than 90 % of 1064 nm pulses [11]. Alternatively, machine learning methods can be employed to obtain comparable results as done previously in the TES group [59].

The cut-based analysis and part of the machine learning techniques discriminated 1064 nm pulses from the background based on the parameters of a phenomenological fitting function described by Eq. 3.1, which will be described in more detail in section 5.1.

$$U_{\mathrm{ph}}(t) = -\frac{2A}{\exp\left\{-\frac{1}{\tau_{\mathrm{rise}}}(t-t_0)\right\} + \exp\left\{\frac{1}{\tau_{\mathrm{decay}}}(t-t_0)\right\}} + V_0 \tag{3.1}$$

In Eq. 3.1, the parameters A, τ_{rise} and τ_{decay} are related to the amplitude, the rise and the decay time of the pulse, respectively. The parameters t_0 and V_0 correspond to the pulse position in a time window and the voltage offset.

The ability to discriminate between pulses mainly relies on the difference between the shape of 1064 nm photon pulses and the background pulses. This is manifested, for instance, in the example pulses in Fig. 3.1a, and the distributions of pulse height and decay time in Fig. 3.1b, where the region corresponding to 1064 nm photons (red circle) occupies a very small section of the parameter space.

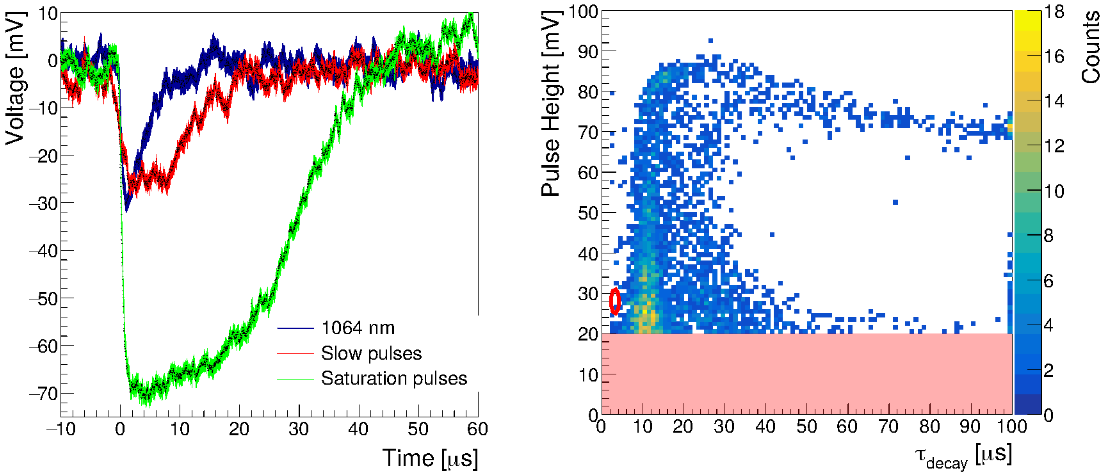

(a)

(b)

Figure 3.1: (a) Example pulses: 1064 nm, slow intrinsics, saturation intrinsics, (b) Pulse height vs. decay time of 1064 nm pulses (red circle) compared to intrinsics. The red-shaded area is below the trigger threshold at 20 mV.

The appearance of background events differing from 1064 nm pulses has been observed in other sensors with the same module design when performing intrinsics measurements. In [60], a separation of background events in populations was performed according to their shape. In that work, the muons and radioactivity were pointed out as possible background sources by depositing energy in the silicon substrate where the sensor is situated. Moreover, [61] performed an intrinsics measurement with gamma-ray sources outside the cryostat but near the sensor, which resulted in the appearance of new background events, indicating the sensitivity of the sensor to radioactivity.

3.2 Modeling a TES

Based on the aforementioned publications [60,61], it is assumed that the background events are produced mainly by particles depositing energy in the silicon substrate where the sensor is located, which then produces a response in the TES. The simulation of these events requires not only the modeling of the TES but also the silicon substrate where the TES is placed. Therefore, the TES model described in section 2.1 becomes more complex as shown in Fig. 3.2a.

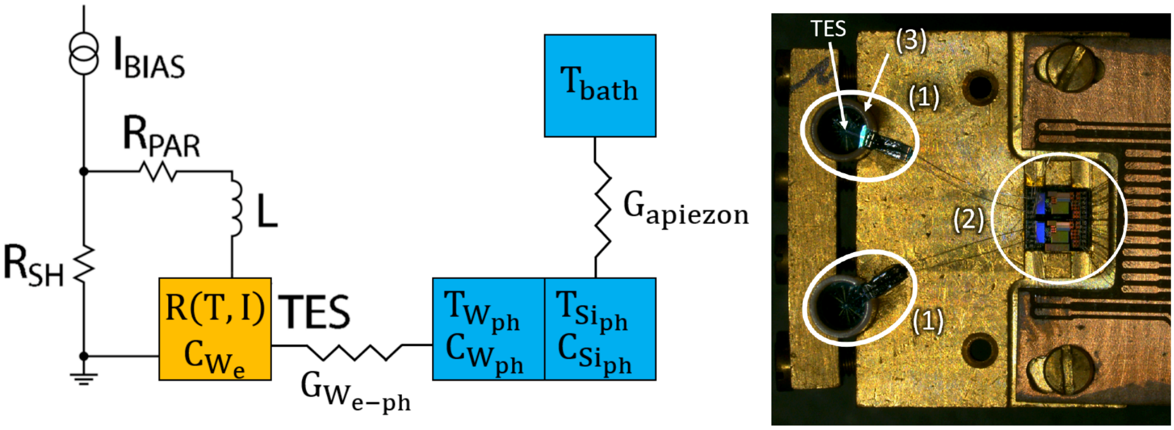

(a) (b)

Figure 3.2: (a) Model of the electrical and thermal circuits in the TES. The approximate values of the variables are given at the end of section 3.3. (b) Close-up of the TES module. The TES is in the center of the racket-shaped silicon substrate (1), which is also centered within the zirconia sleeve (3) to guarantee a high coupling efficiency with the optical fiber. The silicon substrate is supported by a sapphire rod below it, not visible in the picture. The TES chips are wire-bonded to the SQUID chip on the right (2).

In order to simulate the more complex TES model, the software COMSOL Multiphysics [57] is used. This software is based on the finite element method. The components considered in the model are the tungsten volume, which is the TES itself, the silicon substrate, where the sensor is deposited during fabrication, which can be seen in Fig. 3.2b, and the thermal contact between the silicon substrate and a sapphire rod. The latter thermally couples with the rest of the TES module and the cryostat. The geometry of the TES simulation in COMSOL can be seen in Fig. 3.3.

Tungsten system

The tungsten volume requires simulating the heat transport inside the volume and the electrical circuit. The electron and phonon systems in the tungsten are separated into two

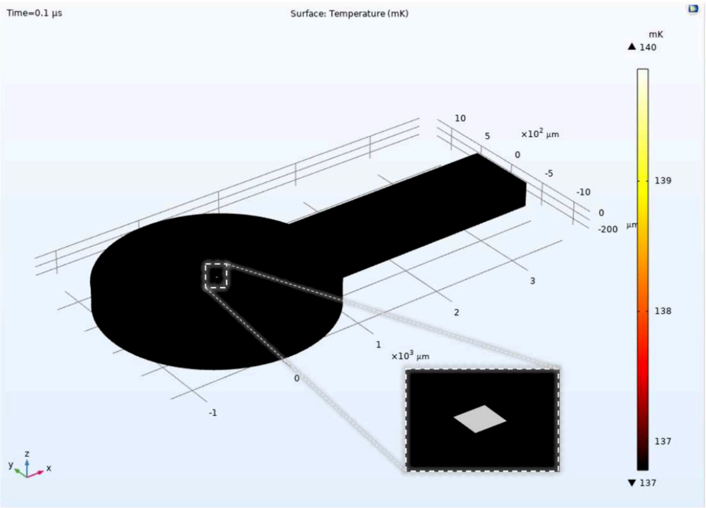

Figure 3.3: Simulated geometry in COMSOL corresponding to the silicon substrate (black) and the µm × µm-sized TES (white dot in the middle of the circle). The diameter of the circular area in the silicon substrate is $d_{Si} = 2.5$ mm, and the length of the leg is $x_{Si} = 2.5$ mm with a width of $y_{Si} = 0.8$ mm. The height of the substrate corresponds to $z_{Si} = 275$ µm. The colors indicate the temperature difference between the TES and the silicon substrate.

volumes to consider their interactions as independent systems. The simulation components are described below:

- Electrical circuit: Depicted in Fig. 3.2a. The approximate values of the inductance of the circuit $L = 20$ nH, the shunt resistance $R_{SH} = 24$ mΩ and the parasitic resistance $R_{PAR} = 36$ mΩ are provided by PTB. The modeling of the TES resistance $R(T, I)$ and the bias current I_{BIAS} will be described later.

- Heat transport in the tungsten electron system: The temperature of the system is defined as T_e, with a heat capacity per unit of mass calculated as $C_{W_e} = 2.43\gamma_W T_e / V_m \rho_W$, where $\gamma_W = 1.3 \cdot 10^{-3}$ J/(mol $\cdot$ K^2) is the molar specific heat of tungsten, $V_m = 9.6 \cdot 10^{-6}$ m^3/mol is the molar volume of tungsten, and $\rho_W = 1.78 \cdot 10^4$kg/m^3 is the density of tungsten. The factor 2.43 appears in the transition of tungsten between superconducting and normal conducting state [62]. This factor gives an upper limit of the heat capacity since, in reality, it can vary from 2.43 to 1 in the transition [45].

- Heat transport in the tungsten phonon system: The temperature of this system is defined as T_{ph}, with a heat capacity per unit of mass computed using the Debye model for low temperatures $C_{W_{ph}} = 234\, R_g (T_{ph}/\theta_W)^3/\mu_W$ [63], where R_g is the molar gas constant, μ_W is the molar mass of tungsten and $\theta_W = 383$ K is the Debye temperature of tungsten reported in [64].

The interaction between the tungsten electron and phonon system is a form of Eq. 2.7 for tungsten, considered as $P_{e-ph} = \Sigma_W \left(T_e^n - T_{ph}^n\right)$ for the power per unit of volume transmitted from the electron system to the phonon system when $T_e > T_{ph}$, with $\Sigma_W = 0.4\,\mathrm{nW}/(\mu\mathrm{m}^3 \cdot \mathrm{K}^5)$ electron-phonon coupling and $n = 5$ thermal link constant for a superconductor [65]. The condition $T_e = T_{ph}$ if T_{ph} becomes larger than T_e is imposed to represent the sensitivity of the electrons to the distortion of crystal structure produced by the phonons [63]. The condition would also be consistent with the breaking of Cooper pairs by hot phonons (temperatures over T_c) [62]. This condition is an approximation; in reality, this effect could be reflected in an increase in Σ_W of the electron-phonon coupling as T_{ph} approaches T_e.

The TES resistance is represented by Eq. 3.2, which is inspired by the form used in [65], but using an error function instead of a hyperbolic tangent.

$$R(T, I) = \frac{R_N}{2}\left[1 + \text{erf}\left\{\frac{T_e - T_c + \Delta_I I}{\sqrt{2}\sigma_T}\right\}\right] \tag{3.2}$$

Eq. 3.2 depends on the temperature of the electron system T_e and the current passing through the sensor given by solving the circuit at that resistance. The parameters T_c, σ_T, and Δ_I describe the tungsten critical temperature, the transition's width at a fixed current, and the shift in the transition at a fixed temperature.

Silicon substrate

The silicon substrate has a racket shape, as seen in Fig. 3.2b, with a diameter of d_{Si} = 2.5 mm, thickness z_{Si} = 275 μm, a width of the legs y_{Si} = 0.8 mm and a length in the legs of x_{Si} = 2.5 mm. It is composed of p-doped silicon with a resistivity between 10 and 20 $\Omega \cdot$ cm [66], which corresponds to a carrier concentration in the order of 10^{15} cm^{-3} [67], meaning this is lowly doped silicon. Given the low carrier concentration, the electron system in the silicon is neglected in the simulation.

No thermal resistance is assumed between the tungsten and the silicon phonon systems. The temperature of the silicon phonon system is defined as T_{ph}, and the system has a heat capacity per unit of mass calculated with the Debye model $C_{Si_{ph}} = 234\ R_g(T_{ph}/\theta_{Si})^3/\mu_{Si}$ with μ_{Si} as the molar mass of silicon and $\theta_{Si} = 645$ K its Debye temperature [64]. The heat conductivity k is calculated using the expression $k = \frac{1}{3}C_{Si_{ph}} \cdot v \cdot l \cdot \rho_{Si}$, where $C_{Si_{ph}}$ is the heat capacity of the phonon system, v and l are the average velocity and the mean free path between collisions of the phonons respectively [63]. The average velocity of phonons in silicon can be considered as $v = 6.4 \cdot 10^3$ m/s [68]. The mean free path of the phonons is given by the scattering of the phonons in the silicon crystal lattice. The boundary scattering is the dominant effect in pure silicon at a temperature below 10 K. The mean free path in this condition is given by the smallest dimension of the silicon substrate, $l_{pure} = 275$ μm [68, 69]. As the silicon in the substrate is p-doped, the mean free path of the phonons is reduced due to the presence of impurities [70, 71]. A free parameter k_{corr} is introduced to account for this reduction, where $k_{corr} = 1$ in the presence of pure silicon and $k_{corr} < 1$ for silicon with impurities. Taking this into account, the heat conductivity of the silicon substrate is computed as $k = \frac{1}{3}k_{corr} \cdot C_{Si_{ph}} \cdot v \cdot l_{pure} \cdot \rho_{Si}$.

In Fig. 3.2b, the silicon substrate is thermally connected to a sapphire rod with apiezon grease [66]. The sapphire rod and the rest of the components of the TES module and the cryostat are assumed to be at a constant temperature T_{bath}, equivalent to a thermal bath. The thermal contact between the silicon substrate and the sapphire rod is assumed to produce a heat transfer described by $q_{contact} = H_c(T - T_{bath})$, with $H_c = 184\text{W}/(\text{m}^2\text{K})$ [72]. Despite this being a rough estimation, variations even by one order of magnitude do not change the simulation results.

WP (%)	R_0	I_{BIAS}(μA)	I_0(nA)	I_{SST}(mVμs)	τ_-(μs)	η
20	0.2 R_N	9.99	113.0	169 ± 3	3.44 ± 0.05	0.294 ± 0.005
30	0.3 R_N	12.2	92.8	137 ± 2	3.34 ± 0.05	0.291 ± 0.005
40	0.4 R_N	14.3	80.9	117 ± 2	3.31 ± 0.05	0.290 ± 0.005
50	0.5 R_N	16.2	73.0	103 ± 2	3.34 ± 0.05	0.288 ± 0.005
60	0.6 R_N	18.0	67.4	92 ± 1	3.42 ± 0.05	0.286 ± 0.005

Table 3.1: Variation of the TES parameters with the WP. There is no reason to expect a variation in the process of photon absorption in the TES with the WP. This is reflected in the behavior of the parameter η, which stays constant within uncertainties with the WP.

3.3 Calibration of the TES model

The complex impedance measurement is the most optimal way to obtain the physical parameters of the TES [45]. During the development of this thesis, this measurement was not possible due to the malfunctioning of the cryostat and the TES sensors. The missing parameters to calibrate the simulated TES are I_{BIAS}, σ_T, Δ_I, k_{corr} and T_{bath}, which were described before. The parameters, except k_{corr}, which remains as a free parameter in the simulation, were obtained from the results of the fitting procedure described in chapter 6 and measured I-V curves. The procedure is described below.

IV curves

As described in section 2.3, the relation between the bias current I_{BIAS} and the TES WP, i.e. the resistance of the TES at a working point R_0, can be measured which provides the I-V curve. The data to calibrate the simulated TES with the fitting procedure corresponds to a set of WPs with resistances R_0, with bias current I_{BIAS}, which translates to a current circulating through the TES of I_0. The values for every WP are summarized in Table 3.1. The critical temperature of the TES is assumed as $T_c = 140$ mK due to its tuning conditions [48] and taking previous setups as reference [11,51]. By assuming that this temperature is reached at $0.5R_N$ WP, the bath temperature can be calculated from Eq. 2.7 as

$$T_{bath} = \left(T_c^5 - \frac{I_0^2 R_0}{\Sigma_W V_W} \right)^{1/5} \tag{3.3}$$

where $V_W = 1.25 \cdot 10^{-17}$ m^3 is the tungsten volume. This gives a bath temperature of $T_{bath} = 136.7$ mK. The error introduced by considering T_{bath} instead of T_{ph} in Eq. 3.3 is less than 0.1 % according to the simulation with COMSOL, meaning that the phonon temperature in the tungsten is almost the same as that in the bath.

Parameters from fitting procedure

The fitting procedure, which will be described in section 6.1, allows to find the TES physical magnitudes τ_- and E_{ETF} defined by Eq. 2.17 and 2.18. The magnitude τ_- is obtained directly from the fitting procedure, while $E_{ETF} = I_0 R_0 \cdot I_{SST} \cdot a_{VtoI}$ is calculated from the integral of the TES pulse (I_{SST}) defined by Eq. 6.4, and also depends on the working point conditions (I_0, R_0) and the conversion from the voltage in the DAQ card to the current in the TES defined as a_{VtoI}. If the output voltage of the SQUIDs is equal to the input in the DAQ card, then $a_{VtoI} = M_{in}^{-1}/R_f M_f^{-1}$ from Eq. 2.28. A difference between voltages could arise due to couplings between the input and output impedances. For this system, $M_{in}^{-1} = 5.65\mu A/\Phi_0$ and $M_f^{-1} = 42.75\mu A/\Phi_0$, as given by PTB, and the feedback resistance was set at $R_f = 100$ kΩ. Therefore, the conversion from the voltage in the DAQ card to the current in the TES is $a_{VtoI} = 1.32$nA/mV. The distributions of the pulse integral I_{SST} and the decay time τ_-, for 1064 nm photon measurements with the TES WPs defined before, are shown in Fig. 3.4a and 3.4b respectively.

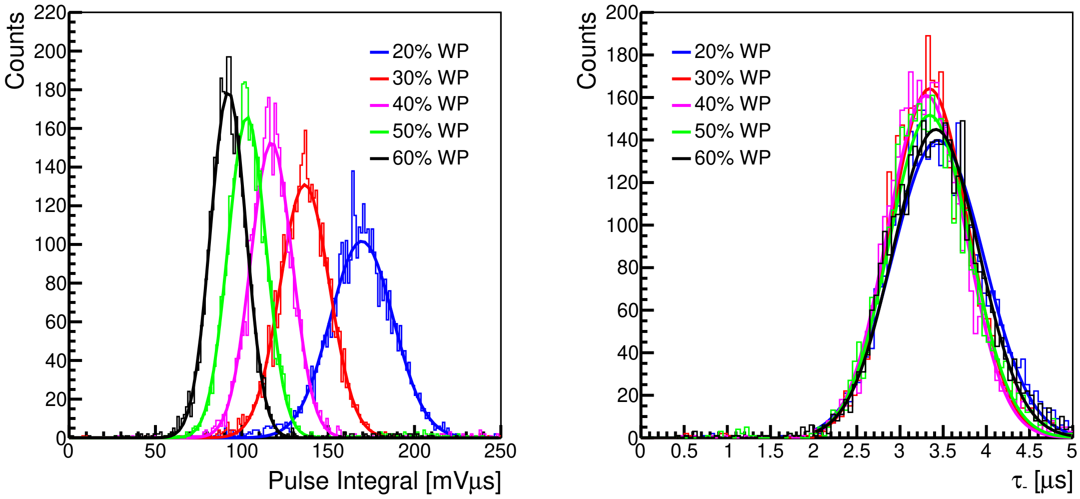

(a)

(b)

Figure 3.4: (a) Distributions of pulse integral (I_{SST}) for the different WPs fitted to a Gaussian function. The means of the distributions decrease with the WP and are shown in Table 3.1. (b) Distributions of decay time for several WPs fitted to a Gaussian function. The means of the distributions remain approximately constant with the WP and are shown in Table 3.1.

Eq. 2.17 can be rewritten as Eq. 3.4:

$$\frac{\alpha}{1+\beta} = \frac{\tau - \tau_-}{\tau_-} \frac{G T_0}{I_0^2 R_0} \tag{3.4}$$

where all parameters are known ($G = 5T_c^4 \Sigma_W V_W$), as $R_L \ll R_0$ and assuming the very sharp transition of the TES, therefore, $T_0 \approx T_c$. The steps from Eq. 2.17 to Eq. 3.4 are shown in appendix A.1.

Moreover, from the proposed resistance dependence on temperature and current in Eq. 3.2, and the definitions of α and β in Eq. 2.4 and 2.5, the following relation between α and β also holds:

$$\frac{\alpha}{1+\beta} = \frac{\frac{T_0}{R_0} \frac{\partial R}{\partial T}\Big|_{I_0}}{1 + \frac{I_0}{R_0} \frac{\partial R}{\partial I}\Big|_{T_0}} = \frac{\frac{T_0}{R_0} \frac{R_N}{\sqrt{2}} \exp\{-x^2\} \frac{1}{\sqrt{2}\sigma_T}}{1 + \frac{I_0}{R_0} \frac{R_N}{\sqrt{2}} \exp\{-x^2\} \frac{\Delta_I}{\sqrt{2}\sigma_T}} \tag{3.5}$$

where $x = \mathrm{erf}^{-1}\{2R_0/R_N - 1\}$. For fitting purposes, Eq. 3.5 is transformed into Eq. 3.8 by redefining the variables involved:

$$x' = \frac{I_0}{R_0}\frac{R_N}{\sqrt{2}}\exp\{-x^2\} \tag{3.6}$$

$$y' = \frac{\tau - \tau_-}{\tau_-}\frac{G}{I_0 R_0} \tag{3.7}$$

then the fitting function is:

$$y' = \frac{x'}{\sqrt{2}\sigma_T + \Delta_I x'} \tag{3.8}$$

The fitting function of Eq. 3.8 is plotted in Fig. 3.5, where the uncertainties in the data points were computed only considering the statistical uncertainties. The results of the fitting provide the parameters $\sigma_T = 7.02 \cdot 10^{-2}$ mK and $\Delta_I = 1.05$ mK/μA.

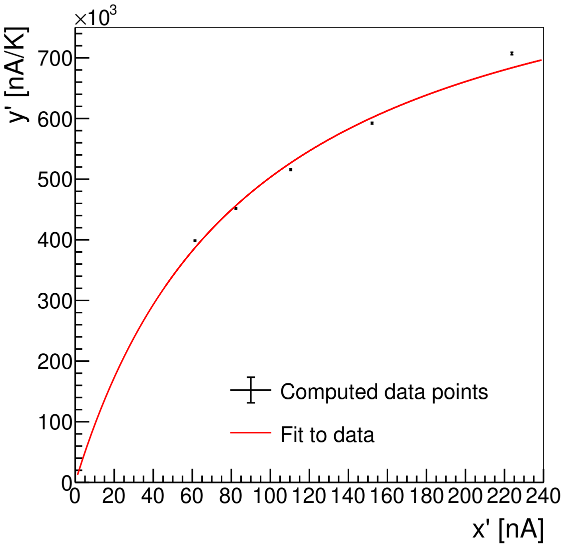

Figure 3.5: Fit of the function defined in Eq. 3.8 to the dependency of y' to x' defined by Eq. 3.7 and Eq. 3.6, respectively.

On the other hand, the energy collection efficiency η for 1064 nm pulses can also be found. The energy collection efficiency is defined as the fraction of the total photon energy which is deposited in the tungsten electron system [73]. This can be computed, considering a 1064 nm photon with energy $E = 1.165$ eV, converting Eq. 2.16 to Eq. 3.9 (see appendix A.2 for detailed derivation). The mean of the data of the pulse integral I_{SST} and decay time τ_- are extracted from the fit in Fig. 3.4a and 3.4b.

$$\eta = I_0 R_0 \frac{\tau}{\tau - \tau_-}\frac{I_{SST}}{E} \tag{3.9}$$

The mean collection efficiency of the five WPs corresponds to $\eta = 0.29$, with a 2 % variation among the WPs. For comparison, a value of $\eta = 0.42$ is reported in [74].

In the following, a summary of the parameters at 30 % WP of the model is made:
TES electrical circuit parameters:

$\mathrm{L} = 20\ \mathrm{nH}$, $\mathrm{R_{SH}} = 20\ \mathrm{m\Omega}$, $\mathrm{R_{PAR}} = 36\ \mathrm{m\Omega}$

$\mathrm{I_{BIAS,\ 30\%}} = 12.2\ \mathrm{\mu A}$, $\mathrm{R_N} = 10.2\ \Omega$, $\mathrm{R_{0,\ 30\%}} = 3.06\ \Omega$

$\sigma_\mathrm{T} = 7.02 \cdot 10^{-2}\ \mathrm{mK}$, $\Delta_\mathrm{I} = 1.05\ \mathrm{mK/\mu A}$

TES thermal circuit parameters:

$\mathrm{C_{W_{e,\ 30\%}}} = 2.43\gamma_\mathrm{W}\mathrm{T_{0,\ 30\%}}/\mathrm{V_m}\rho_\mathrm{W} = 2.6 \cdot 10^{-3}\mathrm{J/kgK}$, $\gamma_\mathrm{W} = 1.3 \cdot 10^{-3}\ \mathrm{J/(mol \cdot K^2)}$,

$\mathrm{V_m} = 9.6 \cdot 10^{-6}\ \mathrm{m^3/mol}$, $\rho_\mathrm{W} = 1.78 \cdot 10^4\ \mathrm{kg/m^3}$

$\mathrm{T_{0,\ 30\%}} \approx \mathrm{T_c} = 140\ \mathrm{mK}$,

$\mathrm{C_{W_{ph}}} = 234\ \mathrm{R_g}(\mathrm{T_{ph}}/\theta_\mathrm{W})^3/\mu_\mathrm{W} \sim 2 \cdot 10^{-7}\mathrm{J/kgK}$, $\mathrm{R_g} = 8.31\ \mathrm{J/molK}$

$\theta_\mathrm{W} = 383\ \mathrm{K}$, $\mu_\mathrm{W} = 1.84 \cdot 10^{-1}\ \mathrm{kg/mol}$

$\Sigma_\mathrm{W} = 0.4\ \mathrm{nW/(\mu m^3 \cdot K^5)}$, $\mathrm{n} = 5$

$$\mathrm{G_{W_{e-ph}}} = \mathrm{V_W}\frac{\partial \mathrm{P_{e-ph}}}{\partial \mathrm{T_e}} \approx \mathrm{n}\Sigma_\mathrm{W}\mathrm{V_W}\mathrm{T_c^{n-1}} = 7.6\ \mathrm{pW/K}$$

TES geometry parameters:

$\mathrm{x_W} = 25\ \mathrm{\mu m}$, $\mathrm{y_W} = 25\ \mathrm{\mu m}$, $\mathrm{z_W} = 20\ \mathrm{nm}$, $\mathrm{V_W} = 12.5\mathrm{\mu m^3}$ $\mathrm{m_W} = 2.2 \cdot 10^{-13}\ \mathrm{kg}$

Silicon substrate thermal circuit parameters:

$\mathrm{C_{Si_{ph}}} = 234\ \mathrm{R_g}(\mathrm{T_{ph}}/\theta_\mathrm{Si})^3/\mu_\mathrm{Si} \sim 6 \cdot 10^{-7}\mathrm{J/kgK}$, $\mathrm{R_g} = 8.31\ \mathrm{J/molK}$

$\theta_\mathrm{Si} = 645\ \mathrm{K}$, $\mu_\mathrm{Si} = 2.81 \cdot 10^{-2}\ \mathrm{kg/mol}$

$\rho_\mathrm{Si} = 2.33 \cdot 10^3\mathrm{kg/m^3}$

$\mathrm{k} = 1/3 \cdot \mathrm{C_{Si_{ph}}} \cdot \mathrm{v} \cdot \mathrm{l} \cdot \rho_\mathrm{Si}$, $\mathrm{T_{ph}} \approx \mathrm{T_{bath}} = 136.7\ \mathrm{mK}$

$\mathrm{v} = 6.4 \cdot 10^3\ \mathrm{m/s}$, $\mathrm{l_{pure}} = 275\ \mathrm{\mu m}$

$\mathrm{k_{pure}} = 1/3 \cdot \mathrm{C_{Si_{ph}}} \cdot \mathrm{v} \cdot \mathrm{l_{pure}} \cdot \rho_\mathrm{Si} = 8.2 \cdot 10^{-4}\ \mathrm{W/(m \cdot K)}$, $\mathrm{H_c} = 184\mathrm{W/(m^2K)}$

$\mathrm{G_{apiezon}} = \mathrm{H_c A_{Si}} = \mathrm{H_c} \cdot \pi(\mathrm{d_{Si}}/2)^2 = 903\ \mathrm{\mu W/K}$

Silicon substrate geometry parameters:

$\mathrm{d_{Si}} = 2.5\ \mathrm{mm}$, $\mathrm{z_{Si}} = 275\ \mathrm{\mu m}$, $\mathrm{y_{Si}} = 0.8\ \mathrm{mm}$, $\mathrm{x_{Si}} = 2.5\ \mathrm{mm}$, $\mathrm{m_{Si}} = 10^{-9}\ \mathrm{kg}$

3.4 COMSOL simulation

Considering the components and the calibration of the TES aforementioned, the TES simulated with COMSOL behaves as the system described in section 2.1. The current circulating through the TES computed with COMSOL is converted to voltage using $1/\mathrm{a_{VtoI}}$, defined before, to emulate the output of the SQUIDs readout. Additionally, as mentioned in section 2.2.2, the SQUID readout response can be approximated to a first-order low-pass filter, and this has been implemented in the simulation with a cut-off frequency of 350 kHz. Moreover, in the data taken with the TES in the different setups explained in section 2.3, the DC component of the voltage from the SQUIDs is removed. This effect in the TES signal is equivalent to the appearance of a high-pass filter with a cut frequency of approximately 1 kHz.

3.4.1 1064nm photon

The calibration of the COMSOL simulation is checked by comparing the expected signal produced by a 1064 nm photon with measured 1064 nm photon pulses. To simulate the effects of a 1064 nm photon in the TES, an energy of $\eta \cdot E_{1064\mathrm{nm}} = 0.29 \cdot 1.165$ eV is deposited in the tungsten electron system through a heat load. The simulated signal is in good agreement with measured data, as shown in Fig. 3.6.

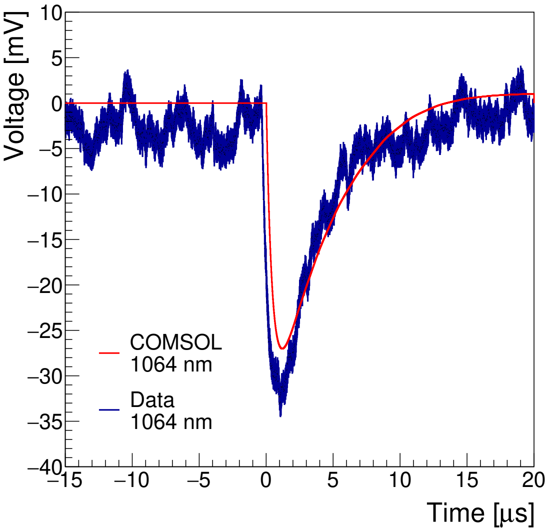

Figure 3.6: 1064 nm photon simulated with COMSOL compared to a 1064 nm photon extracted from measurement data.

3.4.2 TES linear response

As done with 1064 nm, the effect of other wavelengths in the TES can be evaluated in the simulation. This could be used as a predicted calibration of the response of the TES to different wavelengths without the necessity of a linearity measurement. The pulses from the response of the simulated TES to an energy $\eta \cdot E_x$ of the pulse with wavelength x is shown in Fig. 3.7a, with η assumed constant for different energies.

Fig. 3.7b shows how the pulse integral and the pulse height of the pulse computed from the fitting procedure behave depending on the energy. It can be clearly seen that the pulse integral presents a more linear behavior than the pulse height. Section 6.2 will discuss this in more detail.

3.4.3 Energy deposition in silicon substrate

The silicon substrate phonon system is weakly coupled to the TES electron system. Therefore, it is expected that the production of a considerable signal in the TES would require a much higher energy deposition in the silicon. The energy deposition is done with a heat load

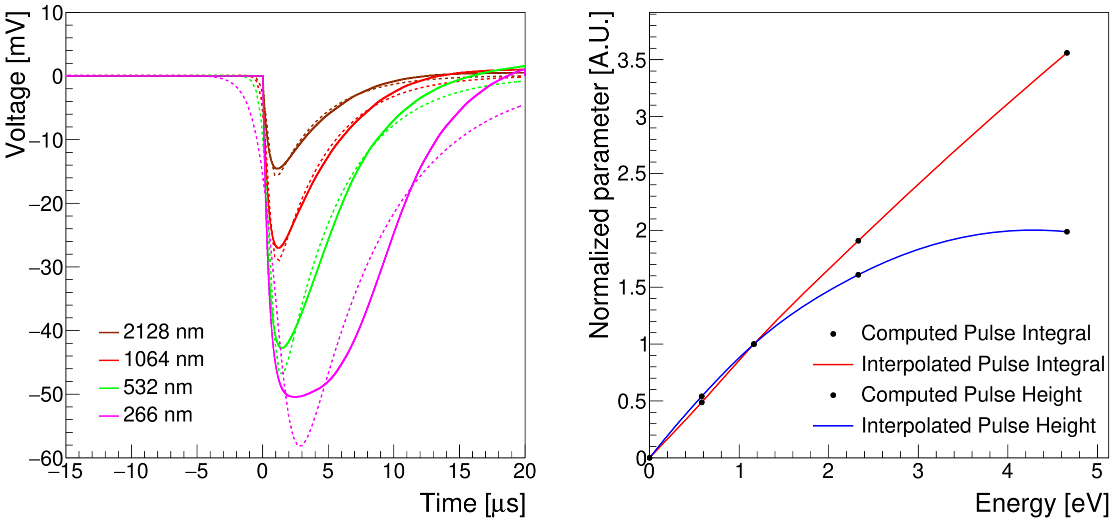

(a) (b)

Figure 3.7: (a) Pulses simulated with COMSOL (solid line) and fitting of the function defined in Eq. 3.1 (dashed line) to the pulses. In this case, the TES saturates with a 266 nm (4.66 eV) photon, and the function no longer fits the pulse well. (b) Comparison of the linear behavior of the pulse integral and the pulse height computed from the fitting procedure of the simulated pulses using Eq. 6.6.

defined by the energy E multiplied by a normalized 3D Gaussian distribution with displacement from the TES $x_0 = r$, $y_0 = 0$ and $z_0 = -100$ µm, where r is the radial distance to the TES, and spread given by $\sigma = 100$ µm. This considers a cloud of heat instead of a Dirac delta energy deposition in one point of the silicon. The cloud emulates the heat propagation in the first nanoseconds from the Dirac delta energy deposition. This does not introduce any significant distortion in the results but greatly improves the convergence of the simulation.

The heat propagation is computed using Fourier's heat transfer law, the default configuration of COMSOL [57]. This introduces an error in the simulation, as Fourier's law overestimates the heat flux when the mean free path of the phonons is in the order of the dimensions of the material [75, 76]. As evidenced in [77], high-energy phonons can also produce a signal in the TES, and their movement inside a crystal structure is not well described by finite element methods. As the impurities in the silicon substrate reduce the mean free path, the lower k_{corr} is, the more suitable Fourier's law is for the simulation. Currently, k_{corr} is a free parameter, and the uncertainty from using this method is difficult to assess. The results from [70] indicate that a value of $k_{corr} < 0.1$ could be expected for millikelvin temperatures. Several values of k_{corr} lower than 0.1 are tested in the simulation.

Fig. 3.8 shows the response of the simulated TES to energy deposition in the silicon substrate in the order of the keV for $k_{corr} = 0.03$ and $k_{corr} = 0.015$.

It can be seen that a high-energy deposition in the silicon substrate is able to produce a signal in the TES. If Eq. 3.1 is fitted to the signal, the parameters A, τ_{rise} and τ_{decay} can be extracted to characterize the signal shape. The parameters A, τ_{rise} and τ_{decay} depend on the value of k_{corr}, E and r. For r = 0.4 mm and E = 10 keV, the signal is slower and has a higher amplitude for a lower value of k_{corr}. However, with a higher distance to the TES, the pulses become slower but reduce their amplitude, as the perturbation produced by the energy deposition takes longer to arrive at the TES. A description of the overall behavior of

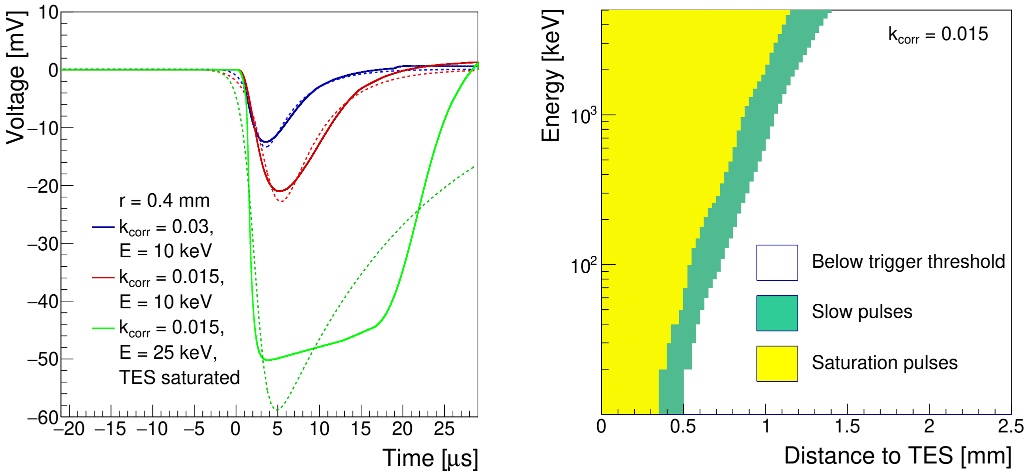

(a) (b)

Figure 3.8: (a) Pulses resulting from the simulation of energy deposition in the silicon substrate at a distance of 0.4 mm from the TES. The blue curve represents an energy deposition in the silicon substrate of 10 keV with $k_{corr} = 0.03$ (correction to the mean free path of the phonons). For the same energy deposition but $k_{corr} = 0.015$, the corresponding signal (red curve) is slower and has a higher amplitude. The green curve shows the response of the TES for an energy deposition of 25 keV, which is high enough to saturate the TES. The three curves are fitted to the phenomenological model given by Eq. 3.1. While the slow pulses (blue and red curves) are approximately well described by the fitting function (blue and red dashed curves, respectively), it does not fit the saturated pulses (green dashed curve) correctly. (b) Shown are regions for pulses that do not pass a trigger threshold of -20 mV (white), slow pulses (green) and saturation pulses (yellow) in the space of energy versus distance to the TES computed for $k_{corr} = 0.015$.

E(keV)	r(mm)	k_{corr}	A(mV)	τ_{rise}(µs)	τ_{decay}(µs)
1064 nm	0 (TES)	-	18.4	0.25	3.9
10	0.4	0.03	10.8	0.84	3.9
10	0.4	0.015	19.5	1.38	4.8
10	0.5	0.015	9.1	1.42	5.5
25	0.4	0.015	35.5	0.87	18.2

Table 3.2: Fit parameters from pulses resulting from energy depositions with energy E, distance from the TES r, and correction to the mean free path of the phonons k_{corr}. A 1064 nm photon pulse (1.2 eV) is not affected by the k_{corr} value, and the energy is deposited on the TES itself.

the fit parameters while changing k_{corr}, E and r can be seen in Table 3.2.

For an energy sufficiently high, the temperature of the TES phonon system strives to overcome the temperature of the electron system. The simulation increases the energy flow between the phonon and the electron system so that $T_e >= T_{ph}$. This suddenly increases the temperature of the electron system, and then the TES becomes saturated, as shown in

Fig. 3.8 (green curve). The phenomenological function given by Eq. 3.1 is not designed to fit this kind of pulse, so it does not describe the resulting shape.

It is important to note that the saturation of the simulated TES is reached at a voltage of -50 mV, in disagreement with measured data which goes up to -70 mV. However, the data was taken at 30 % WP of the TES, with a current circulating through the TES at steady state $I_0 = 92.8$ nA. From solving the circuit in Fig. 3.2a, the maximum pulse height should be given by the following equation, which is the voltage level when the TES is normal conducting.

$$h_{max} = \frac{I_0 - I_N}{a_{VtoI}} = \frac{I_0}{a_{VtoI}}\left(1 - \frac{R_0}{R_N}\right) \tag{3.10}$$

In Eq. 3.10, I_N is the current circulating through the TES in saturation. Then, the measured voltage in saturation should be $h_{max} = 49.2$ mV. This means that a scale factor should be applied to convert the measured output voltage from the SQUID readout to the current variation produced due to a TES pulse. This effect is probably caused by the different impedances in the measurement setup. As the cause of this is unknown, the scale factor is not applied to the measured intrinsic data or to the simulated pulses.

From the simulation of pulses with energy deposition in the silicon substrate at different values of E, r, and k_{corr}, three regions are defined according to the pulse shape and amplitude: pulses which do not pass a trigger threshold, slow pulses (with higher τ_{rise} and τ_{decay} than 1064 nm pulses), and saturation pulses (reach the saturation level). Fig. 3.8b shows the distribution of these three regions for a value of $k_{corr} = 0.015$ and trigger threshold at 20 mV, the same used to take the intrinsics data. The colored region, where the generated pulses pass the trigger threshold, is defined as the TES sensitive region in the silicon substrate. Furthermore, if the fitting procedure is applied to pulses originating from different values of E and r, as done in Fig. 3.8a, a map describing the values of the fit parameters $A(r, E)$, $\tau_{rise}(r, E)$ and $\tau_{decay}(r, E)$ is obtained. The pulse height is computed as the minimum of the fitting function defined by Eq. 3.1 with the parameters A, τ_{rise} and τ_{decay}.

3.5 Geant4 simulation

In order to compute the energy deposited in radioactivity events and muons from cosmic rays, a simulation with Geant4 [58] was implemented. As shown in Fig. 2.4b, the TES module is located in the bottom stage of the cryostat (25 mK) attached to a cold finger. An aluminum can encloses the TES module with the cold finger to protect the TES and the SQUIDs from external electromagnetic interference. For the geometry of the simulation, the aluminum can, the cold finger and the TES module have been constructed, as shown in Fig. 3.9b. In the simulation, the TES faces the ceiling, recreating the conditions of the intrinsic data run used to evaluate the simulation results.

The track of the particles passing through the silicon substrate with the energy deposition along the track is recorded. The mean distance of the track to the TES is computed as $\bar{r} = |\sum E_i \vec{r}_i| / E_{total}$, where $\vec{r}_i$ is the position of a point in the track and E_i the energy deposition at that point produced by the particles in the simulation.

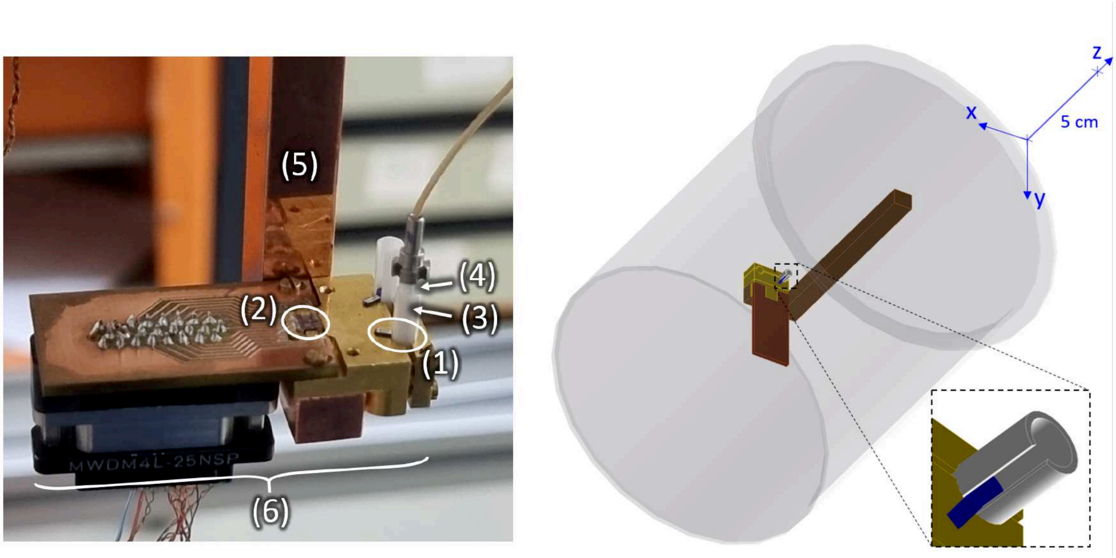

(a)

(b)

Figure 3.9: (a) Cold finger (5) with module with two TESs (1) and two SQUID chips (2). Example configuration of the module (6) facing the lab's ceiling. The orientation of the module depends on the geometry of the cold finger. The optical fiber is coupled and aligned to the TES employing a zirconia sleeve (3) present in the module and a zirconia ferrule in the fiber (4) as described in [78]. (b) 3D visualization of the parts inside the aluminum can in the cryostat. The blue line in the top right corner is in the direction of the Z-axis and indicates the scale of 5 cm. The module is in a cold finger attached to the bottom of the mixing chamber plate of the cryostat. The silicon substrate where the sensor is located is kept in place by a sapphire rod and a zirconia fiber sleeve.

3.5.1 Cosmic rays

The muons from cosmic rays are simulated following the distribution f_μ in energy E and azimuthal angle θ given by Eq. 3.11 according to [79].

$$f_\mu(E,\theta) = I_0 N (E_0 + E)^{n-1} \left(1 + \frac{E}{\epsilon}\right)^{-1} \cos^2\theta \tag{3.11}$$

Here, $I_0 = 70.7\ \mathrm{m^{-2}s^{-1}sr^{-1}}$ is the muon flux for $\theta = 0$, N is a normalization factor to make the integral of the function equal to 1, $E_0 = 4.29$ GeV is a parameter that accounts for the energy loss, and $n = 3.01$ and $1/\epsilon = 1/854\ \mathrm{GeV^{-1}}$ are additional parameters for the fit to data in [79]. The muons are considered uniformly distributed in the polar angle. For the simulation of the interaction with the silicon substrate, the muons are directed to a larger area A_{sim} than the silicon substrate, which includes it. The effective area of the silicon substrate A_{eff} is then computed from the ratio between the hits N_{dep} vs the total number of events N_{total}, by means of $A_{eff} = A_{sim}N_{dep}/N_{total}$. Considering a flux of cosmic muons of 70 $\mathrm{m^{-2}s^{-1}sr^{-1}}$ close to the Earth's surface [80], the computed rate of muons hitting the substrate is $4.22 \cdot 10^{-4}$ cps. The distribution of energy deposition in the silicon substrate versus the distance to the TES is shown in Fig. 3.10.

The energy deposited by the muons in the silicon substrate is mostly between 60keV and 160keV, with the most likely value at 80keV.

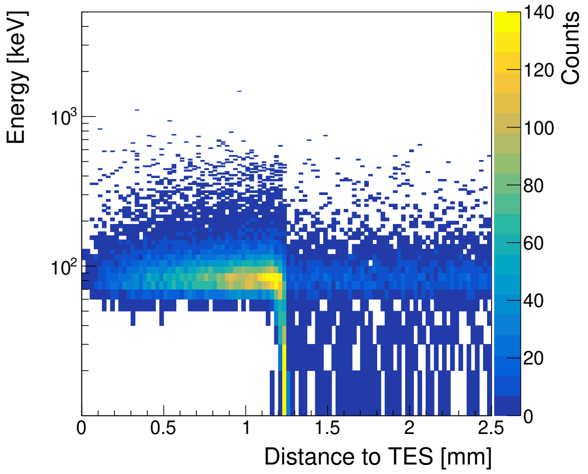

Figure 3.10: Distribution of the deposited energy in the silicon substrate as a function of the mean distance to the TES computed with Geant4 for muons. The most likely value of energy deposited by muons is 80 keV, but the extreme cases can reach energy deposition in the order of 1 MeV. At a distance to the TES of 1.25 mm, corresponding to the boundary between the zirconia and the silicon substrate (Fig. 3.2 and Fig. 3.3), the muons scatter in and out of the silicon substrate. Therefore, the energy deposition in this region is smaller compared to smaller distances to the TES.

3.5.2 Radioactive materials

The presence of radioactive nuclei in zirconia has been widely studied [81]. Therefore, the zirconia fiber sleeve shown in Fig. 3.2b and 3.9a is investigated as a possible radioactive source. The decay of the Uranium-238 and Thorium-232 series and Potassium-40 (Fig. 3.11) from the zirconia material [81] is simulated with a uniform distribution in the fiber sleeve and isotropic angular distribution.

The distribution of energy deposition in the silicon substrate from radioactivity in the zirconia versus the distance to the TES is shown in Fig. 3.12. Below 1 MeV, the distribution is dominated by the interaction of electrons from the beta decay occurring in the decay series and the photons produced by the deexcitation of the nuclei and the fluorescence of zirconium. Above 1 MeV, alpha particles dominate the spectrum as they deposit their whole energy in the substrate once they hit it.

The lower bound and the upper bound for the rate of events which deposit energy in the silicon substrate can be computed with Eq. 3.12 and Eq. 3.13, respectively:

$$\mathrm{rate_{low}} = \sum_{\mathrm{j}} \mathrm{min(A_j) N_{j,dep}/N_{j,total}} \tag{3.12}$$

$$\mathrm{rate_{up}} = \sum_{\mathrm{j}} \mathrm{max(A_j) N_{j,dep}/N_{j,total}} \tag{3.13}$$

Here, the radioactive nuclei reported in [81] present in zirconia are considered. The variables correspond to j the jth nucleus, $\mathrm{min(A_j)}$ and $\mathrm{max(A_j)}$ the minimal and maximal activity reported for that nucleus, $\mathrm{N_{j,dep}}$ the number of events which deposit energy and $\mathrm{N_{j,total}}$, the total number of events simulated for that nucleus. The resulting rates of events depositing

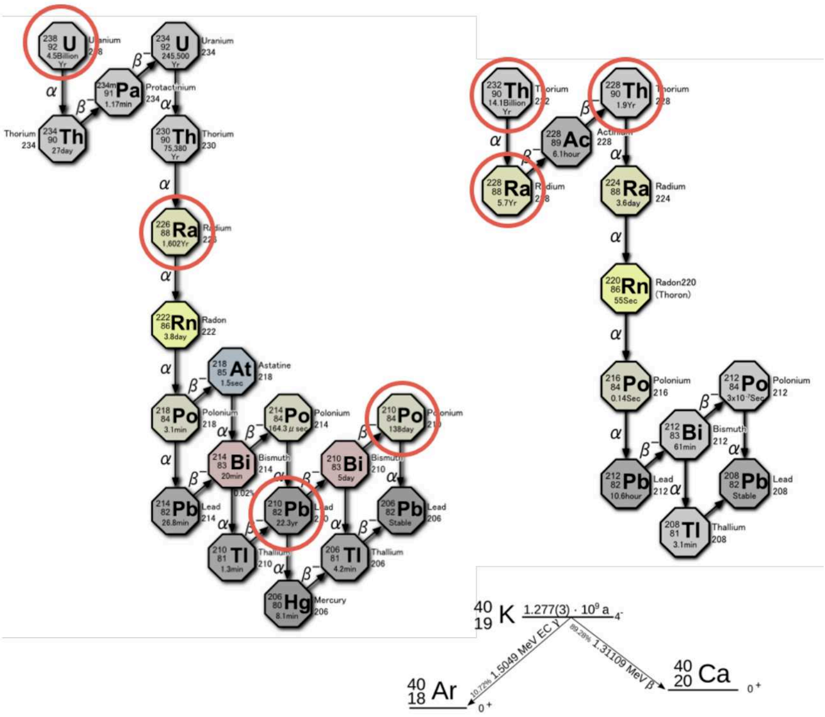

Figure 3.11: Radioactive series of Uranium-238 and Thorium-232 and radioactive decay of Potassium-40. The isotopes circled in red are incorporated together with the Uranium and Thorium during the extraction and production of the zirconia [81]. [Adapted from Wikimedia Commons]

energy in the silicon substrate for the radioactivity in zirconia are between $1.08 \cdot 10^{-2}$ cps and $6.92 \cdot 10^{-2}$ cps.

3.6 Combination of Geant4 and COMSOL simulations

The information of the energy deposition E at a mean distance to the TES, $\bar{r}$, in Fig. 3.10 and 3.12, obtained using Geant4, is folded with the results from the COMSOL simulation in Fig. 3.8b, with $k_{corr} = 0.015$, and the map describing the values of the fit parameters $A(r, E)$, $\tau_{rise}(r, E)$ and $\tau_{decay}(r, E)$. The use of $\bar{r}$ from Geant4 implies that the track information is lost. However, this allows the replication of most events while simplifying the simulation and reducing the number of simulated events in COMSOL. Furthermore, this approach assumes that the energy deposition happens fully in the form of heat and is relatively fast ($0.1\mu s$) compared to the decay time of the pulses (> 3 μs). The energy deposition of radiation in a material is a more complex process [82]. In reality, the energy deposition would also form electron-hole pairs in the silicon substrate, which would also heat the material, but with a delay given by the lifetime of the pairs. The lifetime of the electron-hole pairs in silicon is in the order of microseconds or higher depending on impurities [83]. This means that the simulation underestimates the decay time of the pulses resulting from an energy deposition in the silicon substrate.

The result of the folding of the spectrum in Fig. 3.10 and 3.12 with the sensitive region of the TES from Fig. 3.8b gives the expected rate of events that pass the trigger threshold of

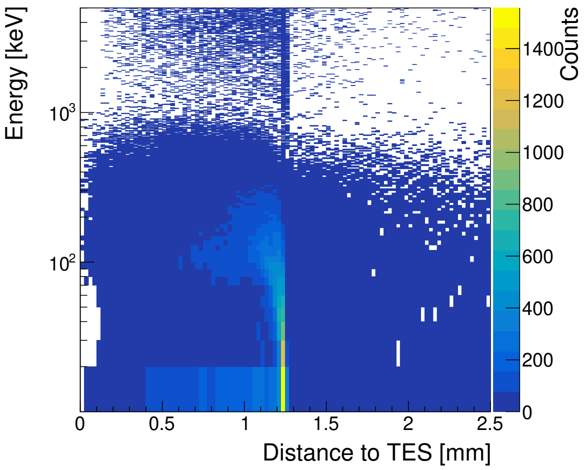

Figure 3.12: Distribution of the deposited energy in the silicon substrate as a function of the mean distance to the TES computed with Geant4 for radioactivity in the zirconia. The region below 1 MeV mainly presents energy deposition from beta and gamma decays of the simulated radioactive isotopes in the zirconia fiber sleeve. The region above 1 MeV is produced by energy depositions from the alpha decays. As the alpha particles do not penetrate the material, a population can be seen at a distance to the TES of 1.25 mm, corresponding to the boundary between the zirconia and the silicon substrate (Fig. 3.2 and Fig. 3.3). A cloud is also observed at the boundary at low energies consisting of low energetic gamma and beta particles which do not penetrate the substrate.

20 mV. The expected rate for muons from cosmic rays is $1.2\cdot 10^{-4}$ cps, and for the radioactivity from zirconia, the rate is between $3.3 \cdot 10^{-3}$ cps and $2.14 \cdot 10^{-2}$ cps considering the lower and upper bounds. Therefore, the intrinsic background rate measured with the TES can be explained by the radioactivity in the zirconia fiber sleeve within limits, contributing one order of magnitude more than the muons to the intrinsic background rate.

As aforementioned, the results from Fig. 3.10 and 3.12 are also folded with the map of fit parameters $A(r,E)$, $\tau_{rise}(r,E)$ and $\tau_{decay}(r,E)$. The pulse height is computed as the minimum of Eq. 3.1 with the corresponding combination of $A(r,E)$, $\tau_{rise}(r,E)$ and $\tau_{decay}(r,E)$. Fig. 3.13a and 3.13b show the 2D distribution of the pulse height and the decay time parameters from the simulation of radioactivity in zirconia and cosmic muons, respectively.

It can be seen that the distributions for the radioactivity and the muons are very similar. The distributions can be divided into regions according to the ones defined in Fig. 3.8b. Close to 8 µs of decay time and between 20 mV and 50 mV of pulse height, the slow pulse region defined in section 3.4.3 can be found. Then, the saturation region is found above 50 mV in Fig. 3.13a and 3.13b, and an artificial increase of the pulse height beyond the saturation level at 50 mV is observed. Afterwards, τ_{decay} increases to its upper limit at 100 µs, while the pulse height converges to the saturation level.

The same features can be observed in the corresponding distribution for the intrinsic background extracted from data as shown in Fig. 3.14a, where the same column of slow pulses is observed around 10 µs, and then the transition to the saturation pulses over 70 mV of pulse height. The possible cause of the discrepancy in the saturation levels was discussed in section 3.4.3. Under 70 mV of pulse height, the distribution in data extends to higher decay times. At the moment, this is not described in the simulation.

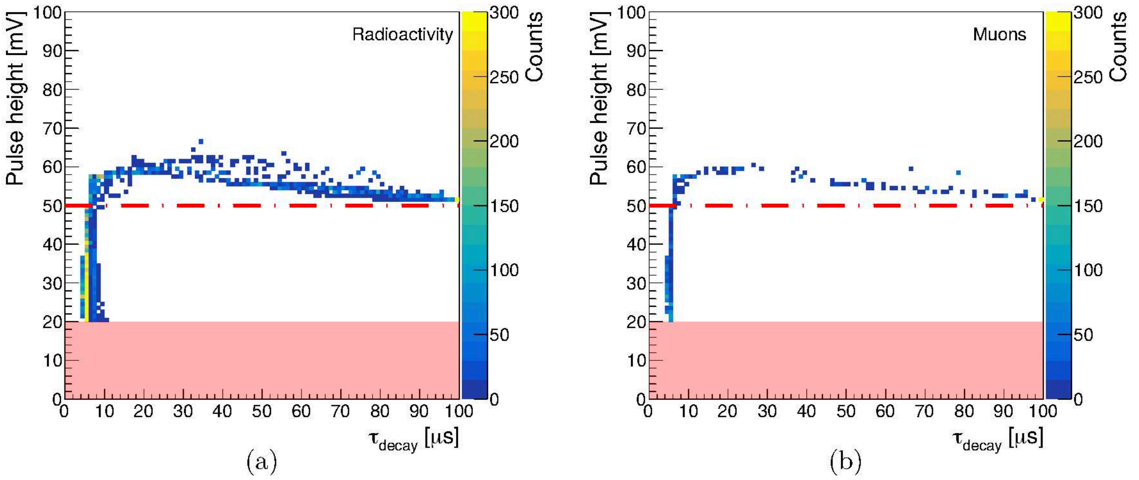

(a) (b)

Figure 3.13: 2D distribution of the pulse height and the decay time computed from the fit of Eq. 3.1 to the pulses simulated with COMSOL Multiphysics in the case of (a) radioactivity in the zirconia, (b) muons from cosmic rays. The red shaded area indicates the region below the trigger threshold. The dashed line indicates the transition from slow pulses to saturated pulses.

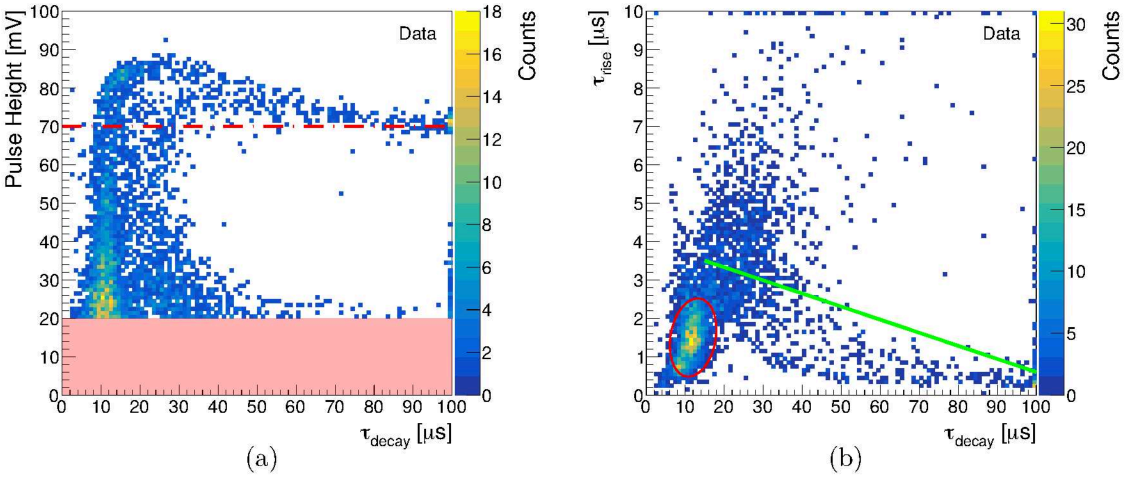

(a) (b)

Figure 3.14: 2D distribution from the fit of Eq. 3.1 to the pulses from an intrinsics data sample taken for 50 h. Distribution of (a) Pulse height vs decay time, (b) Rise time vs decay time. In (a), the red shaded area indicates the region below the trigger threshold. The dashed line indicates the transition from slow pulses to saturated pulses. In (b), the red circle indicates the region of slow pulses, and the green line follows the pattern of the saturated pulses.

Fig. 3.15a and 3.15b show the 2D distribution of the rise time and the decay time parameters from the simulation of radioactivity in zirconia and cosmic muons, respectively.

In this case, the radioactivity and muon distributions are also very similar. Similar to the explained previously, Fig. 3.15a and 3.15b can also be divided into regions. The region close to 8 µs of decay time but between 1 µs and 3 µs represents the slow pulse region, followed by the saturation region. In the saturation region, the fitting function fails to describe the saturation pulses, so the rise time increases up to 4 µs while the decay time increases. After

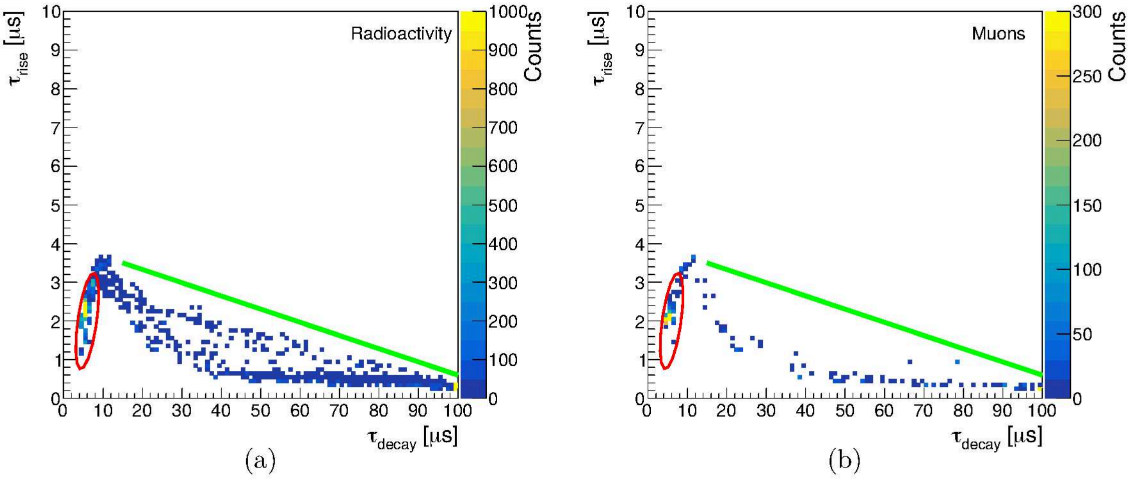

(a) (b)

Figure 3.15: 2D distribution of the rise time and the decay time computed from the fit of Eq. 3.1 to the pulses simulated with COMSOL Multiphysics in the case of (a) radioactivity in the zirconia, (b) muons from cosmic rays. The red circle indicates the region of slow pulses, and the green line follows the pattern of the saturated pulses.

that, the rise time decreases, and the decay time increases until it reaches its upper limit at 100 μs.

The simulation does not explain the extension of the distribution to higher decay and rise times. However, the rise and decay time distribution in simulation resembles what happens in the data shown in Fig. 3.14b. Although very dispersed, a similar distribution is observed. The discrepancy could be explained by the electronic noise present in the data, which was not included in the simulation. The effect of the electronic noise in the data will be discussed in chapter 5 for the case of 1064 nm photons.

Overall, the simulation can explain the background rates from the intrinsics data and identify different event classes, but it fails to explain the balance between the slow and saturation pulse regions. Considering the slow and saturation regions defined before, the simulation underestimates the rate of slow pulses compared to data, while the opposite happens with the saturation pulses.

3.7 Evaluation of results

The results from the simulation combining COMSOL and Geant4 point to the zirconia as the main contributor to the energy depositions in the TES substrate over the muons. The expected rate of events from the simulation is compatible with the background data within the limits.

Based on the results, three approaches are proposed to reduce the intrinsic background in the TES:

- Reduction or removal of the zirconia fiber sleeve. This would be only practical in the studies for direct dark matter searches within the TES [84], given that this would drastically reduce the efficiency of the TES due to the loss of direct alignment between the fiber and the TES chip.

- Substitution of the zirconia for a more radiopure material.
- Reduction of the volume where an energy deposition produces a signal in the TES. This could be realized with the TES located on a membrane as described in [85]. The TES would be suspended in the membrane over a gap in the silicon substrate. This would reduce the volume of the substrate in the vicinity of the TES.
- Implementation of a veto detector for background discrimination with the same or greater active volume than the TES. The events in the veto would be in coincidence with the ones in the TES, allowing their discrimination from the signal.

Further investigations will be dedicated to improving the accuracy of the simulation. Several phenomena, such as high-energy phonons, the particle tracks from Geant4, electron-hole pair propagation, and electronic noise, could be considered to achieve this goal.

CHAPTER

4

SIMULATION OF BLACK BODY RADIATION AS MAIN PHOTON-LIKE CONTRIBUTOR TO EXTRINSIC BACKGROUND

Contents

Compared to the intrinsic background explained in the previous chapter, an additional contribution in the form of Black Body radiation and luminescence photons appears in the extrinsic background. This is a consequence of connecting the optical fiber to the sensor, with the other end in a dark, room-temperature environment outside the cryostat, as discussed in section 2.2. In [86], the Black Body radiation is confirmed as the main contributor to the extrinsic background. In the scope of this thesis, a framework for the simulation of Black Body radiation in the TES has been developed, which is able to adapt to different experimental conditions. This chapter will discuss the simulation of this new population of events and its comparison with a background measurement.

4.1 Simulation of Black Body Radiation

A model for the simulation of Black Body Radiation (BBR) in the TES is built by considering the possible optical components in the TES setup in addition to the theory of BBR production. The individual parts of the simulation will be explained in the following sections. First, an overview of the computation of the distribution of a Black Body radiator will be given, followed by a description of the effects of the different optical components for the resultant rate computed at the TES.

4.1.1 Production of Black Body Radiation

Perfect Black Body

A perfect black body radiator is an idealized object that absorbs all electromagnetic radiation that falls on it, regardless of frequency or angle of incidence. It does not reflect or transmit any part of the incident radiation. According to Kirchhoff's law of thermal radiation, for an object in thermal equilibrium, the emissivity (a measure of how well a body emits radiation) must equal its absorptivity (how well it absorbs radiation) [87]. Therefore, it is also an ideal emitter of radiation.

A good model to visualize this is a cavity with ideally reflecting walls with a small aperture at a temperature T. The walls reflect a photon entering the cavity, and the probability of exiting once more through the hole is very small. Therefore, it will be a perfect absorber. The photons leaving the cavity follow Planck's distribution [87]. The photons have an energy E following a spectral probability density given by Eq. 4.1, which is a function of the photon's energy and the temperature T.

$$\mathrm{B(E,T)} = \frac{2}{\mathrm{h^3c^2}}\frac{\mathrm{E}^2}{\exp\{\frac{\mathrm{E}}{\mathrm{kT}}\}-1} \tag{4.1}$$

$\mathrm{B(E,T)}$ represents the rate of photons emitted by the hole per unit area and energy in units of photon/($\mathrm{eV \cdot s \cdot m^2 \cdot sr}$), h is the Planck constant, c the speed of light and k the Boltzmann constant. The hole in the cavity would act as a perfect Black Body radiator [87]. The angular distribution of emitted photons will follow Lambert's cosine law, i.e. the rate emitted in an infinitesimal solid angle is given by $\mathrm{B(E,T)}\cdot\cos\theta$, where θ is defined according to Fig. 4.1.

The flux of photons entering and exiting the cavity must be the same [88]. That means that if an optical element occupies the place of the hole in the cavity, the flux photons coupling to the optics would be equal to the photons which would be emitted at its surface. The rate of photons entering such an optical element will be determined by its surface area A, and the efficiency $\eta_\mathrm{e}(\mathrm{E},\theta)$ of the coupling depending on the energy of the photon E and the incidence angle θ. It can be computed using:

$$\mathrm{N(E,T)} = \iint_{\mathrm{A},\Omega} \mathrm{B(E,T)}\eta_\mathrm{e}(\mathrm{E},\theta)\cos\theta\,\mathrm{d}\Omega\,\mathrm{dA} \tag{4.2}$$

Non-perfect Black Body

The previous expression can be generalized for the case of a partially transparent body with reflecting surfaces. In [89], a one-dimensional object is considered for simplicity. BBR

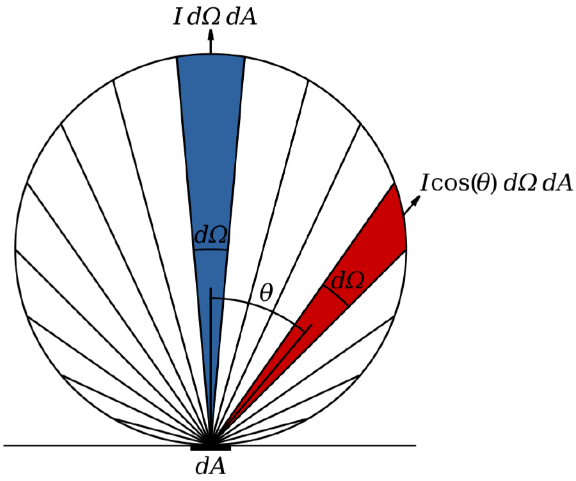

Figure 4.1: Scheme of the flux emitted in a solid angle by a Lambertian radiator. The flux depends on the angle θ between the normal to the surface and the direction of emission [Taken from Wikimedia Commons].

is produced inside the object depending on its absorptivity and emissivity, then part of it is absorbed as it travels to the surface, a fraction is emitted at the surface, and the rest is reflected back to the object. The reflected light repeats this process until all of it is absorbed. Considering then the object length L, a transmission t(E, T) between the surfaces can be computed, which depends on the object's energy and temperature. Considering the reflectivity at the surface as R(E, T), the BBR emitted by the object at the surface follows:

$$B_{np}(E,T) = \frac{[1-R(E,T)][1-t(E,T)]}{1-R(E,T)t(E,T)}B(E,T) \tag{4.3}$$

If this body were a perfect Black Body, the light produced inside it would be reabsorbed at the same time without traveling to the surface. Then, the flux at the surface would be given by B(E, T).

4.1.2 Optical components

TES absorbance

The quantum efficiency of the TES under study would be in the order of 30 % if bare tungsten were used [42]. With the inclusion of a cavity-like coating structure around the sensor, the efficiency can be raised up to 99.68 %, as seen in Fig. 4.2a, if it is optimized for the desired wavelength, here 1064 nm. This is shown in the reflectivity of the optical stack in Fig. 4.2a, where the reflectivity is near zero in the 1064 nm region. The coating structure consists of a highly reflective mirror at the bottom and non-absorbing dielectrics to increase the light absorption in the sensor [90].

To facilitate computation, Eq. 4.4 is used as an approximation to Fig. 4.2a, where $1-\eta_{TES}(E)$ represents the reflection fraction and $\eta_{TES}(E)$, the absorbance of the TES. To approximate the TES reflection curve, the error functions in f_1 and f_2 are combined, acting as a band-pass filter.

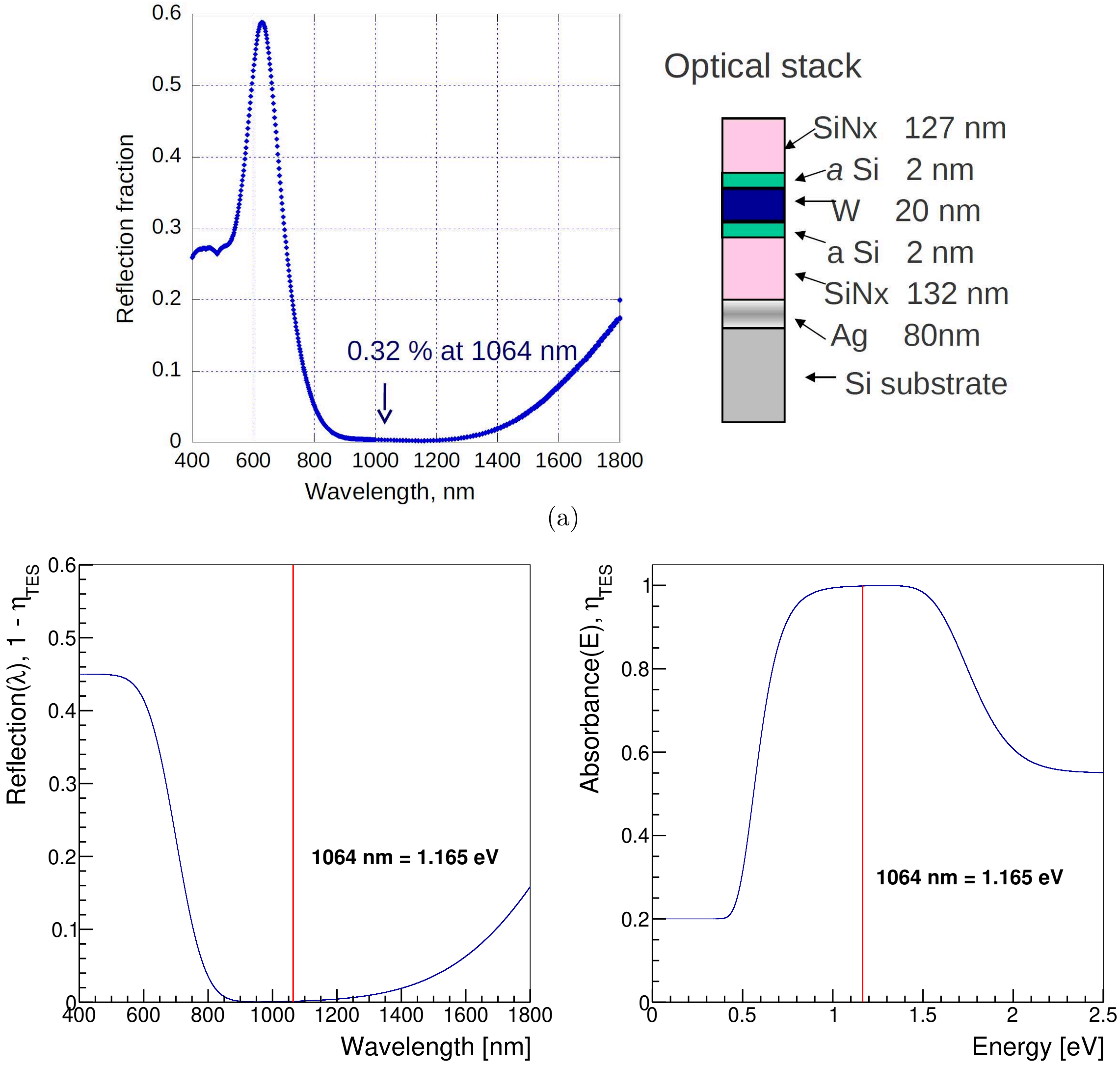

(a)

(b)

(c)

Figure 4.2: (a) On the left, the reflectance of the TES optical stack as a function of the wavelength of the arriving photon is shown. On the right, the thickness of the layers on the optical stack is shown. Image taken from [51]. (b) Approximated reflectance of the TES as implemented in the BBR simulation. (c) The absorbance of the TES as a function of energy computed from the reflectance.

$$\begin{aligned} 1-\eta_{\mathrm{TES}}(E) &= f_1(E)\cdot f_2(E) \\ f_1(E) &= \frac{1-b_1}{2}\left(1+\mathrm{erf}\left\{a_1(\lambda(E)-\lambda_1)\right\}\right)+b_1 \\ f_2(E) &= \frac{1-b_2}{2}\left(1-\mathrm{erf}\left\{a_2(\lambda(E)-\lambda_2)\right\}\right)+b_2 \end{aligned} \tag{4.4}$$

This assumes that the reflection fraction would have a valley at the wavelength for which the TES was optimized and would be flat in the extremes, reaching a maximum reflection. Therefore, in Eq. 4.4, $\eta_{\mathrm{TES}}(E)$ converges to b_1 for high energies (small wavelengths) and to

b_2 for low energies (large wavelengths), as seen in Fig. 4.2c. The values of a_1 and a_2 modify the width of the step of the error functions, and λ_1 and λ_2 control the center of the step. The parameters are chosen such that the modeled reflection (Fig. 4.2b) resembles the shape of the reflection fraction in Fig. 4.2a.

Fig. 4.2c shows the modeled absorbance as a function of energy and is one of the components of the simulation.

The function in Eq. 4.4 could be adapted to better adjust to Fig. 4.2a. However, the difference between Fig. 4.2a and 4.2b does not introduce an error in the simulation, given that for wavelengths lower than 650 nm the rate of BBR photons is several orders of magnitude lower, as a consequence of the exponential form of Eq. 4.1. For wavelengths higher than 1800 nm, the data to model the TES absorbance is not available. Nevertheless, the BBR photons arriving at the TES with these wavelengths are suppressed by several orders of magnitude by bending the optical fiber, as will be seen in section 4.2. Therefore, the approximation in Eq. 4.4 does not affect the simulation results.

Fiber transmission

The fiber transmission is computed from the loss per kilometer of optical fiber depending on the wavelength of the guided photons, without considering coupling or bending losses. To minimize the loss of 1064 nm photons, a HI-1060 optical fiber from Corning is currently implemented in the TES setup. Its loss per kilometer is shown in Fig. 4.3a, and the values out of the range in the x-axis are computed by extrapolating using a linear function. Afterwards, the transmission $\eta_{\mathrm{fiber}}(E, l)$ as a function of the energy of the propagating photon E is calculated for a given length of l meters of optical fiber. Fig. 4.3b shows the transmission for 4 m of the HI-1060 fiber.

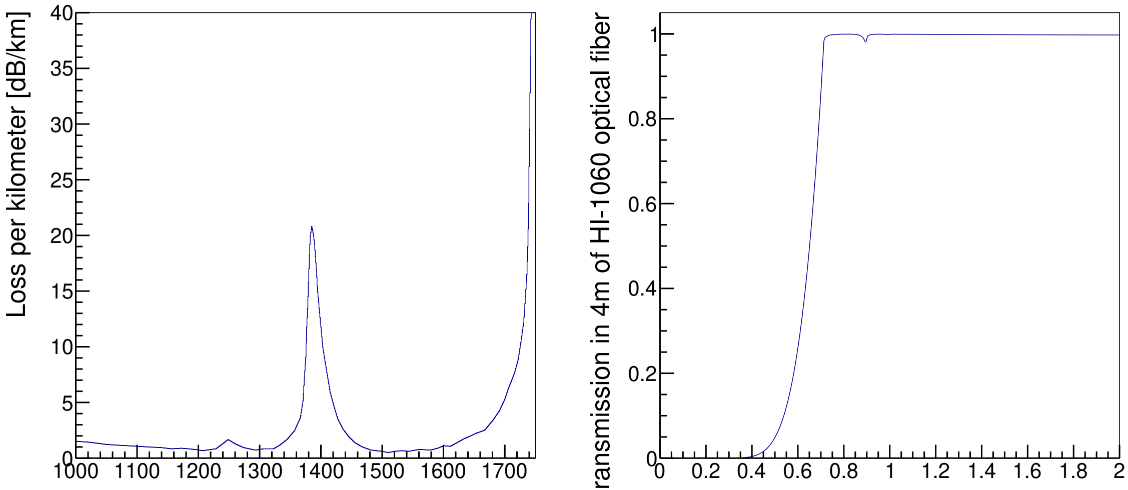

(a) (b)

Figure 4.3: (a) Loss per kilometer of a HI-1060 optical fiber from Corning, the data was taken from [91], (b) Transmission of 4 m of optical fiber as a function of the photon energy computed from the loss per kilometer.

Optical filter

The use of a reflective filter is proposed in [86] as a strategy to reduce the background produced by BBR. This component has been made available in the simulation to study its possible use in the TES system for ALPS II by filtering non-1064 nm photons in the cold inside the cryostat. The filter's transmission $\eta_{\text{filter}}(E)$ can be computed from the data sheet corresponding to the filter or approximated with a Gaussian distribution. Fig. 4.4a shows the simulated distribution using both approaches for the FLH1064-8 filter from Thorlabs. This filter has a central wavelength at 1064 nm and a Full Width Half at Maximum (FWHM) of 8 nm.

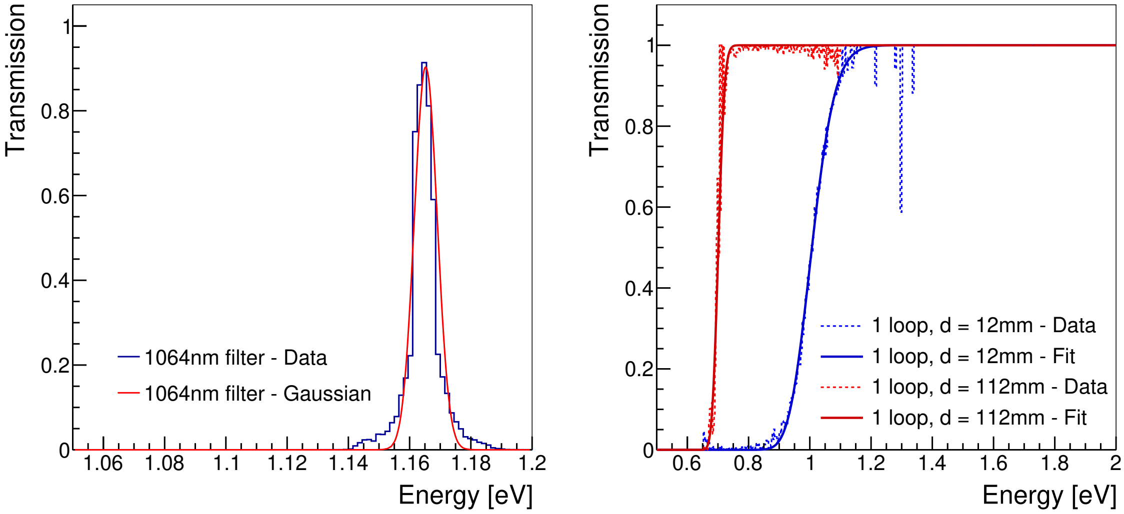

(a) (b)

Figure 4.4: (a) Transmission data as a function of energy from the datasheet of a FLH1064-8 filter from Thorlabs. The peak in the data as a function of wavelength is centered at 1064 nm with a FWHM of 8 nm. The data in the datasheet is in the form of transmission vs. wavelength. The Gaussian function describing the filter is computed with a maximum equal to the maximum transmission in the datasheet, μ = 1064 nm and σ = 8 nm/2.355. The Gaussian function is plotted as a function of energy instead of wavelength. (b) Example of the transmission as a function of energy for 1 loop of fiber curling with diameters d = 1.2 cm and d = 11.2 cm measured in the TES lab with a spectrometer. The data is fitted to an error function for use in the BBR simulation.

Fiber curling

The bending of an optical fiber produces losses depending on the wavelength of the propagating photons and the fiber's bending curvature radius [92]. For a given bending radius, the loss becomes higher for higher wavelengths. Therefore, fiber curling could be used to reject the low-energy part of BBR, if the curling happens in the cold. It is predicted that if this is done in the warm, the BBR escaping the fiber would be replaced by the BBR entering the fiber. The fiber curling in the cold was implemented in [93], where their group tested the reduction of the rate of BBR by changing the curling radius using a superconducting nanowire single-photon detector (SNSPD).

Based on data measured by the TES group and shown in Fig. 4.4b, of fiber loss vs wavelength and bending radius for one loop of bending, a phenomenological function defined by Eq. 4.5 was chosen to fit the data and then implement the curling in the simulation of BBR.

$$\eta_{\mathrm{curl}}(E,\alpha) = \left[\frac{1}{2}\left(1 + \mathrm{erf}\left\{a(\lambda(E) - \lambda_0)\right\}\right)\right]^{\alpha} \tag{4.5}$$

The function can describe the shape of transmission vs. wavelength given by a jump in transmission, as shown in Fig. 4.4b. The variable E is the photon's energy, and α corresponds to the number of loops in the fiber curling, where fractional numbers describe non-complete loops, e.q. half a loop. The parameters a and λ_0 depend on the width and the center of the transition from 0 transmission to 1 for one loop of fiber curling, respectively.

4.2 Combination of simulation and TES response

Considering the optical components and the production of BBR aforementioned, a model can be built to compute the rate arriving at the TES. Eq. 4.6 considers every path j that the BBR photons with energy E could have to follow to reach the detector.

$$N(E,T) = \sum_{j} \iint_{A_j,\Omega_j} \left[B_{np}(E,T) \cdot \prod_{i_j} \eta_{i_j} \cdot H(\theta_{\max} - \theta)\right] \cos\theta \, d\Omega \, dA \tag{4.6}$$

For every path j, the product operator multiplies the transmissions η_{i_j} of every optical component i_j along it. Moreover, a Heaviside step function $H(\theta_{\max} - \theta)$ introduces the approximation that the optical fiber used to transmit the BBR to the TES accepts every photon entering with an angle θ lower than $\theta_{\max}$ with respect to the central axis of the core of the optical fiber, and rejects the rest. Furthermore, it assumes that the transmission of the optical components does not depend on θ.

The advantage of the approach in Eq. 4.6 is its flexibility, which allows the inclusion of different optical components depending on the experimental conditions.

The following explains an example of the assembly of a specific simulation to recreate the conditions of an extrinsic background measurement. Fig. 4.5 shows a scheme of the different components in the simulation.

It starts with the optical fiber with a numerical aperture NA = 0.14 and a core radius $r_{\mathrm{fiber}} = 3.1$ μm given by the manufacturer. The numerical aperture is related to $\theta_{\max}$ as $NA = n_{\mathrm{air}} \sin\theta_{\max} \approx \sin\theta_{\max}$, where n_{air} is the index of refraction of the medium containing the optical fiber, in this case, the air. The integrals in Eq. 4.6 can already be computed (Eq. 4.7) as the BBR term and the transmissions do not depend on the angle θ or the area A_{core} of the fiber's core, which is considered a circle:

$$A_{\mathrm{core}}\Omega_{\mathrm{eff}} = \int_0^{2\pi} d\phi \int_0^{\theta_{\max}} \sin\theta\cos\theta \, d\theta \int_A dA = \pi^2 (NA)^2 r_{\mathrm{core}}^2 \tag{4.7}$$

Afterwards, the photons travel through the optical fiber (A) in the warm. There, the transmission of 6 m of fiber is considered $\eta_{\mathrm{fiber1}}(E, 6\text{ m})$. Here, another source of BBR is taken into account, which is produced in the fiber itself. It produces non-perfect BBR, given that it is not a perfect absorber of light. According to Eq. 4.3 and assuming no reflectivity in the fiber, it will be the same rate as the one entering the fiber but multiplied by the factor

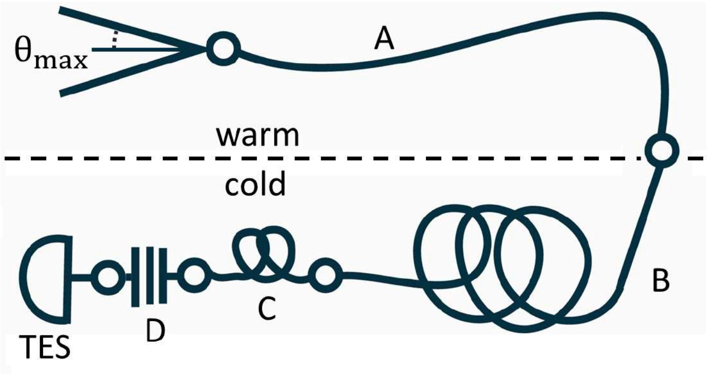

Figure 4.5: Scheme of the simulated path in the BBR. The BBR enters the optical fiber in the circle on the left of (A) if the incidence angle θ with respect to the fiber core axis is lower than $\theta_{\max}$ given by the numerical aperture of the fiber. (A) represents the optical fiber outside the cryostat. The BBR absorbed by the fiber is emitted back inside the fiber because it is at room temperature. The result is equivalent to directly producing BBR on the right of component (A). The section of the fiber inside the cryostat is represented by (B) and (C). (B) and (C) also represent the fiber curling shown in Fig. 4.6a and 4.6b, respectively. Finally, (D) corresponds to the TES optical stack. In every circle, more BBR could couple to the fiber. However, this contribution is neglected given the lower temperature inside the cryostat.

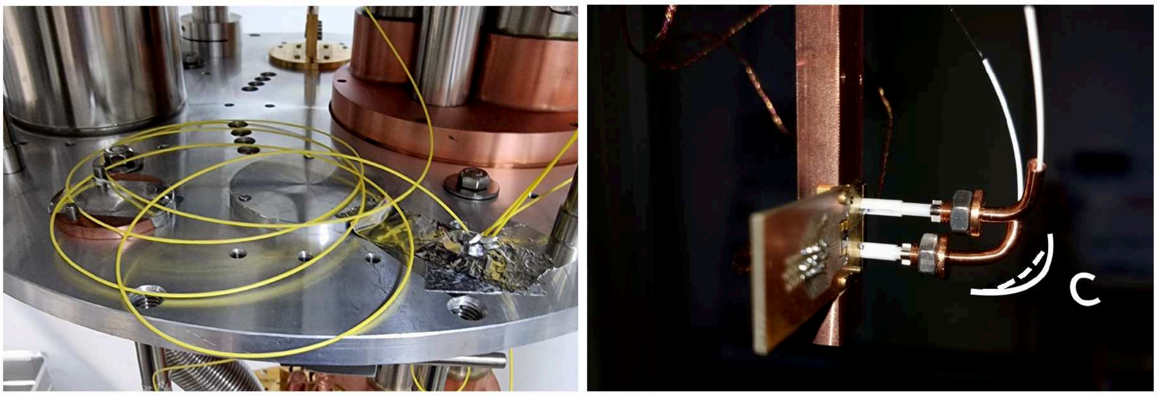

(a)

(b)

Figure 4.6: (a) Fiber curled inside the cryostat approximated as 4 loops of diameter $d = 11.2$ cm, component B in the simulation, with transmission η_{curl1}, (b) Bending of the optical fiber produced by the heat sink, represented in the simulation as 1/4 loop of diameter $d = 2.5$ cm, component C in the simulation. Note that, as the white curve shows, the piece is not described as a perfect arc of circumference depicted in the white dashed curve, meaning that the curling diameter d could be lower, introducing one of the uncertainties in Fig. 4.8.

$1-\eta_{\text{fiber1}}(E, 6\text{ m})$. The sum of the paths' transmissions equals 1, meaning that, as this part of the optical fiber is in the warm, the equilibrium condition mentioned in the previous section should be met: the absorbed photons in the optical fiber will be replaced by the produced photons.

Once the fiber enters the cryostat, its transmission is considered again $\eta_{\text{fiber2}}(E, 4\text{ m})$, with a length estimated at 4 m. Also, inside the cryostat, the fiber is curled, as shown in Fig. 4.6a, with 4 loops of 10 cm diameter, approximated to 11.2 cm since the corresponding data was not available. This is equivalent to the component B shown in Fig. 4.5, with transmission $\eta_{\mathrm{curl1}}(\mathrm{E}, 4)$. Another curling is included to account for the bending of the fiber in its heat sink (Fig. 4.6b) just before connecting it to the TES. Its shape is estimated to produce a quarter of a loop of diameter 2.5 cm, with transmission $\eta_{\mathrm{curl2}}(\mathrm{E}, 1/4)$. Afterwards, the absorbance of the TES is added as the last optical component. Then, the rate of BBR $\mathrm{N(E, T)}$ as a function of temperature and energy arriving at the TES is given by:

$$\mathrm{N(E,T)} = \pi^2(\mathrm{NA})^2 \mathrm{r}_{\mathrm{core}}^2 \cdot \mathrm{B(E,T)} \cdot \eta_{\mathrm{fiber2}} \cdot \eta_{\mathrm{curl1}} \cdot \eta_{\mathrm{curl2}} \cdot \eta_{\mathrm{TES}} \tag{4.8}$$

In Fig. 4.7, the effects of the individual optical components on the BBR spectrum computed with Eq. 4.8 are shown. The transmission of the optical fiber already cuts energies lower than 0.2 eV (Fig. 4.7b). The fiber curling reduces the rate of BBR at energies lower than 0.7 eV significantly (Fig. 4.7c and 4.7d). Finally, the influence of the absorbance of the TES optical stack is not noticeable (Fig. 4.7e).

The accuracy of Eq. 4.8 is affected mainly by the fiber curling component η_{curl} and the value of temperature used to compute $\mathrm{B(E, T)}$. Small variations in T or the radius of the curling can produce changes by one order of magnitude in the results of the expected photon rate $\mathrm{N(E, T)}$. This can be later seen in Fig. 4.8 and 4.9, where the upper values in the uncertainty bands are produced by a variation in the room's temperature by 2 K. The largest variation, represented in the lower values, originates by adding a half-loop of 4.2 cm diameter and assuming a quarter-loop of 1.2 cm diameter instead of 2.5 cm in η_{curl2} (extra step represented in Fig. 4.7f). The 4.2 cm half-loop could result from a non-accounted bending in another region of the cryostat since the fiber is not installed in a straight line inside the cryostat but rather needs to curve around the inner components. The sharper quarter-loop of 1.2 cm diameter instead of 2.5 cm in η_{curl2} is motivated by the imperfection of the arc of the circle shown in Fig. 4.6b.

Eq. 4.8 would be the spectrum of BBR in the TES if it had perfect energy and time resolution. As this is far from reality, the TES response to a photon flux needs to be considered. To account for this, two approaches have been implemented, one of them consisting of the folding of $\mathrm{N(E, T)}$ with a proposed TES response, and the other on the simulation of the pulses produced by the BBR photons in a timeline. Both will be explained in the following.

Folding with TES energy and time resolution

The spectra measured by the TES, from a single energy source, can be approximated to follow a Gaussian distribution ($g(\epsilon, \mu = \mathrm{E}, \sigma = \sigma(\mathrm{E}))$) with μ centered at that energy and σ given by the energy resolution σ/μ, as shown in chapter 5 and 6 for 1064 nm photons. In the analysis described in chapter 5, the relative energy resolution for 1064 nm photons is 11.3 %. Either the relative energy resolution $\mathrm{ER}_{1064\mathrm{nm}}$, or the absolute $\sigma_{1064\mathrm{nm}}$, can be assumed to be constant for other energies such that $\sigma(\mathrm{E}) = \mathrm{ER}_{1064\mathrm{nm}} \cdot \mathrm{E}$ or $\sigma(\mathrm{E}) = \sigma_{1064\mathrm{nm}}$, respectively. The assumption that $\sigma(\mathrm{E}) = \sigma_{1064\mathrm{nm}}$ is motivated by the response of the TES shown in section 6.2. The folding of the rate $\mathrm{N(E, T)}$ and the energy resolution is done using Eq. 4.9. This gives the rate of single photons measured at the TES:

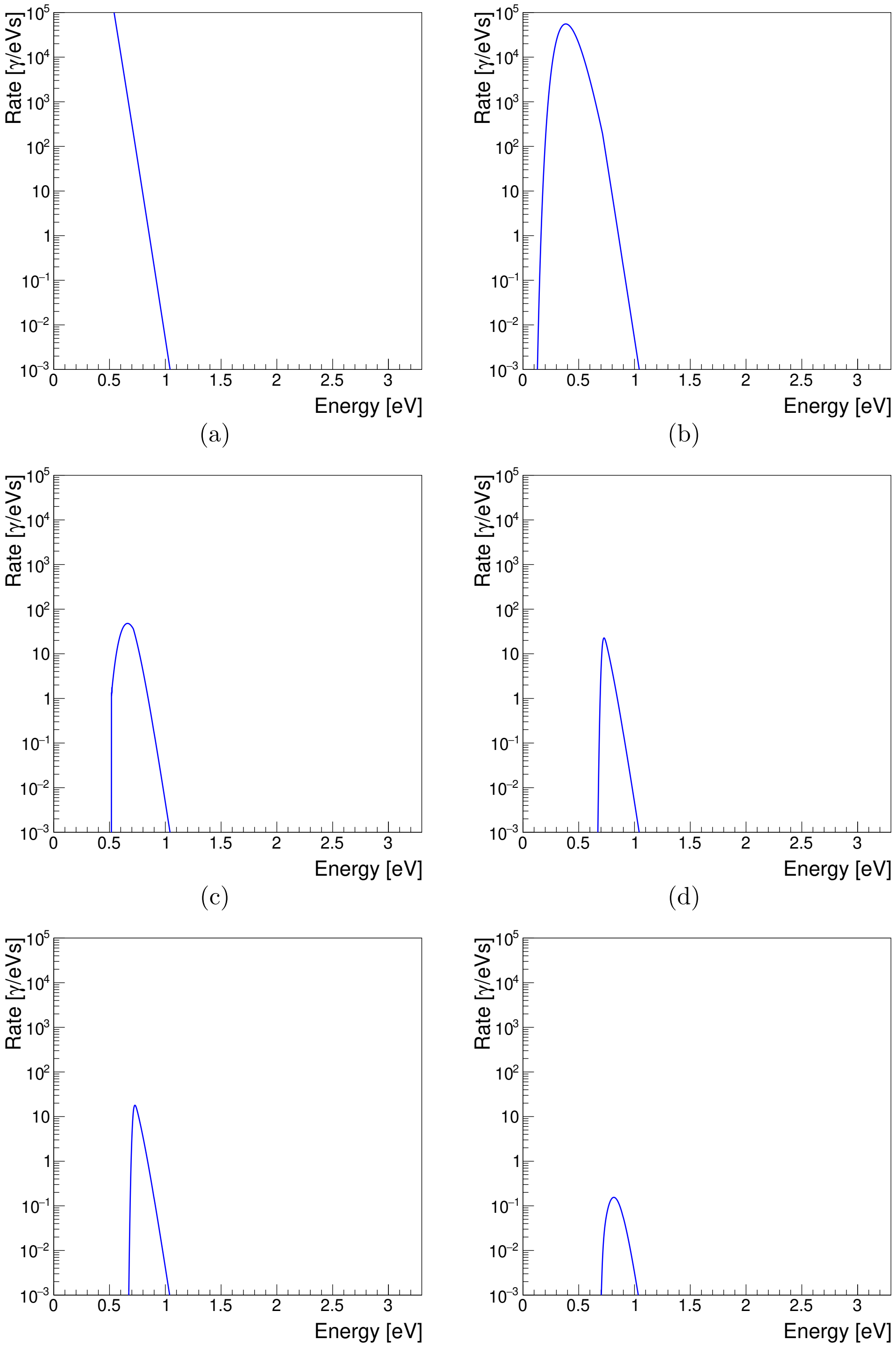

(a) (b) (c) (d) (e) (f)

Figure 4.7: BBR spectrum computed from Eq. 4.8 including optical components step by step: (a) no components, (b) optical fiber transmission η_{fiber}, (c) adding curling with 4 loops with diameter d = 11.2 cm η_{curl1}, (d) adding curling with 1/4 loops with diameter d = 2.5 cm η_{curl2}, (e) adding the absorbance of the TES optical stack, (f) extra curling considered for the lower limit in Fig. 4.8.

$$\hat{N}_{direct}(\epsilon, T) = \frac{\int_0^\infty N(E,T) g(\epsilon, \mu = E, \sigma = \sigma(E))\, dE}{\int_0^\infty g(\epsilon, \mu = E, \sigma = \sigma(E))\, dE} \tag{4.9}$$

The process is equivalent to a convolution of the BBR spectrum with the distortion created by the energy resolution of the TES. The denominator in Eq. 4.9 is added to keep the total BBR rate invariant.

Due to the limited time resolution of the TES, another effect that needs to be considered is the arrival of two photons with a time difference Δt, where the TES voltage has not yet returned to the baseline. This effect is defined as pile-up. If Δt is sufficiently small, the pulses produced by the photons cannot be distinguished and could mimic a single photon, an effect that is often used for measuring photon number distribution with TESs [90]. A value of $\Delta t_{min} = 0.75$ μs is assumed to be the minimum that the current data analysis can distinguish. A strategy for reducing Δt_{min} will be discussed in section 6.4. The possible BBR spectrum from the pile-up contribution, motivated by [94], is computed using Eq. 4.10, where the upper limit in the integral avoids $\epsilon - E$ to be negative:

$$N_p(\epsilon, T) = 2\Delta t_{min} \int_0^\epsilon N(E,T) N(\epsilon - E, T)\, dE \tag{4.10}$$

This is then folded with the energy resolution:

$$\hat{N}_{indirect}(\epsilon, T) = \frac{\int_0^\infty N_p(E,T) g(\epsilon, \mu = E, \sigma = \sigma(E))\, dE}{\int_0^\infty g(\epsilon, \mu = E, \sigma = \sigma(E))\, dE} \tag{4.11}$$

The total rate produced by the BBR is given by adding the single photons and the pile-up contributions:

$$\hat{N}_{total}(E, T) = \hat{N}_{direct}(E, T) + \hat{N}_{indirect}(E, T) \tag{4.12}$$

The results for the conditions defined in this section are shown in Fig. 4.8. The contribution of the pile-up photons does not appear as it is highly suppressed by the fiber curling and the time resolution of the data analysis.

Combination with signal simulation

The spectrum in Eq. 4.8, before the folding with energy and time resolution, can be used to produce pulses in a signal simulation, which will be described in chapter 5 and expanded in section 6.5. Instead of producing pulses with the same amplitude A, it is varied according to $A = A_{1064nm} E / E_{1064nm}$ with E being random energy generated with a probability given by the spectrum. The rise time τ_+ and the decay time τ_- are kept constant. The simulated photons are placed at the position of the trigger in the timeline, mimicking the data. Additional photons are introduced in the timeline by generating the number of photons in a sample using a Poisson distribution and the total rate of BBR photons. As the rate is usually very low (∼ 1 Hz) compared to the size of a timeline (200 μs), the most likely event will be zero photons in a sample.

After the simulation is generated, it can be analyzed in the same way as the measured data. The resulting BBR spectrum for 10000 simulated pulses is shown in Fig. 4.9.

This method allows the consideration of the effects that cannot be included in the folding approach, such as the rejection of events because of the trigger in the DAQ, pile-up and cuts

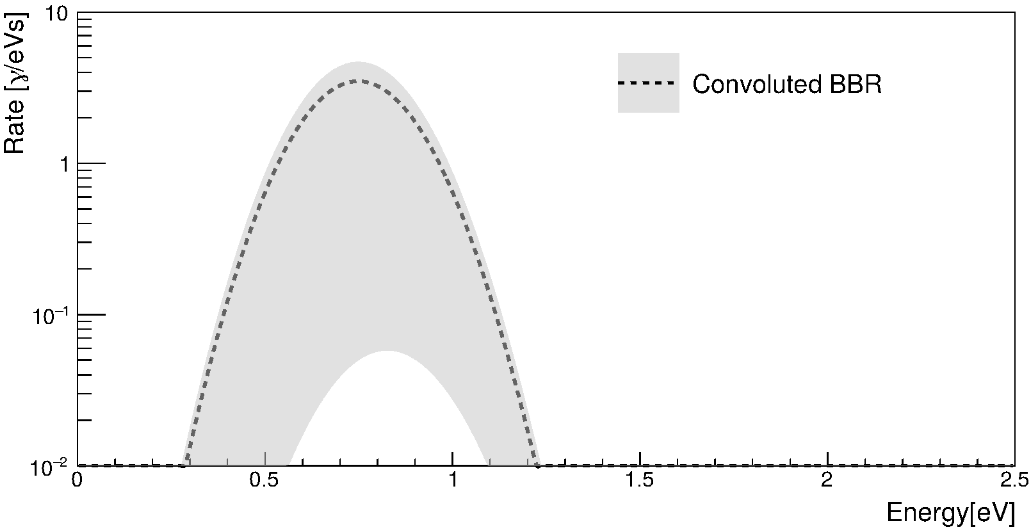

Figure 4.8: The dashed curve represents the BBR spectrum simulated as explained in section 4.2 convoluted with the TES energy resolution. The upper limit of the bands is produced by varying the temperature by 2 K. The lower bound is produced by the assumption of more attenuation due to the non-accounted bending of the fiber inside the cryostat.

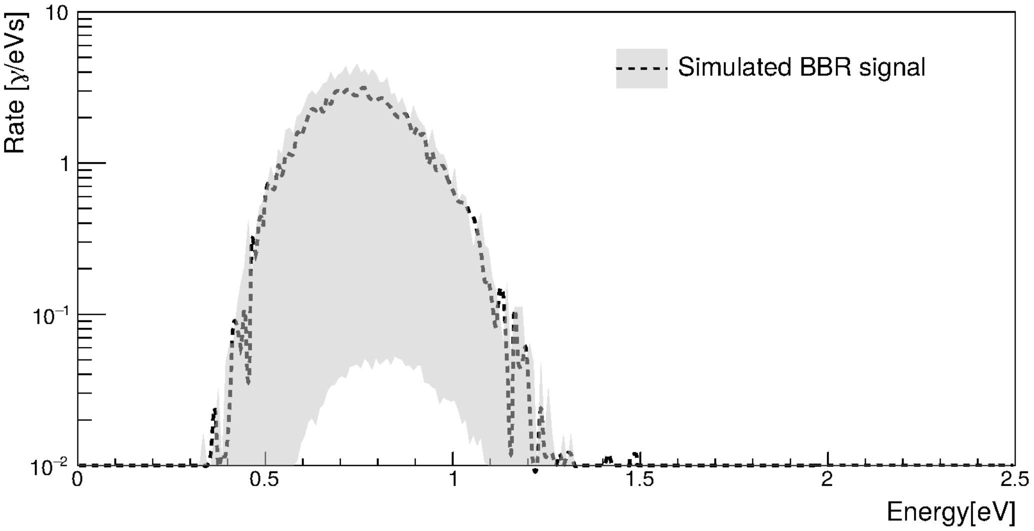

Figure 4.9: The dashed curve represents the rates of BBR obtained by using the simulated spectrum, as explained in section 4.2, as an input to the production of pulses in the signal simulation described in chapter 5 and, afterwards, analyzing the simulated samples with the same fitting analysis procedure used for measurements. The upper limit of the bands is produced by increasing the temperature by 2 K. The lower bound is produced by the assumption of more attenuation due to the non-accounted bending of the fiber inside the cryostat. The limited statistics of events produce the fluctuations in the curve and the bands.

in the fitting parameters from the analysis (described in the next section). Moreover, the energy resolution of the TES is considered naturally in the signal simulation (see chapter 5).

As the BBR spectrum covers several orders of magnitude, many events need to be simulated to accurately compute regions in the spectra with very low rates compared to the maximum. For example, in Fig. 4.9, 10000 events were simulated, and the 1.15 eV energy bin fluctuates by one order of magnitude with respect to the surroundings. The production of simulated samples is limited by the storage required for a high number of events, e.g. 10^5 events, to have enough statistics to reduce the fluctuation in the region with a rate of 10^{-2} γ/eVs, which requires nearly 8 GB of storage.

To compare with data corresponding to several days, the fluctuation in the level of 10^{-4} γ/eVs would need to be reduced, needing about 800 GB of storage. Given the wide range of rates to be simulated, the folding approach will be used in the next section.

4.3 Comparison with extrinsic background measurement

An extrinsic background dataset was measured for 72 hours by covering the warm end of the optical fiber that goes to the cryostat and with the lab in the dark at 295 K. The fiber was curled inside the cryostat and connected to the TES. The conditions were similar to those depicted in the simulation described in the previous section, but the path of the fiber was not completely tracked, so uncontrolled bending could have occurred. A 1064 nm sample was taken before the start of the measurement for reference concerning the energy resolution and energy calibration. The trigger threshold was set at 20 mV for both measurements, and both were analyzed with a fitting analysis. More details about the analysis can be found in the chapter 5. Analogously to work previously performed within the TES group [43], cuts were imposed in the rise and decay times of the pulses and the reduced χ^2 from the fitting procedure. The cut efficiency is defined as the percentage of 1064 nm pulses that survive the cuts. Details can be found in appendix C.

The integral of the photon pulses is considered proportional to the photon's energy. A calibration is done with the integral of the 1064 nm photons $\mathrm{I_{1064nm}}$. Then, the measured energy of the photon is assumed as $\mathrm{E} = \mathrm{E_{1064nm}} \mathrm{I}/\mathrm{I_{1064nm}}$. The events surviving the cuts are accumulated in a histogram. They are scaled, dividing them by the measurement's total time and the energy bin's size. The results are compared with the one predicted by the simulation in Fig. 4.10.

The shape of the simulated spectrum is very similar to the one measured in the extrinsics measurement, but the uncertainties in the simulation limit its ability to describe the background. The low energy edge and the distribution maximum are mainly influenced by the radius and the number of loops in the fiber curling. The curling also affects the right part of the distribution due to the effects of the energy resolution as evidenced in Fig. 4.11 with the reduction of the uncertainty in this region with a better energy resolution. The events at energies higher than 1.4 eV could be caused by surviving events from the intrinsic background explained in chapter 3.

4.4 Evaluation of results

The main interest for ALPS II lies on the reduction of the number of background events in the region surrounding 1064 nm photons, i.e. 1.165 eV. Considering the TES energy resolution and the distribution of 1064 nm photons in the energy spectrum as a Gaussian, regions of

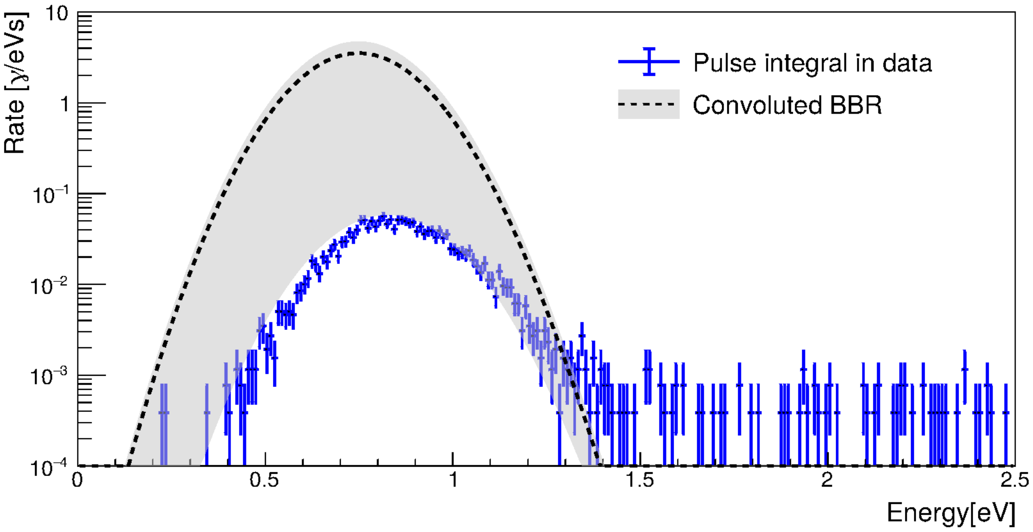

Figure 4.10: Simulated spectrum from Fig. 4.8 compared to the measured rates from data. The pulse integral computed from the analysis was scaled to energy using a 1064 nm sample as a reference.

1σ, 2σ, 3σ are proposed, with $\sigma = 0.13$ eV. The results are shown in Table 4.1, with the corresponding values computed from the simulation.

Range (σ)	Analysis efficiency	Measured rate (I_{Ph})	Simulated lower rate	Simulated rate	Simulated upper rate
$-1, 1$	67.7%	$2.1 \cdot 10^{-3}$cps	$1.5 \cdot 10^{-3}$cps	$2.3 \cdot 10^{-2}$cps	$3.1 \cdot 10^{-2}$cps
$-2, 2$	94.7%	$6.5 \cdot 10^{-3}$cps	$6.2 \cdot 10^{-3}$cps	$1.6 \cdot 10^{-1}$cps	$2.1 \cdot 10^{-1}$cps
$-3, 3$	98.9%	$1.3 \cdot 10^{-2}$cps	$1.3 \cdot 10^{-2}$cps	$5.2 \cdot 10^{-1}$cps	$7.0 \cdot 10^{-1}$cps
$0, 3$	49.5%	$5.8 \cdot 10^{-4}$cps	$2.0 \cdot 10^{-4}$cps	$1.6 \cdot 10^{-3}$cps	$2.2 \cdot 10^{-3}$cps
$-1, 3$	83.3%	$2.3 \cdot 10^{-3}$cps	$1.5 \cdot 10^{-3}$cps	$2.3 \cdot 10^{-2}$cps	$3.1 \cdot 10^{-2}$cps

Table 4.1: Rates computed for measured extrinsics data (I_{Ph}) and simulated BBR (expected), with the upper and lower limits of the uncertainty bands, for several σ regions around 1064 nm photon energy. The analysis efficiency in measured data is defined as the product of the cut efficiency, in this case of 99.2 % (appendix C), and the efficiency resulting from excluding 1064 nm photons outside the σ ranges.

The measured rates are within the limits calculated from the simulation; however, this is mainly due to the simulation uncertainty. To improve the accuracy of the BBR simulations, detailed tracking of the path of the fiber inside the cryostat should be done in future measurements, as the curling has been evidenced as the main contributor (shown as the transition from Fig. 4.7e to Fig. 4.7f), especially for low curling diameters. Furthermore, in the case of a measurement similar to the one analyzed in this chapter, a temperature sensor should be placed in the closed end of the fiber to monitor fluctuations during the measurement.

Given the asymmetry of the BBR spectrum, regions given by $[-\sigma, 3\sigma]$ or $[0, 3\sigma]$ could be a good trade-off to reduce the background while maintaining high efficiency, but the measured rates of r $= 2.3 \cdot 10^{-3}$cps and r $= 5.8 \cdot 10^{-4}$cps are still well above the requirements for ALPS II of r $< 7.7 \cdot 10^{-6}$cps.

To reduce these rates, the use of an optical filter in the cold region of the cryostat has been proposed to block most of the BBR events. However, this system suffers from loss of transmission efficiency due to the shift of the filter's central wavelength and misalignment of the parts of the filter bench as a consequence of thermal contraction during cool-down. As seen before, the filter has been implemented in the simulation framework but was not included in the simulation example in section 4.2. Moreover, the use of more loops in the fiber curling or lower radii could help to reduce the background, but it has a limit, as a low radius of curling can reduce the efficiency for 1064 nm photons. Another solution could be the improvement in energy resolution. As shown in Fig. 4.11, a better energy resolution could significantly reduce the background due to BBR in the region surrounding 1.17 eV (1064 nm photons). With an energy resolution of approximately 5 %, the background rates in the regions given by $[-\sigma, 3\sigma]$ or $[0, 3\sigma]$ are predicted as $3.2 \cdot 10^{-5}$ cps and $3 \cdot 10^{-6}$ cps, respectively, the latter already fulfilling the limit of the ALPS requirements.

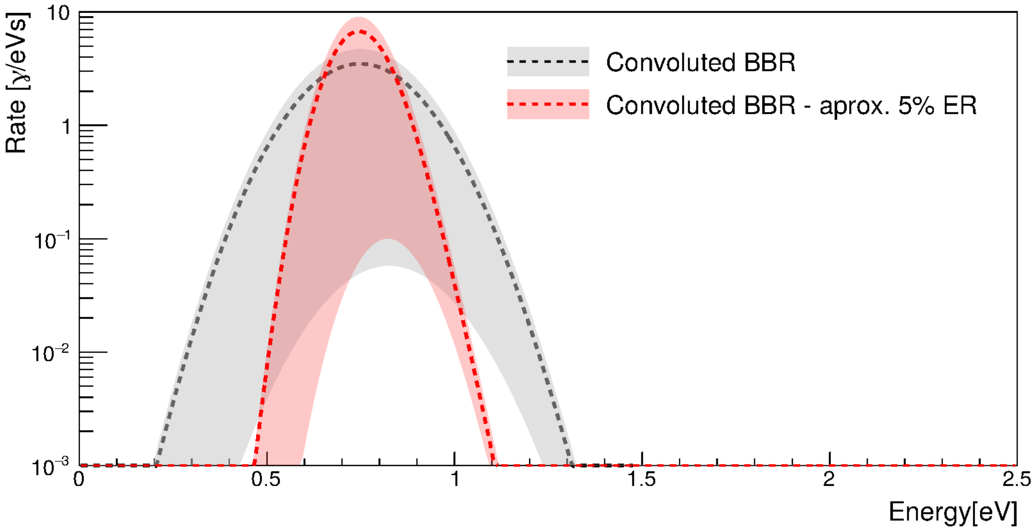

Figure 4.11: Simulated spectrum from Fig. 4.8 compared to the same BBR simulation conditions convoluted with an energy resolution of 5 % instead of 11.3 %.

The following chapters will develop towards the improvement in energy resolution. Chapter 5 focuses on its understanding, and chapter 6 will propose an optimized analysis method to improve it.

CHAPTER

5

UNDERSTANDING OF THE TES ENERGY RESOLUTION

Contents

The energy resolution measured in the TES can be explained by a combination of the variations in the absorption process of a photon and the contribution of the baseline noise. Within the framework of this thesis, the TES signal was simulated to evaluate the contribution of the baseline noise. The first results were published in [95]. This chapter will provide a comprehensive view of this aspect and an optimized method for the baseline noise simulation compared to [95].

5.1 Analysis in time domain

The raw trigger rate for intrinsic background, defined in section 2.3, measured with the same trigger threshold used for 1064 nm photons, at about 75 % of the pulse height, is in the order of 10^{-2}cps [43]. This rate is incompatible with the ALPS II requirements for a single photon detector. To cope with this, a pulse shape analysis was implemented, which allowed to reject pulses with a shape different than the one for 1064 nm photons. The results from a previous thesis reduced the background rate to $6.9^{+2.62}_{-1.47} \cdot 10^{-6}$cps using this technique [11], while keeping more than 90 % efficiency for 1064 nm photons, reaching the ALPS II requirements.

This pulse shape analysis consists of a fitting procedure applied on a trigger window using the function described by equation 5.1:

$$\mathrm{U_{ph}(t)} = -\frac{2\mathrm{A_{ph}}}{\exp\left\{-\frac{1}{\tau_{\mathrm{rise}}}(\mathrm{t}-\mathrm{t_0})\right\} + \exp\left\{\frac{1}{\tau_{\mathrm{decay}}}(\mathrm{t}-\mathrm{t_0})\right\}} + \mathrm{V_0} \tag{5.1}$$

This is an alternative to the expression obtained from Small Signal Theory (SST), which is a piece-wise function and therefore unstable when used for this purpose [96]. The parameters $\mathrm{A_{ph}}$, τ_{rise}, and τ_{decay} define the shape of the pulse and are related to its amplitude, rise time, and decay time, respectively. The parameters $\mathrm{t_0}$ and $\mathrm{V_0}$ correspond to the pulse position in the time window and the voltage offset. In order to facilitate the analysis of a simulated signal, the fitting procedure was implemented in ROOT [54, 97]. An example of fitting a measured photon pulse is shown in Fig. 5.1a.

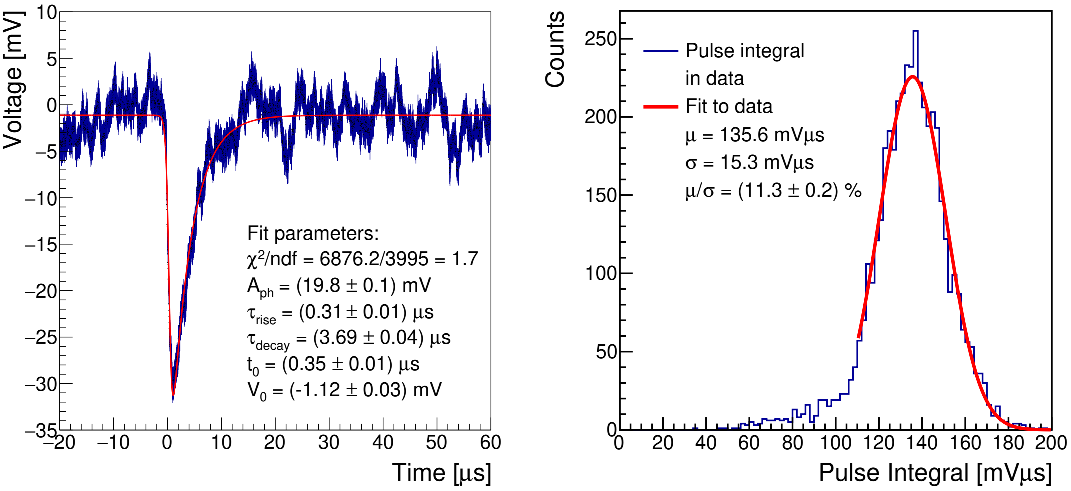

(a) (b)

Figure 5.1: (a) Measured 1064 nm pulse fitted to the phenomenological model and parameters obtained from the fitting procedure. (b) Pulse integral distribution of measured 1064 nm photons and Gaussian function fitted to the distribution. The energy resolution is calculated from the Gaussian function's mean and sigma, resulting in (11.3 ± 0.2)%.

The pulse integral is predicted to be proportional to the energy of the arriving photon, as discussed in section 2.1.2. The pulse integral is calculated by integrating the fitted function without the voltage offset. The energy resolution is then calculated as the ratio between the values σ and μ of a Gaussian function fitted to the distribution of computed time integrals from more than 500 pulses for enough statistics (Fig. 5.1b).

With the TES working point set to a fraction of 0.3 of its normal-conducting resistance, a GBWP in the SQUIDs of 1.5 GHz and a sampling rate of 50 MHz in the Alazar card, the computed energy resolution corresponds to (11.3 ± 0.2)% (Fig. 5.1b). This is equivalent to 0.31 eV of FWHM. This might resolve the ALP signal from 532 nm photons that could travel from the ALPS II optical cavity to the TES. These photons would be the result of the use of green light for cavity control, as mentioned in section 1.3.2. With the energy resolution of 11.3 % at 1.165 eV, the 532 nm signal is predicted to be at 9 σ from the 1064 nm distribution.

5.2 Simulation of TES signal from signal model and baseline noise

In order to simulate the TES signal, the PSD of the noise is extracted from the data and the procedure is described in the following.

Ideally, a continuous noise timeline with the laser off could be taken before the light samples to have a continuous noise sample free from photon pulses. This was not the case for previous measurements; therefore, another procedure was considered to obtain noise samples. As mentioned before, the time window for every triggered photon pulse is chosen as 200 μs. In a light sample, the photon pulse between 20mus and 50mus from the start of the time window is present, and the remaining part is noise as the signal's contribution is negligible (in the order of $\exp\{-10\}$). Thus, the last 120 μs are used to obtain a noise sample. The squared root of the mean value of PSD from several noise samples is calculated to compute the noise distribution in the frequency domain. The uncertainty for every frequency is calculated from the statistical uncertainty of the mean. It is important to check that no pulses are present in the noise window. If so, the noise is overestimated in the low-frequency region of the PSD.

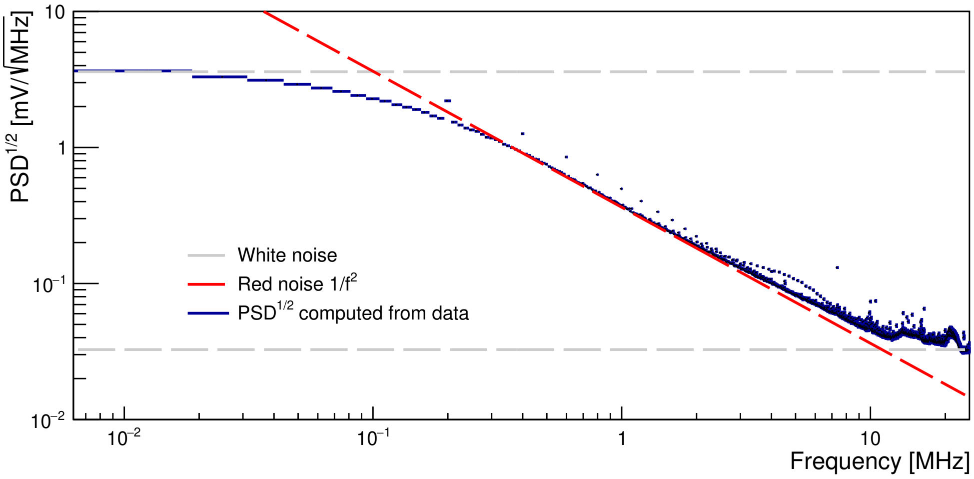

Figure 5.2: PSD of noise in data in blue. Small peaks represent the noise coming from harmonics, specifically 200 kHz harmonics. The white noise dominates at frequencies below 50 kHz and above 10 MHz. The Brownian noise ($1/f^2$) dominates between 100 kHz and 10 MHz.

From the shape of the PSD in Fig. 5.2, it can be seen that a mix of white (section 5.2.2) and Brownian (section 5.2.3) noise dominates the frequencies below 200 kHz, Brownian noise between 200 kHz and 10 MHz, and white noise above 10 MHz. The 200 kHz harmonics (section 5.2.4) are observed on top of that.

The simulation of the noise extracted from the data and the TES pulses is explained in the next sections.

5.2.1 Signal parameters for 1064 nm

The phenomenological model given by Eq. 5.1 is used to simulate ideal 1064 nm pulses. To generate pulses, the parameters A_{ph}, τ_{rise}, τ_{decay}, $t_0 = 0$ and $V_0 = 0$ are fixed recreating the conditions where every 1064 nm photon produces the same response in the TES and there is no electronic noise (Fig. 5.4a). The parameters A_{ph}, τ_{rise}, τ_{decay} are chosen as the values with the highest probability in the corresponding distributions in Fig. 5.3 obtained from the fitting procedure done in data.

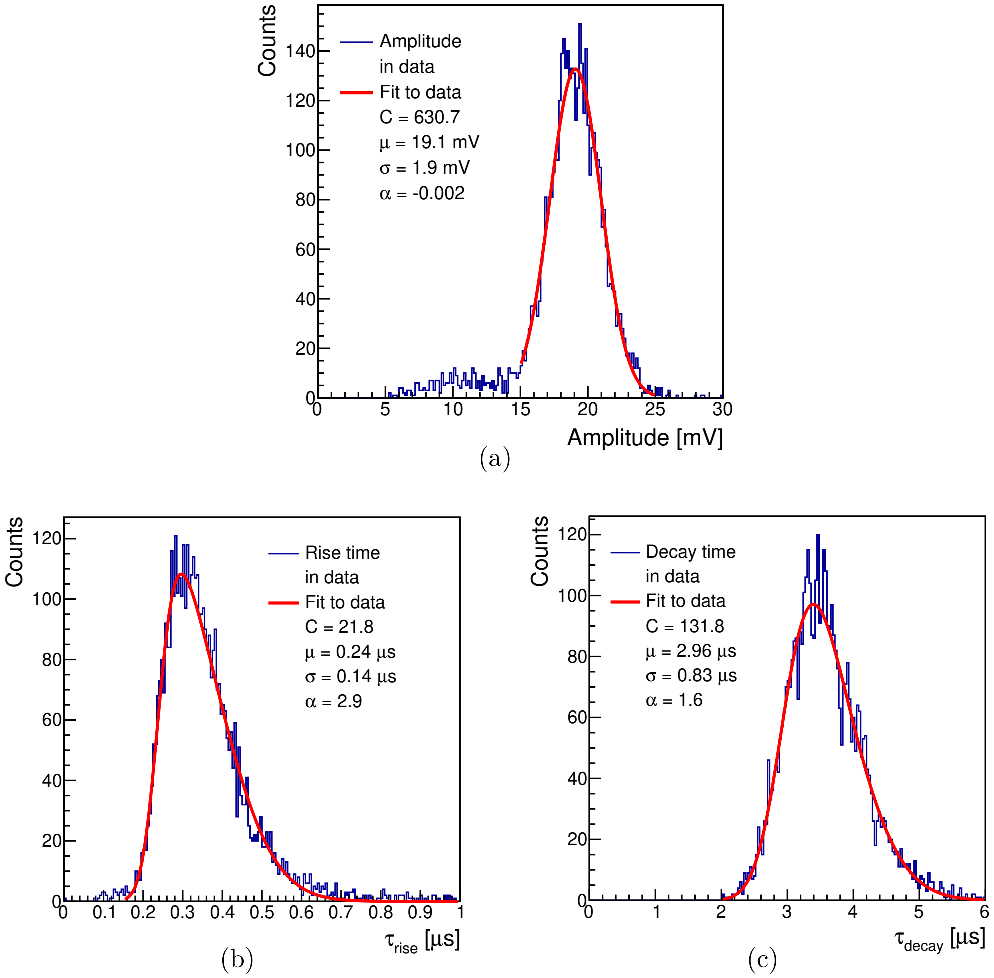

(a)

(b)

(c)

Figure 5.3: Distribution of parameters obtained by fitting the phenomenological model to measured 1064 nm pulses: (a) Amplitude, (b) Rise time, and (c) Decay time. A skew normal distribution function is fitted to the distributions. The skew normal distribution function $f(x, C, \mu, \sigma, \alpha) = 2C \cdot g(x, \mu, \sigma) \cdot \mathrm{erf}(\alpha \cdot x, \mu, \sigma)$ represents the product between a Gaussian function $g(x, \mu, \sigma)$ and an error function $\mathrm{erf}(\alpha \cdot x, \mu, \sigma)$.

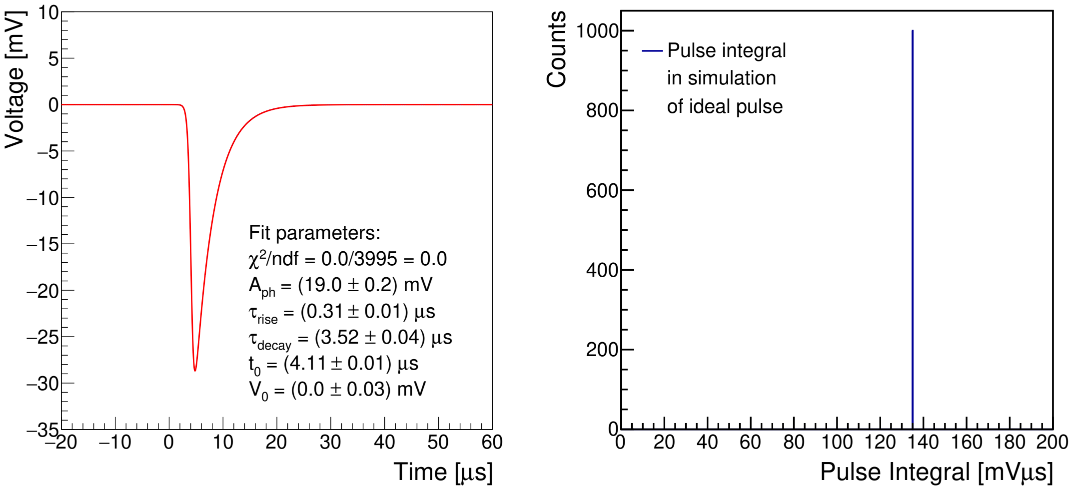

(a) (b)

Figure 5.4: (a) Simulated ideal 1064 nm pulse fitted to the phenomenological model and corresponding fit parameters (testing of fitting analysis on the simulated signal before adding the baseline noise in section 5.3). For technical reasons, an uncertainty of 1.5 mV (same treatment as in data) is considered for the fit. (b) Pulse integral distribution of ideal 1064 nm. The integral of every simulated pulse occupies a single bin at $\mu = 135.2 \mathrm{mV\mu s}$.

As expected, when the analysis described in section 5.1 is applied over these pulses, the computed time integral always returns the same value, and we observe perfect energy resolution (Fig. 5.4b).

5.2.2 White noise production

White noise consists of a random signal with a constant PSD k and amplitude for every frequency. It can be simulated by generating every sample as a random number following a Gaussian distribution function, with $\mu = 0$ and $\sigma = \sqrt{k/\Delta t}$, where Δt is the sampling period. In that case, the produced noise is considered white Gaussian noise (WGN).

5.2.3 Red or Brownian noise

Red noise or Brownian noise is also a random signal, but the power spectral density decreases with frequency, following a $1/f^2$ distribution. One of the simplest algorithms to simulate it is the cumulative sum of WGN. As the PSD of the TES data is not fully red noise, the amplitude of the simulated noise for low frequencies needs to be modulated. Otherwise, it goes to infinity for $f = 0$ (Fig. 5.5b), producing huge fluctuations as in Fig. 5.5a.

A modulation is introduced by making the probability of high absolute values tend to zero. Instead of generating a random value following a Gaussian distribution, its absolute value is generated. Then, the decision to add or subtract it from the cumulative sum depends on whether a uniformly distributed random value between -a and a is greater or lower than the cumulative sum, respectively. Therefore, when the cumulative sum is close to a, it is very unlikely that the next generated value will be added. Similarly, this happens when the cumulative sum is close to -a, but with subtraction.

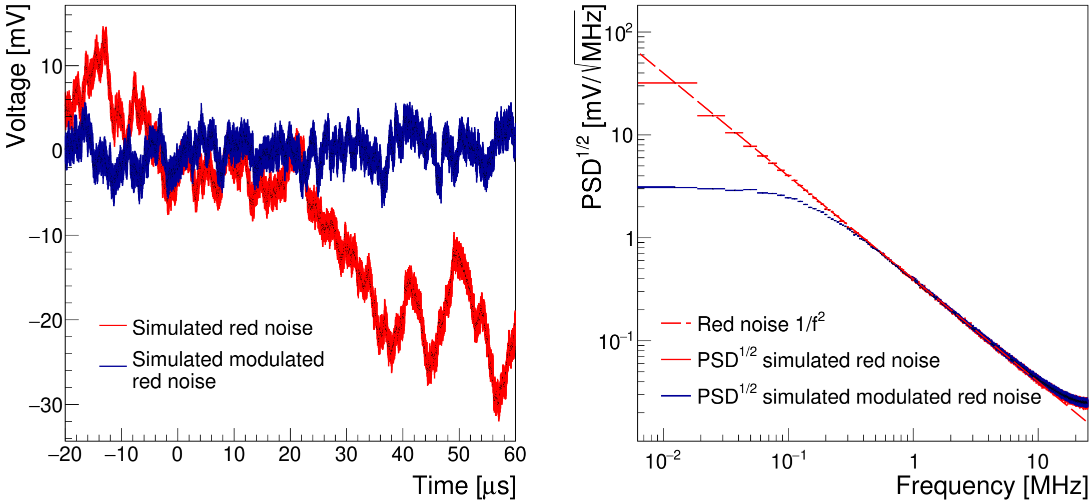

(a) (b)

Figure 5.5: (a) Comparison of the behaviours of pure and modulated red noises. The pure red noise presents large low-frequency fluctuations. (b) Comparison of the PSDs of unmodulated and modulated red noises. The value of the PSD of the pure red noise tends to infinity as the frequency approaches zero.

Although the data's PSD can be reproduced with this modulation, it presents several limitations. Big fluctuations are unlikely in data but could appear in long periods. Due to the way the noise is being produced, it is limited to the range [-a, a], making big fluctuations impossible to happen in simulations. Furthermore, the parameters that describe this noise need to be fitted to the PSD of the data by trial and error, which makes the fine-tuning of the simulation very difficult.

This method was used to obtain the results in [95], but a better algorithm that solves these limitations was implemented later and will be described in section 5.2.5.

5.2.4 200 kHz harmonics

The 200 kHz harmonics appear in the TES module used to collect the data analyzed in this chapter. This noise is coherent in time. Therefore, it can be simulated by calculating the sum of a family of sinusoidal functions $\mathrm{A_k} \sin(2\pi \mathrm{k f_0 t} + \phi_\mathrm{k})$, with t as the time since the start of the simulation, $\mathrm{f_0}$ the main frequency of the harmonics, k the order of the harmonic, and $\mathrm{A_k}$ and ϕ_k the amplitude and phase of the k-order. The calculation of the sinusoidal function is computationally expensive in most programming languages, and usually, the simulated time is much longer than one period of the main frequency $\mathrm{f_0}$. Therefore, the production of the 200 kHz harmonics can be optimized by computing and storing one period and then using the stored values to produce the next samples.

The value of $\mathrm{A_k}$ can be extracted from the PSD of the data. The class `TSpectrum`, already implemented in ROOT, can extract the height of the peaks $\mathrm{PSD_{total}(f)}$ present in the PSD and the distribution of the non-periodic noise $\mathrm{PSD_{nonper}(f)}$. The value of $\mathrm{A_k}$ is equivalent to $2\sqrt{\mathrm{PSD_{per}(f)/N\Delta t}}$ for every frequency of the harmonics and can be calculated using Eq. 5.2, where N is the number of samples used to calculate the PSD, and Δt is the sampling period.

$$\mathrm{PSD_{per}(f) = PSD_{total}(f) - PSD_{nonper}(f)} \tag{5.2}$$

A verification of this assumption can be found in the appendix A.3.

The origin of this noise is attributed to the SQUID electronics. The method to simulate this kind of noise can also be used with other frequencies.

5.2.5 Colored noise production

The use of digital filters is a good alternative to the production of red noise explained in section 5.2.3. Moreover, it opens the possibility to generalize the simulation to $1/\mathrm{f}^{2\mathrm{n}}$ and $\mathrm{f}^{2\mathrm{m}}$ noise.

A low-pass digital filter

In an order-1 low-pass filter (LPF) with cut frequency $\mathrm{f_c}$, sampling period $\Delta \mathrm{t}$ and described by Eq. 5.3, the value of a sample at a certain point in time $\mathrm{V_i^{(1)}}$ depends on the previous filtered sample $\mathrm{V_{i-1}^{(1)}}$ and the value of the current sample $\mathrm{V_i^{(0)}}$.

$$\mathrm{V_i^{(1)} = \beta_L V_i^{(0)} + (1-\beta_L) V_{i-1}^{(1)}}, \qquad \mathrm{\beta_L = \frac{2\pi f_c \Delta t}{1 + 2\pi f_c \Delta t}} \tag{5.3}$$

This corresponds to a Linear Time-Invariant (LTI) digital filter, and its response to a signal is well understood [98]. The response of the digital filter in Eq. 5.3 is equivalent to the expression in Eq. 5.4. The derivation of this term can be found in the appendix A.4.

$$\mathrm{|H_L(f)|^2 = \frac{\beta_L^2}{1 + 2\,(\beta_L - 1)\cos(2\pi f \Delta t) + (\beta_L - 1)^2}} \tag{5.4}$$

This response converges to 1 for frequencies below $\mathrm{f_c}$, and to $1/\mathrm{f}^2$ for frequencies above $\mathrm{f_c}$ and much lower than $1/\Delta \mathrm{t}$, as shown in Fig. 5.6a.

Concatenating this filter *n* times produces an n-order low-pass filter.

$$\mathrm{V_i^{(j)} = \beta_L V_i^{(j-1)} + (1-\beta_L) V_{i-1}^{(j)}}, \qquad \mathrm{\beta_L = \frac{2\pi f_c \Delta t}{1 + 2\pi f_c \Delta t}} \tag{5.5}$$

In Eq. 5.5, a loop in *j* filters the signal several times until j = n. Therefore, the values $\mathrm{V_i^{(n)}}$ and $\mathrm{V_i^{(0)}}$ represent the filtered and the unfiltered signal respectively. By utilizing this algorithm, the response of this filter is given by Eq. 5.6, which is conveniently the power of *n* of Eq. 5.4, which corresponds to the curve $1/\mathrm{f}^{2\mathrm{n}}$ for frequencies above $\mathrm{f_c}$, as shown in Fig. 5.6a.

$$\mathrm{|H_L(f)|^2 = \left(\frac{\beta_L^2}{1 + 2\,(\beta_L - 1)\cos(2\pi f \Delta t) + (\beta_L - 1)^2}\right)^n} \tag{5.6}$$

A high-pass digital filter

Analogously, an *m*-order high-pass filter (HPF) can be produced using the algorithm in the Eq. 5.7, with cut frequency $\mathrm{f_c}$ and sampling period $\Delta \mathrm{t}$.

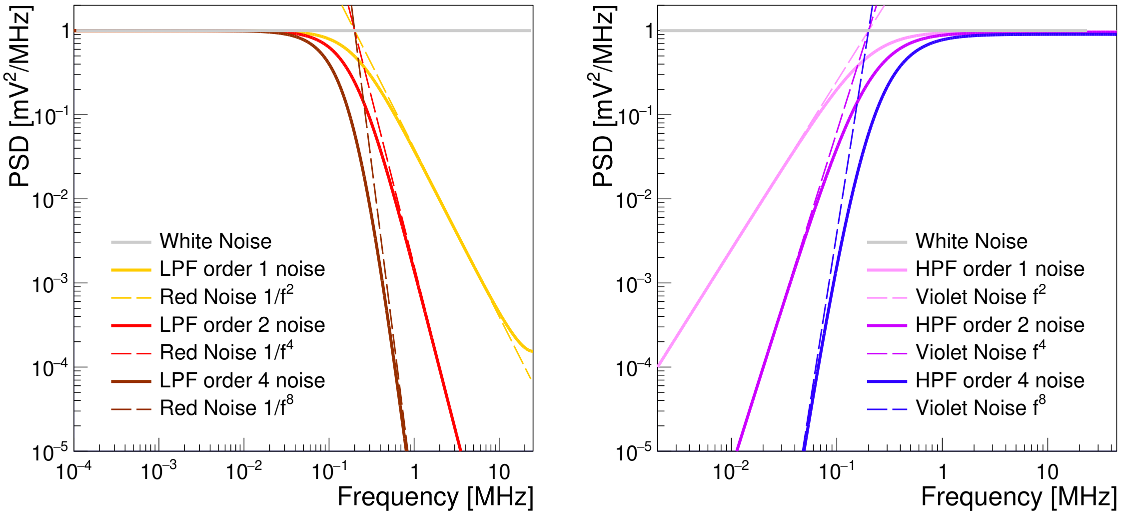

(a) (b)

Figure 5.6: Comparison between the response of the filters and the noise. The dashed lines intercept at the cut frequency of the filters, set at 200 kHz. (a) *n*-order low-pass filters (LPF) against $1/f^{2n}$ noise, (b) *m*-order high-pass filters (HPF) against f^{2m} noise.

$$V_i^{(j)} = \beta_H V_{i-1}^{(j)} + \beta_H \left(V_i^{(j-1)} - V_{i-1}^{(j-1)} \right), \qquad \beta_H = \frac{1}{1 + 2\pi f_c \Delta t} \tag{5.7}$$

A loop in *j* filters the signal several times until $j = m$. As in the low-pass filter case, the values of $V_i^{(n)}$ and $V_i^{(0)}$ represent the filtered and the unfiltered signal respectively. The response of this filter is computed using Eq. 5.8.

$$|H_H(f)|^2 = \left(\frac{2\beta_H^2 \left(1 - \cos\left(2\pi f \Delta t\right)\right)}{\left(1 + \beta_H^2\right) - 2\beta_H \cos\left(2\pi f \Delta t\right)} \right)^m \tag{5.8}$$

For frequencies below f_c, this response is equivalent to f^{2m}, as evidenced in Fig. 5.6b.

Colored noise

The combination of WGN and the digital filters previously mentioned produces $1/f^{2n}$ noise and f^{2m} noise. The unfiltered data in Eq. 5.5 and 5.7 are the current random value ($V_i^{(0)}$) and the previous random value ($V_{i-1}^{(0)}$), generated using a Gaussian distribution function as in section 5.2.2. The spectrum of the produced noise is determined by Eq. 5.6 and Eq. 5.8 respectively, scaled by the parameter σ used to generate the WGN. The special cases of noise with a spectrum corresponding to $1/f^2$ and f^2 are usually referred to as red noise and violet noise, respectively.

5.2.6 Combined noise production

Fig. 5.7 shows the corresponding simulated noise component's response function and the PSD. The response function describes its corresponding noise spectrum very well.

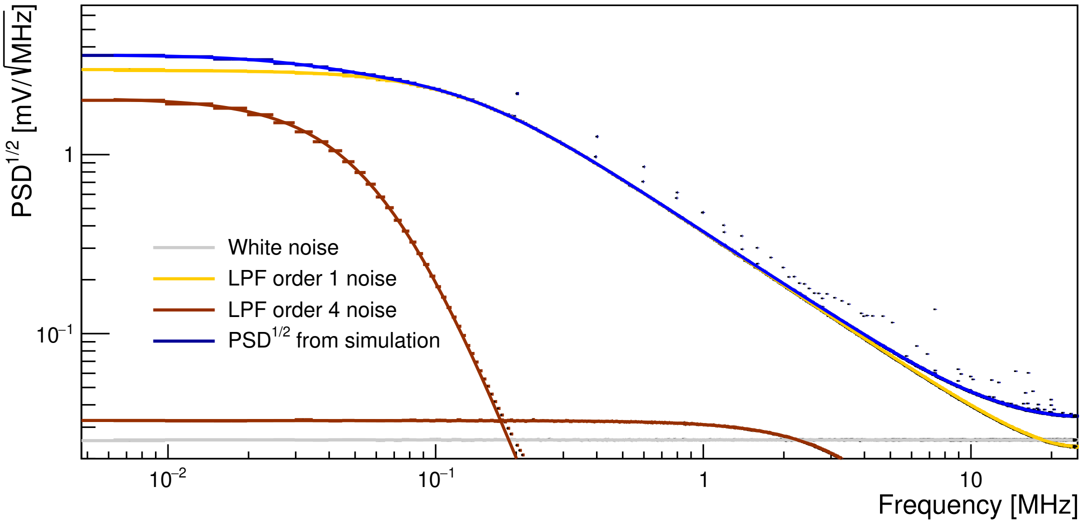

Figure 5.7: PSD of simulated noise and its components. In this case, the noise is composed of the superposition of the 200 kHz harmonics, white noise with $\sigma = 0.180$ mV, one first-order low-pass filter (LPF) noise with parameters $\sigma = 20.9$ mV and $f_c = 127$ kHz, and two fourth-order low-pass filter noises with parameters $\sigma = 14.6$ mV and $f_c = 66.6$ kHz and $\sigma = 0.231$ mV and $f_c = 9.01$ MHz. The parameters are obtained from a fit to the PSD of the data. Other combinations of components are also computed, and the one with the lowest χ_{red} is selected.

With known responses of simulated white noise (section 5.2.2), 200 kHz noise (section 5.2.4), and colored noise (section 5.2.5), the PSD from data can be fitted to the parameters of the different noise components. The fitting function consists of the sum of the response of white noise (a constant), red noise components (Eq. 5.6) with different values of cut frequencies f_c and orders n, and violet noise components (Eq. 5.8). The harmonics are extracted from the noise spectrum from data, as described in section 5.2.4, and the fitting function is fitted to the resultant spectrum.

For example, typical TES noise at 1.5 GHz of GBWP and $0.3R_N$ TES working point can be fitted by combining the responses of one low-pass filter of order 1, two low-pass filters of order 4 and white noise. This allows to reproduce the noise spectrum of the data in simulations very precisely, as evidenced in Fig. 5.8.

5.3 Baseline noise as explanation for energy resolution

The simulation of TES pulses is performed with the superposition of the simulated noise from section 5.2.6 and the ideal pulses from section 5.2.1. Small corrections are applied to the selected parameters of the ideal pulses so that the maximum of the simulated distributions matches the data. This correction is necessary because the pulses in the data respond to the SST and not to the phenomenological model, as will be explained in section 6.5. The simulation is produced sample by sample until a full-time window is constructed. The value of a sample is the sum of the noise produced in that sample and Eq. 5.1 evaluated in the time corresponding to that sample. Fig. 5.9a shows an example of a simulated TES pulse.

The analysis described in section 5.1 is applied over the simulated and the measured pulses.

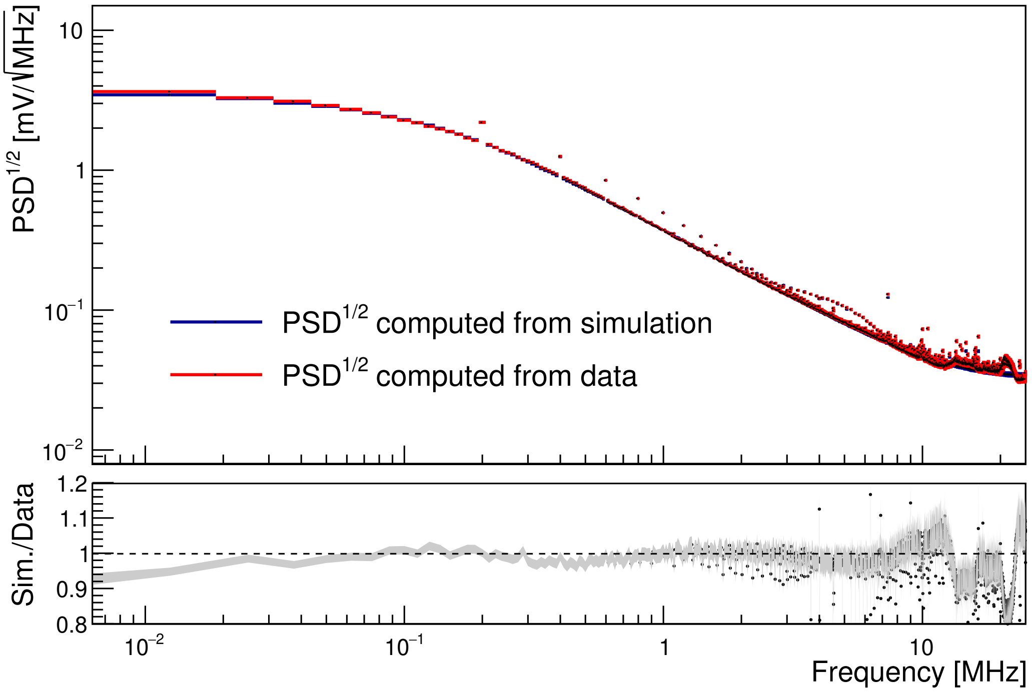

Figure 5.8: Comparison of the PSD of simulated and measured noises. The lower plot shows the ratio between the PSDs with the PSD of the measured noise in the denominator with its corresponding uncertainty. The points correspond to the deviations present in the amplitude of the harmonics with respect to the data.

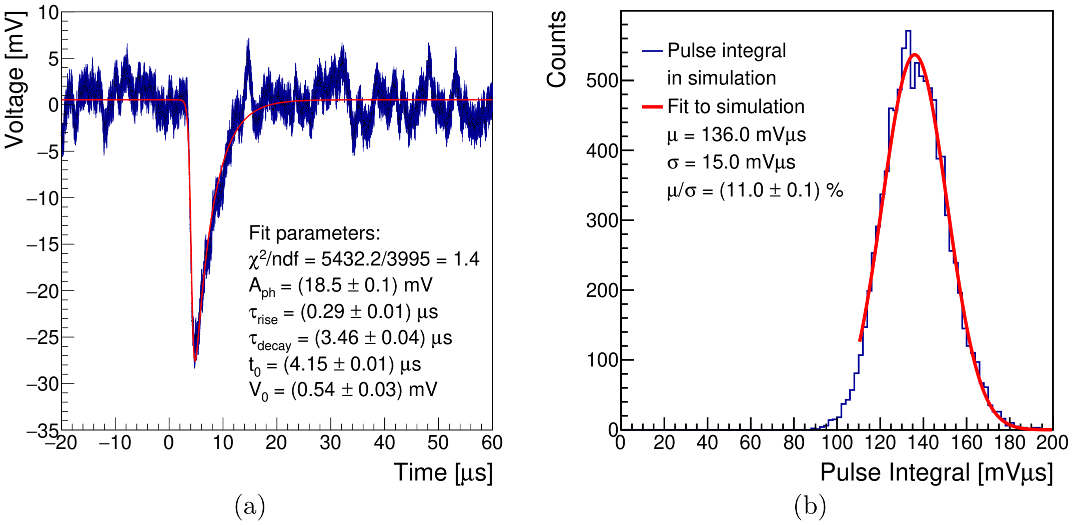

Figure 5.9: (a) Simulated 1064 nm pulse fitted to the phenomenological model and parameters obtained from the fitting procedure, (b) pulse integral distribution of simulated 1064 nm photons and Gaussian function fitted to the distribution. The energy resolution is calculated from the Gaussian function's mean and sigma, resulting in (11.0 ± 0.1)%.

The results of the fits are consistent between both samples, and the energy resolution in simulation calculated from the time integral matches very well with the one computed from data (Fig. 5.10) with only 3 % of difference and thus within the uncertainties.

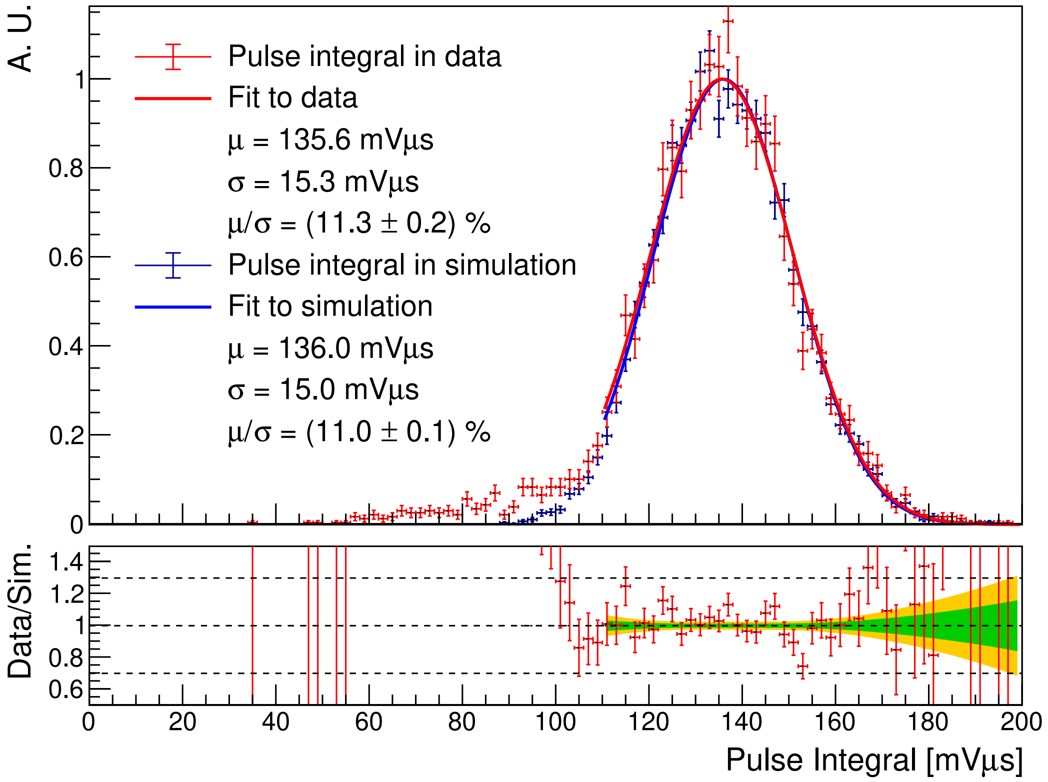

Figure 5.10: Comparison between the distributions of time integral for data (red), with an energy resolution of (11.3 ± 0.2)%, and simulation (blue), with (11.0 ± 0.1)% energy resolution, both normalized to the maximum of the fitted Gaussian functions. Extending the fit range to include the tail of the pulse integral in data increases the energy resolution calculated from the Gaussian fit by 0.1 %. The lower plot represents the confidence interval of the fit of a Gaussian function to the pulse integral of the simulated samples, with green and yellow bands corresponding to 68 % and 95 %, respectively. The red error points are calculated as the ratio between the data points and the function previously described.

The performed simulation only considers an ideal signal and the reproduction of the noise in data. Therefore, in this TES system, the energy resolution for 1064 nm photons can be explained by the effects of the baseline noise, consisting of 200 kHz harmonics, and the white and Brownian noise contributions. The origin of the tail representing low energy events in data (Fig. 5.1b) is related to the coupling efficiency of the optical fiber with the TES, and it is discussed in section 6.2. This effect does not appear in simulations.

The low-frequency part of the PSD exerts the most significant influence on the energy resolution, as shown in appendix B. Even reducing the amplitudes of high frequencies (> 100 kHz) by one order of magnitude, the energy resolution stays very similar at 10.6 % compared to 11.0 % without reduction. In contrast, when reducing low frequencies (< 100 kHz) by 25 %, the energy resolution is reduced to 8.6 %.

CHAPTER

6

OPTIMIZING ANALYSIS FOR BACKGROUND REDUCTION

Contents

The optimization of the TES data analysis is key to reducing the background events discussed in chapters 3 and 4 in order to fulfill the ALPS II requirements. A frequency domain-based analysis aiming to improve the energy resolution for 1064 nm photons was developed. This was briefly covered in [56]. A deconvolution method was also implemented to improve the analysis computation time and the recognition of low-energy pulses and pulse pile-ups in a timeline. This chapter will discuss these topics in detail and present a modification to the simulation shown in the previous chapter, arising from the new analysis.

6.1 Analysis in the frequency domain

As shown in section 2.1.1, the SST applied to describe the response of the TES to a photon predicts a signal corresponding to the Eq. 2.15. This function could be modified for a fitting procedure by including the terms that determine the pulse amplitude in a single parameter $\mathrm{A_{SST}}$ and shifting the time with the parameter $\mathrm{t_0}$ to take into account the photon's arrival time in a trigger window. The resulting fitting function would be Eq. 6.1.

$$\mathrm{U_{SST}(t)} = \begin{cases} \mathrm{A_{SST}} \left(\exp\left\{ -\frac{1}{\tau_+}(\mathrm{t} - \mathrm{t_0}) \right\} - \exp\left\{ -\frac{1}{\tau_-}(\mathrm{t} - \mathrm{t_0}) \right\} \right), & \mathrm{t} \geq \mathrm{t_0} \\ 0, & \text{else} \end{cases} \tag{6.1}$$

Fitting this function to the pulse observed in a time window of the data, analogously to section 5.1, would allow to extract $\mathrm{A_{SST}}$, τ_+ and τ_-, parameters related to actual physical magnitudes which characterize the TES. However, this function is not differentiable, making the fitting unstable [96]. Therefore, is not suitable for a fitting procedure as previously discussed.

Converting Eq. 6.1 to the frequency domain solves this difficulty. The Fourier transform of this equation is calculated using Eq. 6.2.

$$\mathscr{F}[\mathrm{U_{SST}(t)}](\mathrm{f}) = \int_{-\infty}^{\infty} \mathrm{U_{SST}(t)} \cdot \mathrm{e}^{-\mathrm{i}2\pi \mathrm{ft}}\, \mathrm{dt} \tag{6.2}$$

The result corresponds to Eq. 6.3. A step-by-step demonstration is shown in the appendix A.5.

$$\mathscr{F}[\mathrm{U_{SST}(t)}](\mathrm{f}) = -\mathrm{A_{SST}} \cdot (\tau_- - \tau_+) \frac{[1 - (2\pi \mathrm{f})^2 \tau_+ \tau_-] - \mathrm{i}2\pi \mathrm{f}(\tau_+ + \tau_-)}{[1 + \tau_+^2 (2\pi \mathrm{f})^2][1 + \tau_-^2 (2\pi \mathrm{f})^2]} \exp\{-2\pi \mathrm{fit_0}\} \tag{6.3}$$

The Fourier transform (Eq. 6.3) of Eq. 6.1 is not piece-wise defined, and the parameters keep their physical meaning. The Eq. 6.3 is complex, as it has real and imaginary parts.

The fitting procedure in the frequency domain was implemented using the built-in libraries in ROOT [54, 97], modifying the minimization using χ^2 to consider the simultaneous fit in the real and imaginary planes. The χ^2 is defined as the sum of χ^2_{re} of the real part and χ^2_{im} of the imaginary part. The parameters $\mathrm{A_{SST}}$, τ_+, τ_- and $\mathrm{t_0}$ are shared between both functions.

A Fast Fourier Transform (FFT) is applied to a time window of the data (Fig. 6.1a) to obtain its real part (Fig. 6.1c) and imaginary part (Fig. 6.1d). The uncertainty for every frequency $\mathrm{e_{re,im}(f)} = \sqrt{\mathrm{T} \cdot \mathrm{PSD(f)}/2}$ is computed from the PSD of the noise in the data (Fig. 6.1b), where T is the duration of the time window containing the pulse. The PSD(f) is obtained as explained in section 5.2.

The time integral of the signal fitted in the frequency domain can be calculated, by definition (Eq. 6.4), by evaluating Eq. 6.3 at zero with the parameters obtained from the fitting procedure.

$$\mathscr{F}[\mathrm{U_{SST}(t)}](0) = \int_{-\infty}^{\infty} \mathrm{U_{SST}(t)}\, \mathrm{dt} = \mathrm{I_{SST}} \tag{6.4}$$

A comparison between the pulse integral distributions computed for the time and frequency analyses from the same dataset is shown in Fig. 6.2. The energy resolution is computed as explained in section 5.1. The result improves the energy resolution from (11.3 ± 0.2)% and

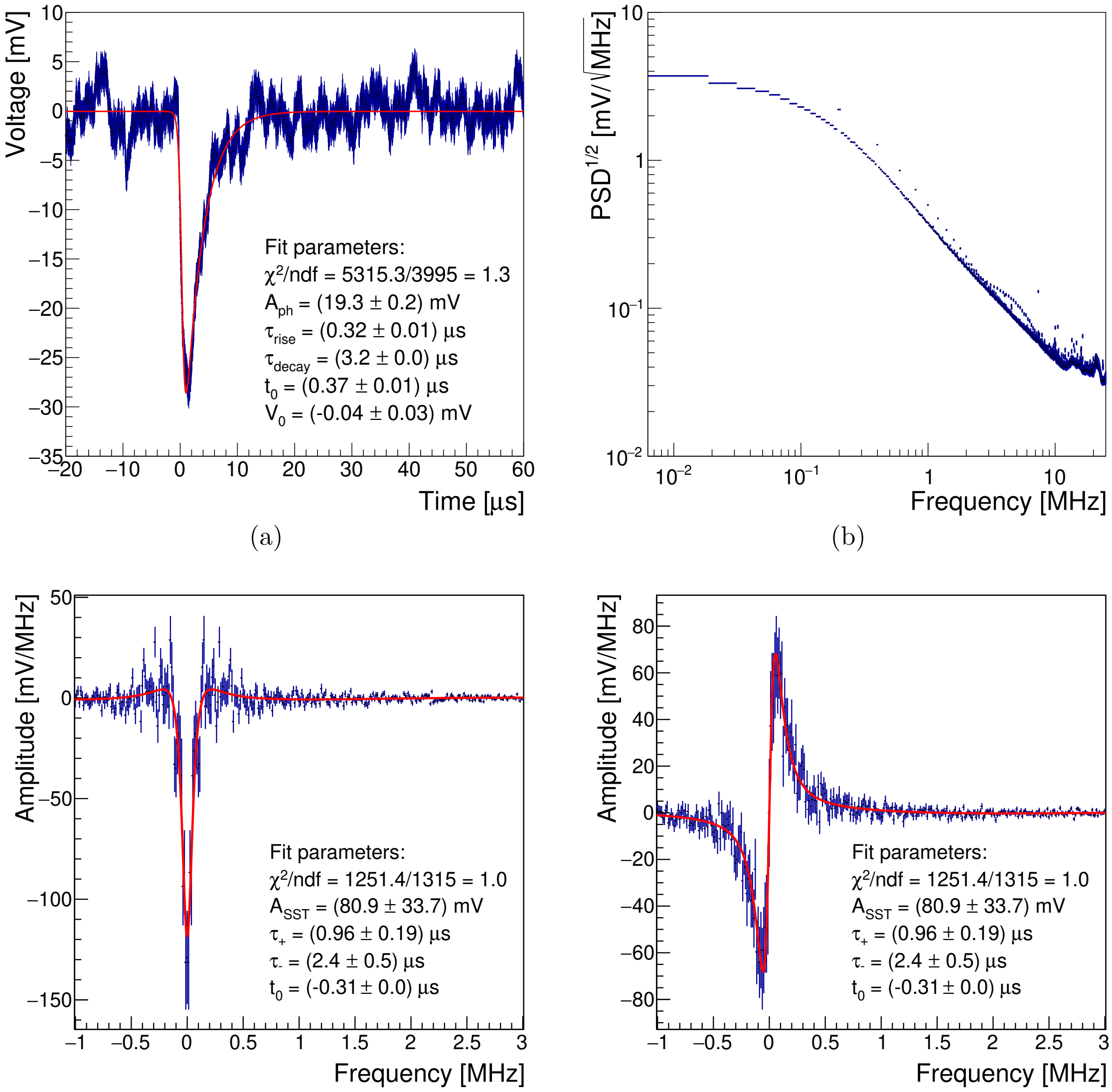

(a) (b) (c) (d)

Figure 6.1: (a) Measured 1064 nm pulse fitted to the phenomenological model and parameters obtained from the fitting procedure. (b) PSD of the noise in the same dataset. (c, d): The real part (c) and imaginary part (d) of the Fourier Transform fitted to the SST model in the frequency domain and fit parameters.

FWHM of 0.31 eV to ER = (9.9 ± 0.2)%, with a FWHM of 0.27 eV. This represents an improvement of approximately 10 % with respect to the time domain analysis.

The analysis in the frequency domain is based on Eq. 6.1 coming from the SST, where the parameters A_{SST}, τ_+, and τ_- are related to the TES physical parameters. Finding A_{SST}, τ_+, and τ_- means that the TES parameters can be calculated from theory, as shown in section 3.3.

The photon signal in the frequency domain is dominant over the noise only in a range of relatively low frequencies (lower than 1 MHz) compared to the sampling rate of 50 MHz. Therefore, the fit can be limited to this range, reducing the number of data points to be fitted while maintaining a good signal-to-noise ratio. The fitting function has one parameter less than the phenomenological model, as V_0 is only an offset in the zero frequency point.

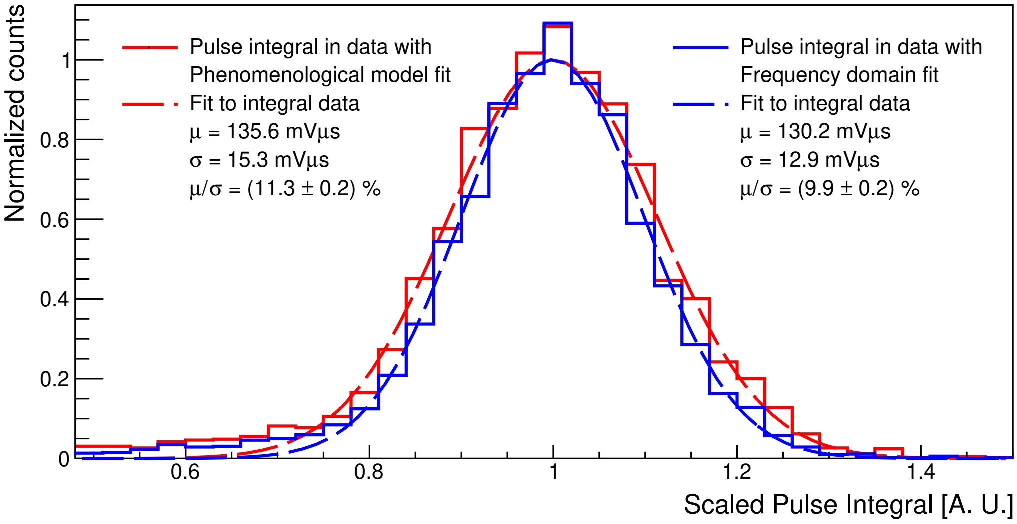

Figure 6.2: Comparison between the normalized pulse integrals calculated in the time domain (red) and the frequency domain (blue). The mean value of the integral is lower in the frequency domain (130.2 mVμs) than in the time domain (135.6 mVμs). There is an improvement of 10 % in the energy resolution in the frequency domain fit compared to the phenomenological approach.

These two factors contribute to a substantial reduction in the time required to perform the fitting procedure. Further optimization will be discussed in section 6.4.

6.2 Pulse height as a compromise between energy resolution and TES linear response

The expression for the integral of the pulse, calculated from the fit parameters, corresponds to $I_{SST} = A_{SST}(\tau_+ - \tau_-)$. When analyzing the 2D distribution of the parameters A_{SST}, τ_+ and τ_- in Fig. 6.3a and 6.3b, it can be observed that despite the parameters are rather spread, they appear to follow a defined correlation. In Fig. 6.3b, it can be seen that the pulse integral (green line) does not follow the profile of the distribution of the amplitude and the decay time (blue error bars). The consequence of this is that the pulse integral spreads with certain values of the fit parameters, as evidenced in Fig. 6.4a, where the central value of the pulse integral shifts depending on the decay time of the pulse. Therefore, it is possible that other variables could better describe the correlations between A_{SST}, τ_+ and τ_-, e.g. a variable which would minimize its distance to the points dispersed around the profile of the distribution (blue error bars).

Considering the measurement of a voltage pulse, the pulse height h_{SST} is a magnitude that naturally comes to mind. It can be computed from Eq. 6.1 by first calculating the position in time of the minimum and then the value of the function in that point following Eq. 6.5.

$$h_{SST} = U_{SST}(t_{max}), \qquad t_{max} = \frac{\tau_+\tau_-}{\tau_- - \tau_+} \ln\frac{\tau_-}{\tau_+} + t_0 \tag{6.5}$$

Analogous to the integral of the pulse, sufficient statistics allow the calculation of the

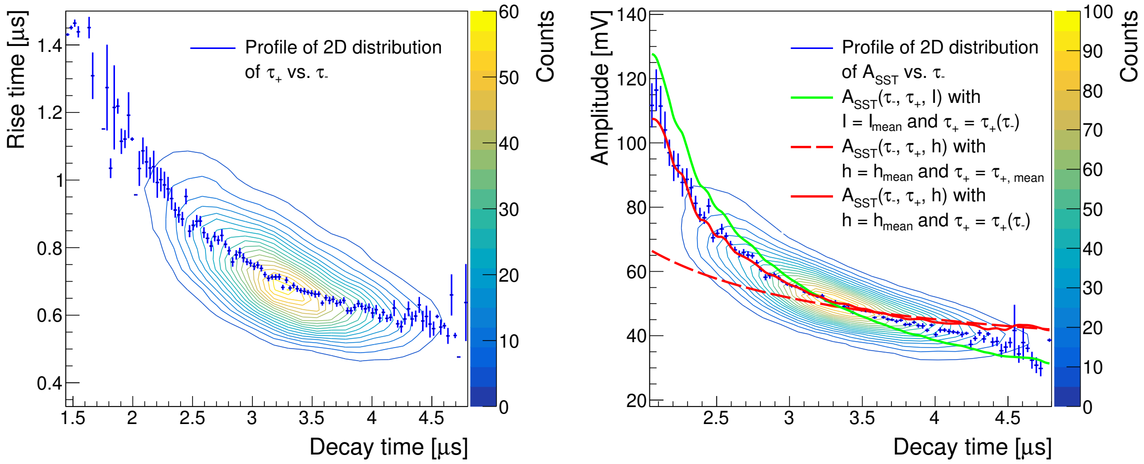

(a) (b)

Figure 6.3: (a) Contour of the 2D distribution of the rise time τ_+ and decay time τ_- fit parameters in the frequency domain. The blue error bars correspond to the profile of the decay time distribution, i.e. for every bin in the decay time axis, the mean and the standard deviation of the rise time distribution are computed, corresponding to the value and the error at that decay time. (b) Analogous to the rise time and decay time distribution, but with amplitude A_{SST} and decay time τ_-. The variable $\tau_+ = \tau_+(\tau_-)$ is computed from the profile of the 2D distribution of rise time vs. decay time in Fig. 6.3a. The green curve $A(\tau_-, I) = I/(\tau_- - \tau_+(\tau_-))$ is calculated by fixing the pulse in integral to the mean of the distribution in Fig. 6.2, $I = I_{mean}$. The red curve $A(\tau_-, h) = h_{SST} A / U_{SST}(t_{max}(\tau_-, \tau_+(\tau_-)))$, is calculated by fixing the pulse height $h = h_{mean}$ instead of the pulse integral. The red dashed curve is computed similarly to the red curve but fixes the rise time to its mean value $\tau_+ = \tau_{+,mean}$. It can be seen that the red curve fits best the profile of the distribution.

energy resolution for the pulse height. Fig. 6.5 shows the normalized pulse height distribution calculated from the fitting results of 1064 nm photons in the frequency domain. The resulting energy resolution is ER = $(5.12 \pm 0.06)\%$, with a FWHM of 0.14 eV. This represents an improvement by a factor of two compared to the integral of the pulse calculated using the frequency domain analysis.

The pulse height can also be computed from the fitting results of 1064 nm photons in the time domain using Eq 6.6.

$$h_{ph} = U_{ph}(t_{max}), \qquad t_{max} = \frac{\tau_{rise}\tau_{decay}}{\tau_{decay} + \tau_{rise}} \ln \frac{\tau_{decay}}{\tau_{rise}} + t_0 \tag{6.6}$$

The corresponding normalized distribution of 1064 nm pulses is shown in Fig. 6.5. The resulting energy resolution for the pulse height calculated from the time domain is ER = $(5.73 \pm 0.08)\%$, with a FWHM of 0.16 eV. This is 11 % worse than the same magnitude computed from the frequency domain, but much better than for the pulse integral.

A possible explanation for the improvement in energy resolution using the pulse height instead of the pulse integral is that the pulse height receives a lower influence from the Brownian noise, which dominates the energy resolution for the pulse integral as seen in section 5.3. The maximum amplitude of the pulse is reached in 1 – 2 μs. Therefore, it is under the influence of high frequencies, where Brownian noise has a lower contribution.

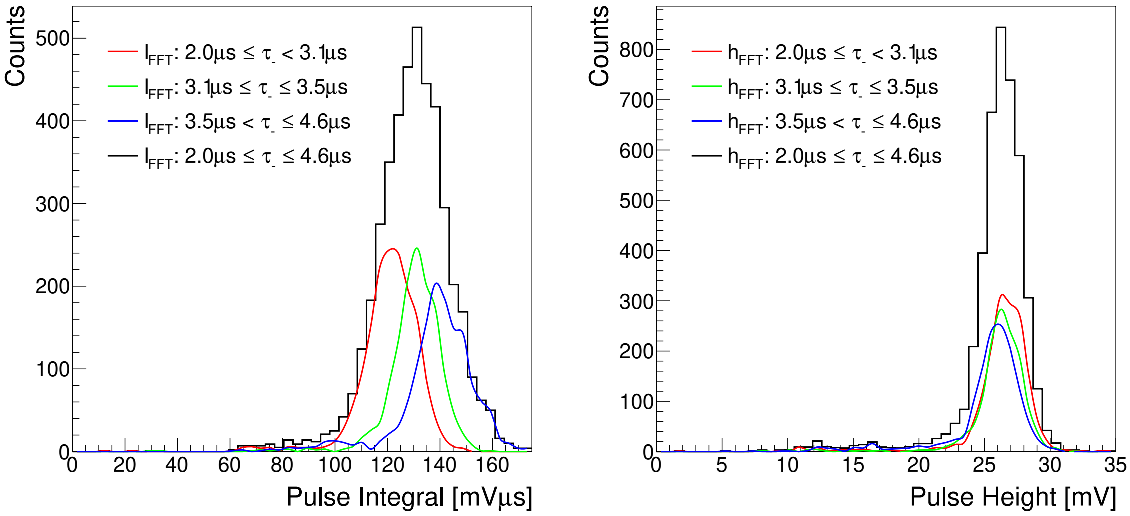

(a) (b)

Figure 6.4: (a) Pulse integral in the frequency domain computed for several intervals of the decay time. From Fig. 6.3b, it is expected that the distribution of the integral is shifted towards lower values of the integral for lower values of the decay time and the opposite for high values of the decay time. The result of this is that the total integral distribution is broadened. (b) Pulse height in the frequency domain computed for several intervals of the decay time. The shift of the mean of the pulse height for different decay time ranges is reduced. Therefore, the width of the total pulse height distribution is narrower than the one from the pulse integral, resulting in an improvement in energy resolution.

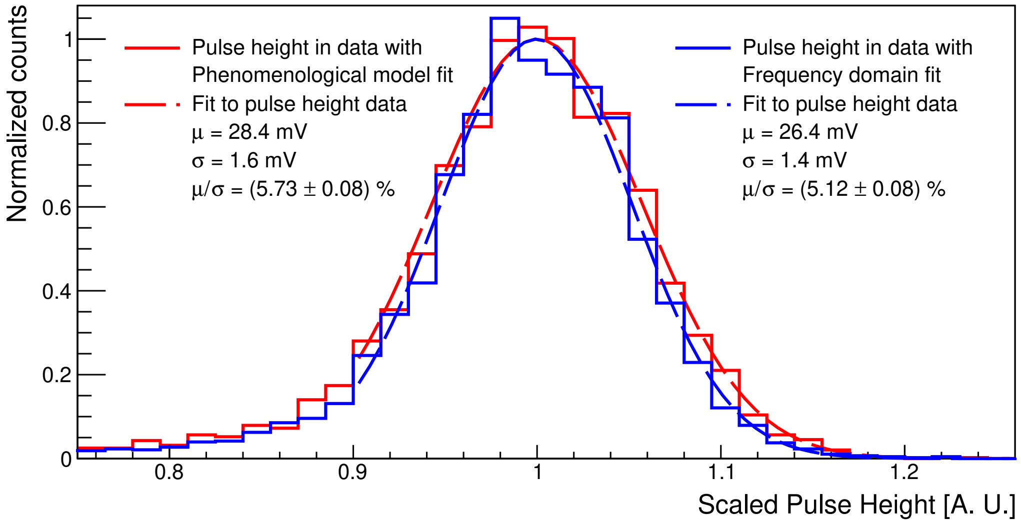

Figure 6.5: Comparison between the normalized pulse heights calculated in the time domain (red) and the frequency domain (blue). As with the time integral, the mean value of the pulse height is lower in the frequency domain (26.4 mV) than in the time domain (28.4 mV). The improvement of 10 % in the energy resolution in the frequency domain fit compared to the phenomenological approach is also observed here.

From the mathematical point of view, the pulse height (red line) better describes the profile of the distribution of the fit parameters in Fig. 6.3b. It only fits the profile if the correlation of τ_+ with τ_- is considered. If it is neglected (red dashed line), the pulse height results in a worse data description than the pulse integral.

Overall, considering the improvement coming from the implementation of the frequency domain analysis and the use of the pulse height to describe the energy, the energy resolution is enhanced from ER = $(11.3 \pm 0.2)\%$, FWHM of 0.31 eV, to ER = $(5.12 \pm 0.06)\%$, with a FWHM of 0.14 eV. In total, an improvement of 55 % in energy resolution is achieved for the analyzed dataset.

How the pulse height and energy resolution behave for other wavelengths should also be observed to evaluate the usefulness of these results. Due to availability, only 750 nm and 642 nm were analyzed additionally. The distributions for the pulse integral from the time domain analysis and the pulse height from the frequency domain analysis are shown in Fig. 6.6a and Fig. 6.6b.

As shown in section 3.4.2, the pulse integral is expected to be more linear with energy than the pulse height. This is consistent with the results from Fig. 6.6. One could conclude that the pulse integral is more optimal for working with lower wavelengths than 1064 nm. However, this is a misleading result since it does not consider the resolution in both parameters. Therefore, the proposed figures of merit θ to compare Fig. 6.6a and Fig. 6.6b are the probabilities of 642 nm and 750 nm photons being identified as 1064 nm wavelength by falling in the range $[\mu_{1064\text{nm}} - 2\sigma_{1064\text{nm}},\ \mu_{1064\text{nm}} + 2\sigma_{1064\text{nm}}]$. In general, for a given wavelength x and a variable that describes the energy (I: Integral, h: pulse height) following a Gaussian distribution, θ is computed as:

$$\theta_I = \int_{\mu_{1064\text{nm}}-2\sigma_{1064\text{nm}}}^{\mu_{1064\text{nm}}+2\sigma_{1064\text{nm}}} g(I, \mu_x, \sigma_x)\, dI \tag{6.7}$$

$$\theta_h = \int_{\mu_{1064\text{nm}}-2\sigma_{1064\text{nm}}}^{\mu_{1064\text{nm}}+2\sigma_{1064\text{nm}}} g(h, \mu_x, \sigma_x)\, dh \tag{6.8}$$

For 750 nm and using the pulse integral to calculate the energy, $\theta_{I_{750\text{nm}}} = 6.0 \cdot 10^{-2}$, whereas using the pulse height $\theta_{h_{750\text{nm}}} = 1.4 \cdot 10^{-5}$. For 642 nm, the results are $\theta_{I_{642\text{nm}}} = 3.8 \cdot 10^{-4}$ and $\theta_{h_{642\text{nm}}} = 4.7 \cdot 10^{-13}$. It is concluded that, for the analyzed dataset, the pulse height is the best magnitude to discern photons of different energies. This does not take the low energy tail observed in data into account. This is discussed later in the present section.

λ	μ_I	σ_I	μ_h	σ_h	Expected μ
1064 nm	1.000 ± 0.002	0.112 ± 0.002	1.000 ± 0.001	0.0515 ± 0.0007	1.00
750 nm	1.408 ± 0.002	0.118 ± 0.002	1.324 ± 0.001	0.0536 ± 0.0008	1.42
642 nm	1.626 ± 0.004	0.119 ± 0.003	1.457 ± 0.001	0.0497 ± 0.0012	1.66

Table 6.1: Values of μ and σ of the Gaussians in Fig. 6.6 for different wavelengths λ. The μ from the Gaussian fitted to the peaks computed using the pulse height and integral are compared to the expected value of μ. The expected value of μ is the proportion between 1064 nm and the wavelength under study.

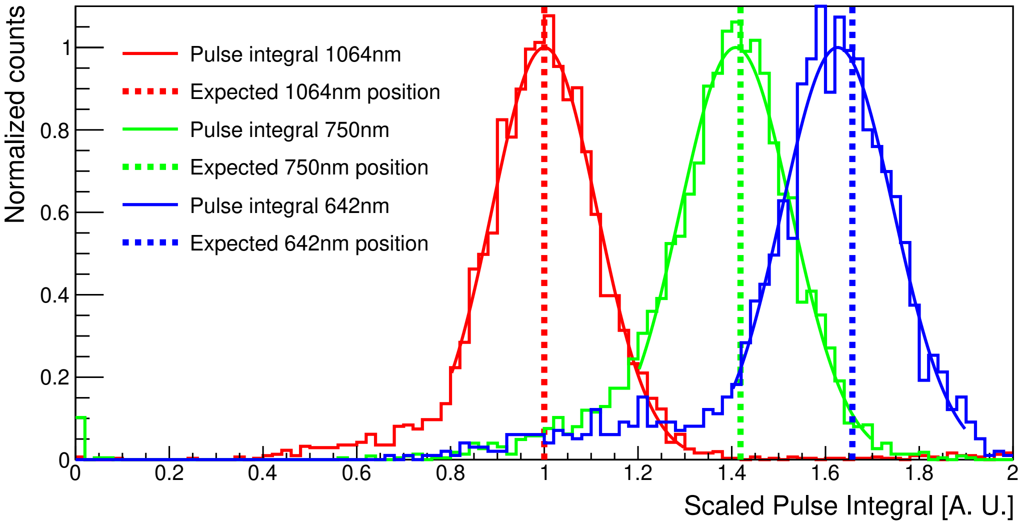

(a)

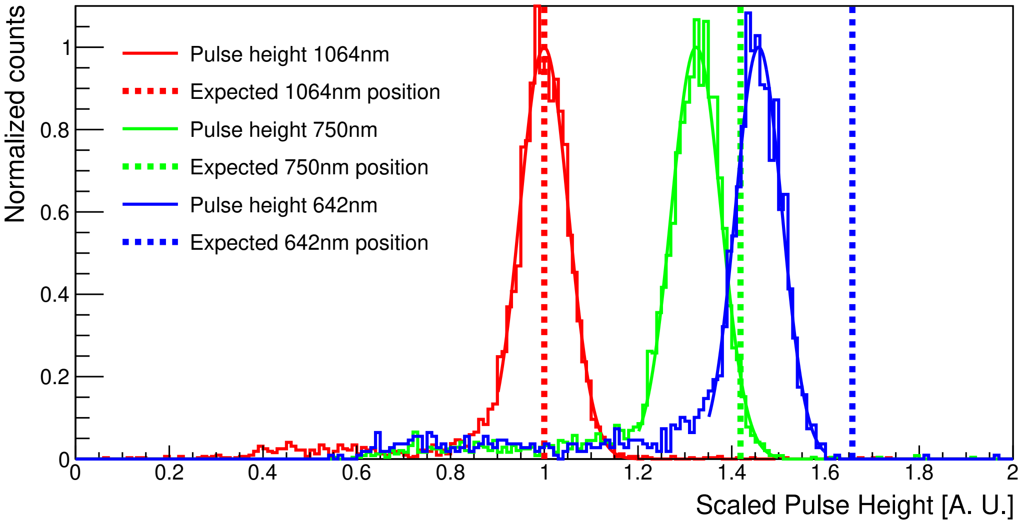

(b)

Figure 6.6: (a) Distribution of the pulse integral computed from the phenomenological approach for 1064 nm, 750 nm and 642 nm photons. (b) Distribution of the pulse height computed from the frequency domain analysis for 1064 nm, 750 nm and 642 nm photons. The results of the fit of Gaussian functions to the peaks are summarized in Table. 6.1. The dashed lines in both plots show where the means should be if the TES response were linear at 1.00, 1.42 and 1.66, respectively.

For ALPS II, discerning between 532 nm from 1064 nm photons is key for background rejection since 532 nm will be the wavelength used for cavity control with the TES [28]. Extrapolating from the results with 1064 nm, 750 nm, and 642 nm, the probability of one 532 nm being identified as 1064 nm can be calculated. It is considered that the mean value of the Gaussian functions describing the pulse height and the pulse integral follow the same tendency of increasing with energy as the higher wavelengths and that the width of the distributions remains constant. A grade 2 polynomial with an intercept at zero is fitted to the mean values of the Gaussians in Fig. 6.6, resulting in the expressions for the pulse integral and the pulse height:

$$\frac{\mathrm{I_x}}{\mathrm{I_{1064nm}}} = -0.03\mathrm{r_x^2} + 1.03\mathrm{r_x} \tag{6.9}$$

$$\frac{\mathrm{h_x}}{\mathrm{h_{1064nm}}} = -0.18\mathrm{r_x^2} + 1.19\mathrm{r_x} \tag{6.10}$$

where $\mathrm{r_x}$ is the ratio between the energy of the photon and the energy of a 1064 nm photon. The values of μ and σ of the Gaussians for different wavelengths, pulse height and integral are summarized in Table 6.1. As expected, the pulse height (Eq. 6.10) has a higher coefficient in the squared term than the pulse integral (Eq. 6.9).

Nevertheless, $\theta_{\mathrm{I_{532nm}}} = 1.0 \cdot 10^{-10}$ and $\theta_{\mathrm{h_{532nm}}} = 1.6 \cdot 10^{-25}$ for 532 nm, evidencing again that the pulse height has more discerning power than the pulse integral.

A caveat on this reasoning is that it did not consider the low energy tail in the spectra shown in Fig. 6.6a and Fig. 6.6b, which also appeared in section 5.3. In [74], the low-energy tail is attributed to the photons hitting the boundary between the TES and the aluminum rails used to bias and read the signal of the TES [74]. This would agree with the results of a first attempt to measure the coupling efficiency between the optical fiber and the TES, being approximately 8%. The setup was similar to a later attempt with results published in [56], but using constant attenuation instead of variable. In [56], the measured efficiency was greater than 90%. Fig. 6.7a shows how the size of the beam incident in the TES could change for both efficiency measurements. Comparing the pulse height distributions when the efficiencies are approximately 8% and 90%, in Fig. 6.7b, it can be seen that the tail disappears, which confirms the contribution of the heat dissipation in the rails. This means that a high coupling efficiency is required to dampen the tail in the Gaussian distributions.

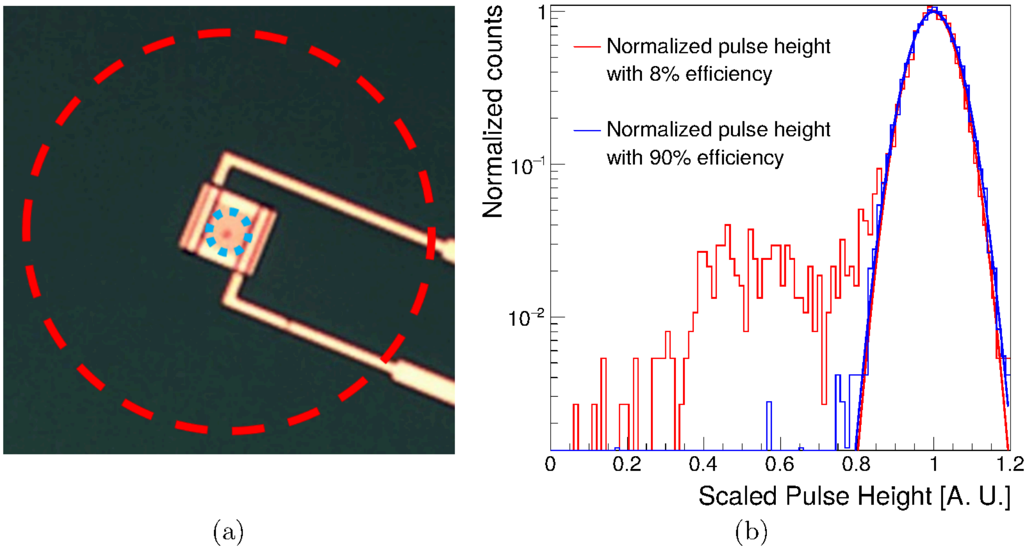

(a) (b)

Figure 6.7: Picture of the TES (square in the center) and the circular area of the light beam for the setups with 8% (dashed blue) and 90% (dashed red) coupling efficiency between the optical fiber and the TES. Photons hitting the boundary between the TES and the rails would not deposit as much energy in the TES as the ones hitting the center of the square. Image adapted from [11]. (b) Pulse height distributions for the setup with 8% and 90% efficiency. The low pulse height tail in the distribution is suppressed when the efficiency is the highest.

6.3 Correlation in fit parameters

The time domain fitting function (Eq. 5.1) and the frequency domain fitting function Eq. 6.3 have different parameters, $\{A_{ph}, \tau_{rise}, \tau_{decay}\}$ and $\{A_{SST}, \tau_+, \tau_-\}$ respectively, directly related to the shape of the pulse. These parameters present very different distributions for 1064 nm photons as shown in Fig. 6.8 and Fig. 6.3 as examples of $\{A_{ph}, \tau_{rise}, \tau_{decay}\}$ and $\{A_{SST}, \tau_+, \tau_-\}$ distributions respectively.

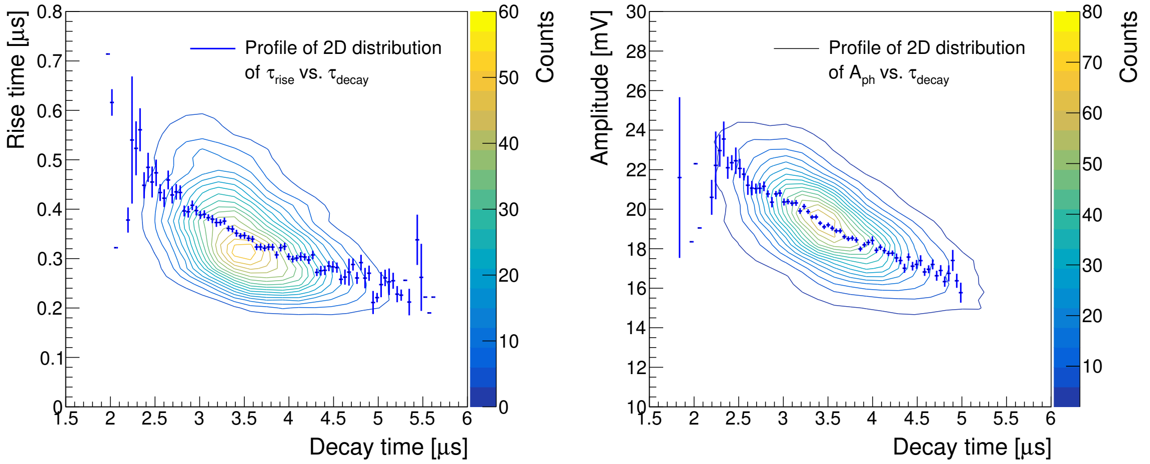

(a) (b)

Figure 6.8: The contour of the 2D distribution and the profile of the distribution of the decay time (see Fig. 6.3), from the phenomenological model, for (a) the rise time τ_{rise} and decay time τ_{decay}, and (b) the amplitude A_{ph} and decay time τ_{decay}.

The cuts in the parameter space from the frequency domain fit could be used in addition to the cuts imposed in the time domain fit parameter space as performed previously within the TES group [43]. However, 1D cuts may not be optimal due to the shape of the fit parameter distributions. Cuts in 2D on a parameter as a function of another could be applied, for example, with the form $\tau_+ > m\tau_- + n$. Furthermore, an additional parameter space extends the possibility of background rejection based on Machine Learning methods as previously done with the time domain [59] in parallel to the cut-based analysis.

The correlations among the parameters could also be exploited to enhance the energy resolution further. This is hinted by the fact that the pulse height does not match exactly the correlation between A_{SST} and τ_-, shown in Fig. 6.3b. It is also evidenced in Fig 6.4b given that the three distributions (red, green and blue) should be the same in an ideal case.

AlazarGUI upgrade

The correlations among the frequency domain fit parameters are diminished when operating the SQUIDs at a higher GBWP as shown in Fig. 6.9. Implementing a cut-based analysis with more localized parameters would be easier. Moreover, the signal's rise time also decreases with a higher GBWP, improving the discrimination against the pile-up of pulses.

However, in the TES module studied, increasing the GBWP of the SQUIDs increases the amplitude of the noise from the 200 kHz harmonics, mentioned in section 5.2.4. Taking data at high GBWP becomes difficult, as the harmonics create spikes in signal as shown

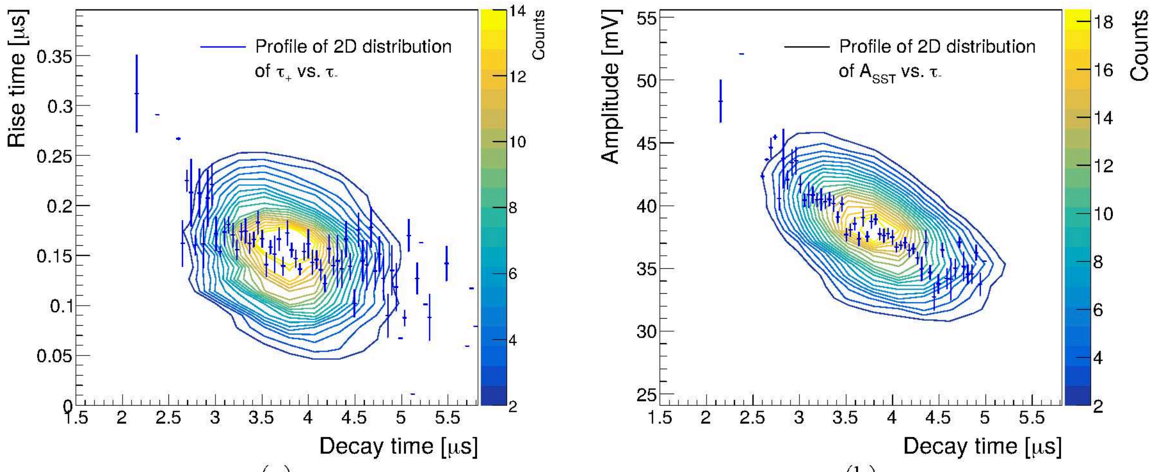

(a) (b)

Figure 6.9: For a high GBWP of 6.2 GHz, the distribution of fit parameters is more localized compared to Fig. 6.3. The figure shows the contour of the 2D distribution and the profile of the distribution of the decay time (see Fig. 6.3), from the frequency domain analysis, for (a) the rise time τ_+ and decay time τ_-, and (b) the amplitude A_{SST} and decay time τ_-.

in Fig. 6.10a, drastically increasing the overall trigger rate as the spikes pass the trigger threshold implemented in the DAQ system described in section 2.2.3.

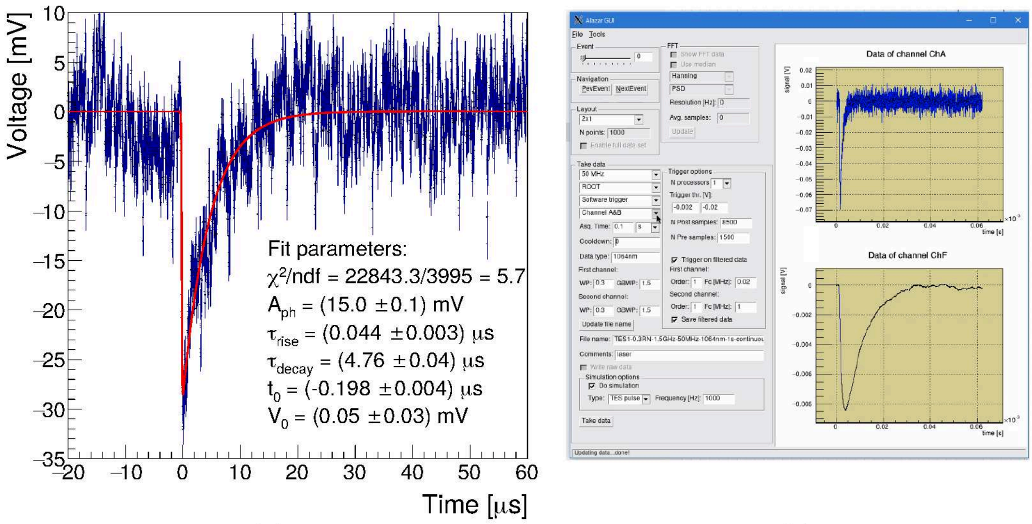

(a) (b)

Figure 6.10: (a) Measured 1064 nm pulse at higher GBWP of 6.2 GHz fitted to the phenomenological model and parameters obtained from the fitting procedure. The 200 kHz harmonics produce spikes every 5 µs. (b) Screenshot of the AlazarGui showing the acquired data at the top, and the filtered data at the bottom used to trigger the acquisition. The cut frequency of the filter was set very low, making the pulse significantly slower.

To cope with this difficulty, a low-pass filter following the expression 5.5 from section 5.2.5 was implemented in the DAQ software. The data is filtered only for triggering purposes; the unfiltered data is kept so the information is not lost. Fig. 6.10b shows how the trigger would be applied to the filtered data, and the information shown in Fig. 6.10b is saved for later analysis.

In parallel to implementing the filter for triggering, further upgrades were implemented in the AlazarGUI. These upgrades are covered in appendix D and are under testing.

6.4 Deconvolution of TES signal

In order to further optimize the analysis, an extra step could be performed before the fitting procedure. The parameter t_0 could be found beforehand given that the rise of the pulse is very fast compared to the noise. However, the employed method would need to be robust due to the presence of 200 kHz noise explained in section 5.2.4. For example, a method consisting on detecting peaks in the derivative of the timeline does not perform well given that the peaks produced by 200 kHz noise could be even higher than the ones for 1064 nm pulses in some cases, as would be the case for the pulse in Fig. 6.10a. This method also has the disadvantage that with the decay of the signal the derivative does not restore back to zero but takes a positive value. In this way, if there is another signal right after, the derivative will have a lower amplitude, making detecting pile-ups also difficult.

In the following, a method is developed to address the computation of t_0 and the detection of the pile-up of pulses.

In section 6.1, the Fourier space of the TES signal was used to implement a fitting procedure using Eq. 6.3 in the frequency domain corresponding to the expected response of the TES to a photon. A known response to a photon in the frequency domain means that it is possible to use a Fourier deconvolution method to search for photon pulses in a timeline. The deconvolution method consists of the reverse of the convolution operator. In signal processing, the Fourier deconvolution is used to revert computationally a distortion due to the effect of a physical process [99], i.e. an electrical filter or the energy resolution of a device.

In this case, the TES signal is considered as the convolution between an energy deposition in the TES occurring in a very short time (Dirac delta in the time domain) and the known response (Eq. 6.3 with $A_{SST} = 1$ mV and $t_0 = 0$). An algorithm for the deconvolution of the TES pulses based on the one described in [99] was programmed. In the frequency domain, the deconvoluted signal D(f) is computed by dividing the convoluted signal or original signal S(f) by the known response model M(f), taking into account that both components are complex (Eq. 6.11).

$$D(f) = \frac{S(f)}{M(f)} = \frac{Re\{S\}Re\{M\} + Im\{S\}Im\{M\}}{|M|^2} + i\frac{Im\{S\}Re\{M\} - Re\{S\}Im\{M\}}{|M|^2} \tag{6.11}$$

If $S(f) = A_{dec} \cdot M(f)$ then $D(f) = A_{dec}$, therefore the result of the reverse Fourier transform of D(f) is a Dirac Delta, $d(t) = A_{dec}\delta(t)$. If the signal S(f) is shifted in time with respect to the model by t_0 and fulfills the same condition as before, $S(f) = A_{dec} \cdot M(f) \exp\{-i2\pi t_0 f\}$, then $D(f) = A_{dec} \cdot \exp\{-i2\pi t_0 f\}$ and the reverse transform of D(f) is a Dirac Delta shifted in time also by t_0, $d(t) = A_{dec}\delta(t - t_0)$. As the Fourier transform is linear, if several signals are present with different amplitude A_{dec_i} and time shifts t_{0i}, $D(f) = \sum A_{dec_i} M(f) \cdot \exp\{-i2\pi t_{0i} f\}$, then the result is the sum of Dirac Deltas $d(t) = \sum A_{dec_i}\delta(t - t_{0i})$.

As shown in section 5.3 the TES can be described as the superposition of an ideal signal and the baseline noise. The deconvolution can be performed using Eq. 6.3 as the model, in the form $M(f) = \mathscr{F}[U_{SST}(t, A_{SST} = 1, \tau_+ = \tau_{m+}, \tau_- = \tau_{m-}, t_0 = 0)](f)$. The baseline noise is problematic for this algorithm because it dominates the high frequencies, then dividing by M(f) amplifies its effects, therefore it is not possible to identify the deconvoluted TES pulse in the time domain as evidenced in Fig. 6.11a.

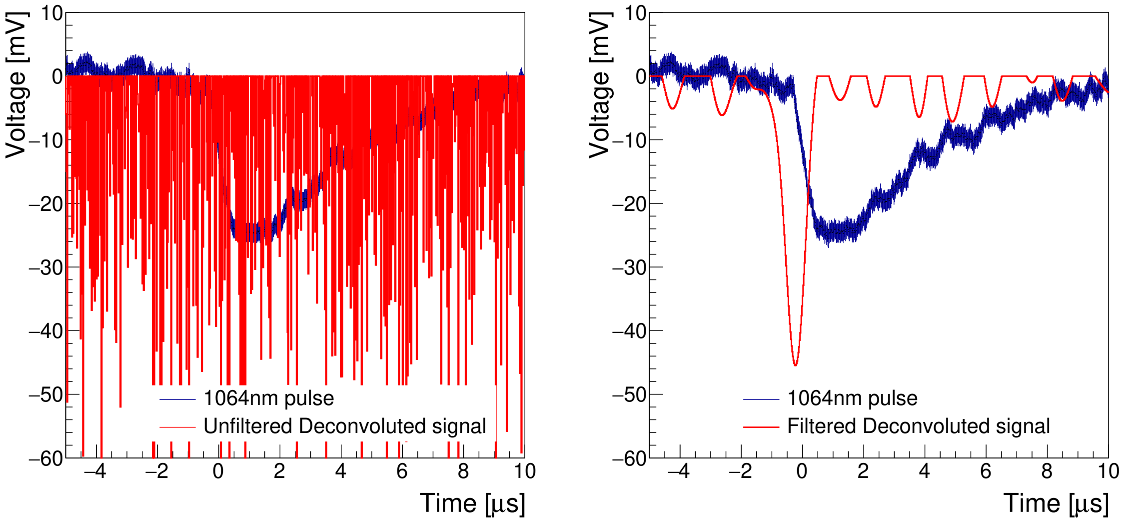

(a) (b)

Figure 6.11: (a) A 1064 nm pulse from data and its deconvolution without filtering. No features can be distinguished in the timeline. (b) Same data but with a filter in the deconvolution at $\sigma = 0.5$ MHz, resulting in a peak with a FWHM of $\Delta t = 0.75$ µs

The effect of the high-frequency noise is overcome by applying a low-pass filter over the deconvoluted signal d(t) as shown in [99]. For the application in the TES, a specific low-pass filter was chosen to control the shape of the deconvoluted signal. A filter with the form described by Eq. 6.12 has as reverse Fourier transform a Gaussian function (Eq. 6.13) with maximum value $g(t_{max}) = 1$.

$$G(f) = \frac{1}{\sqrt{2\pi}\sigma} \exp\{-f^2/2\sigma^2\} \tag{6.12}$$

$$\mathscr{F}^{-1}[G(f)](t) = g(t) = \exp\{-\pi^2\sigma^2t^2\} \tag{6.13}$$

The previous expression D(f) for several pulses without filtering, becomes now $D(f) = \sum A_{dec_i} M(f) \cdot \exp\{-i2\pi t_{0i} f\} G(f)$, therefore the resulting output in the time domain is the sum of Gaussians $d(t) = \sum A_{dec_i} g(t - t_{0i})$. Adjusting σ defines where the high-frequency noise is cut. Moreover, as Eq. 6.13 represents a Gaussian function with $\sigma' = 1/2\pi\sigma$, the time resolution is described by the FWHM and can be computed as $\sigma_t = \text{FWHM} = 2.355\sigma'$. The resulting deconvolution with Gaussian filter can be seen in Fig. 6.11b. The chosen value of σ allows the filtering of the noise and improves the signal-to-noise ratio. As in section 5.2.4, the class `TSpectrum`, from ROOT, can be used to identify the heights A_{dec_i} and positions t_{0i} of the Gaussians, corresponding to the arrival time of the TES pulses. A threshold $A_{dec_{min}}$ can be set on the heights as a criterion to identify pulses.

In general, the performance of this algorithm will depend on four parameters: τ_{m+} and τ_{m-} describing the rise and decay time respectively of the model to describe the TES signal,

σ describing the cut frequency of the Gaussian filter, and $A_{dec_{min}}$ the threshold for selection of pulses.

To maintain an optimal signal-to-noise ratio with real TES pulses, the values of τ_{m+} and τ_{m-} should be as close as possible to the fit parameters obtained from the frequency domain based fitting procedure. With enough statistics, they can be chosen as the mode of the 2D distribution of τ_+ vs. τ_-. Otherwise, the individual 1D distribution mode of τ_+ and τ_- can be used.

The possible tuning of the values of σ and $A_{dec_{min}}$ for the computation of t_0 and the detection of pile-ups is described in the following. Additionally, by variating the tuning criteria, the algorithm can be used as a pulse finder, even being able to differentiate between signal and background, as will be explained later in this section. The optimal parameters for each scenario are evaluated by analyzing simulated pulses considering the combined results of chapter 5 and section 6.5.

Starting time of signal

The computation of the arrival time of pulses t_{0i} is a direct consequence of using the deconvolution algorithm. The values of t_{0i} are determined from the positions of the Gaussians found with the class `TSpectrum`, from ROOT.

The accuracy of this method depends on the cut frequency defined before. The standard deviation presents a much lower value than the defined time resolution Δt, although it also depends on the height of the pulse. Testing its accuracy with the simulation of 1064 nm pulses, it can be seen that the resolution in the arrival time of the pulse is reduced to several samples, as shown in Fig. 6.12a. A test with 2128 nm simulated pulses gave similar results but with a broader distribution. The same happens for 1064 nm pulses if a higher cut frequency is used.

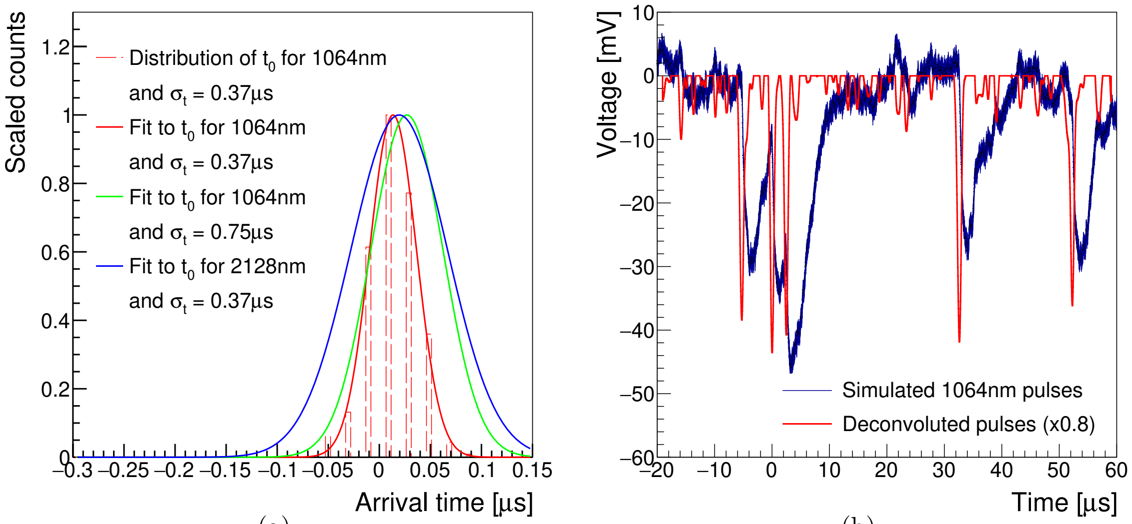

(a) (b)

Figure 6.12: (a) Distribution of arrival time t_0 for simulated samples with the start time of the signal at 0. The distribution broadens for lower energies and cut frequencies (worse time resolution). (b) Simulated pulses at a high rate. The deconvolution produces a peak per pulse. If a threshold is imposed over peaks of the noise but below the peaks of the pulses, e.g. at 20 mV, the peaks which pass the threshold can be identified as signals.

An additional advantage of this method is that by obtaining the arrival time, this value can be introduced in the parameter t_0 of the fitting procedure in the frequency domain and then t_0 is fixed, improving the analysis time by reducing the parameters to fit by one and improving the accuracy of the other parameters.

The amount of pulses that can be found in a timeline is only limited by the time resolution σ_t. As shown in Fig. 6.12b, a Gaussian will correspond to every peak, and the algorithm in `TSpectrum` can recognize every one of them if the distance between peaks is higher than their FWHM, for Fig. 6.12b FWHM would be equivalent to $\sigma_t = 0.75\mu s$.

Rejection of clear background events

The computation time of the deconvolution method is lower than the time required for the fitting procedure in the time analysis as it depends on the speed of the Fast Fourier Transform (FFT) calculation. For comparison, in a laptop using one core, the analysis of 4600 triggers takes approximately 8 minutes, and the deconvolution takes nearly 15 seconds, a factor of 30 times faster. This would allow using the deconvolution method as a discriminant before the fitting procedure, as it is sensitive to the shape of the pulses. Slow pulses are decomposed into several small peaks that, in most cases, do not pass a threshold for 1064 nm pulses, as shown in Fig. 6.13a. The threshold for 1064 nm pulses is also chosen to reject triggers produced by electronic noise. The algorithm could become critical when analysing background measurements with low trigger thresholds in the DAQ, as more than 10^6 triggers could be collected in a few days.

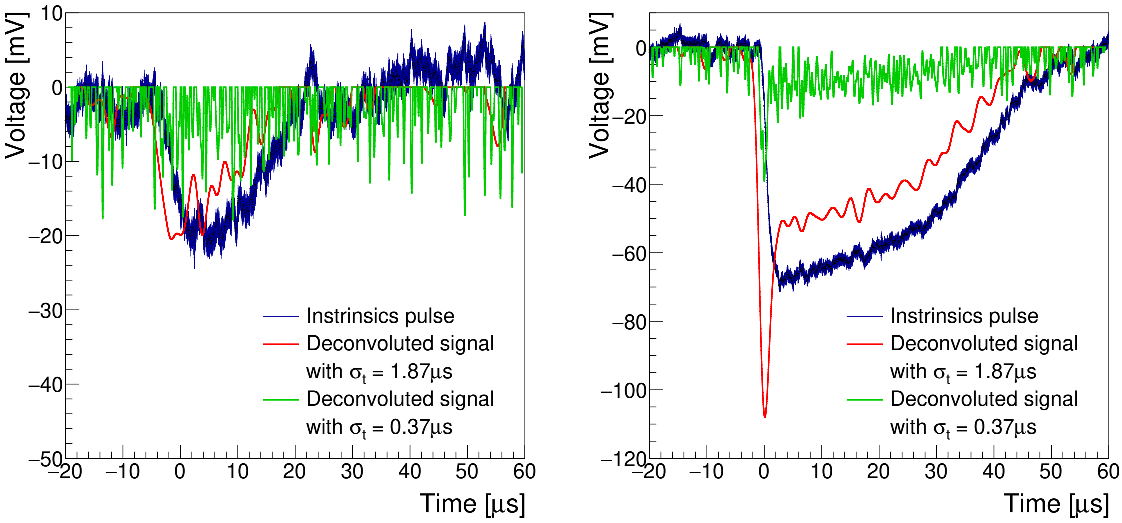

(a) (b)

Figure 6.13: (a) Slow pulse from intrinsic background data. Its deconvolution is also a slow signal different from the deconvolution of 1064 nm pulses. (b) Saturation pulse from the same dataset. The deconvolution of this signal peak is higher (between 80 mV and 120 mV) than the usual 1064 nm photons peak (between 40 mV and 60 mV).

Lastly, saturation pulses produce a peak much higher than the ones for 1064 nm photons. As shown in Fig. 6.13b, a threshold high enough, e.g. above 70 mV, allows identifying and rejecting these pulses before the fitting analysis.

Pile-up detection

The time resolution of the deconvolution method can be tuned to select pulses without pile-up. As evidenced in Fig. 6.14a, for a high time resolution, a pile-up signal can be decomposed in two small peaks which do not pass a given threshold.

σ	σ_t	2.0μs	1.0μs	0.5μs	0.25μs	0.0μs
0.2 MHz	1.87μs	0.0	73.5	99.6	99.9	100.0
0.5 MHz	0.75μs	0.0	0.0	21.6	95.5	99.2
1.0 MHz	0.37μs	0.1	0.3	0.5	33.0	95.1

Table 6.2: Acceptance in % as one 1064 nm pulse of the deconvolution algorithm applied on two simulated 2128 nm pile-up pulses with several time differences (top row) at different cut frequencies σ (left column) and a threshold for peak identification of 40 mV. Pulses with a time difference of 0 would be equivalent to 1064 nm pulses. The timelines containing the signal are accepted if only one peak passes the threshold in the deconvolution.

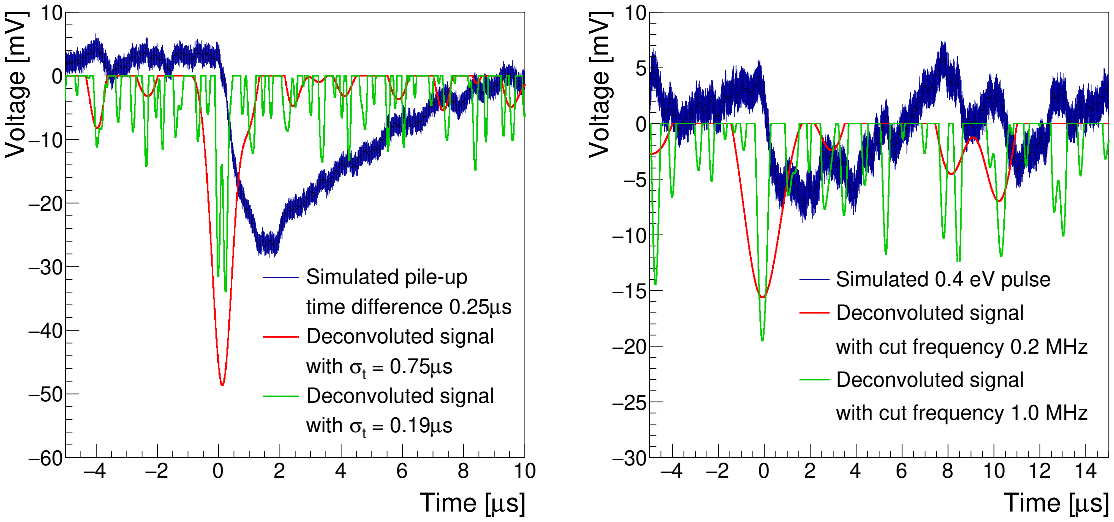

(a)

(b)

Figure 6.14: (a) Simulated pile-up of two 2128 nm pulses at a time difference of 0.25 μs and their deconvolution using two different time resolutions. The two peaks corresponding to each of the two pulses can be observed for a time resolution of 0.19 μs. (b) Simulated 3098 nm photon pulse and its deconvolution using lower cut frequencies (higher time resolutions). For the lowest cut frequency, the signal-to-noise ratio of the deconvolution improves, so the height of the peak corresponding to the photon becomes twice as large as the height of the highest peak of the noise.

Imposing the condition that a 1064 nm must pass the threshold, this algorithm gives a great discrimination power against pile-up, as seen in table 6.2 for different values of the cut frequency. As the time resolution is improved by increasing the cut frequency in the algorithm, the signal-to-noise ratio worsens; therefore, a compromise between both magnitudes needs to be found.

Detection of low energy pulses

Tuning the deconvolution method in the opposite direction by worsening the time resolution improves the signal-to-noise ratio, as shown in Fig. 6.14b.

σ	0.7 eV		0.5 eV		0.4 eV		0.3 eV		0.2 eV		noise
0.2 MHz	100.0	0.0	98.4	0.0	80.0	0.0	29.9	0.0	3.2	0.0	0.1
0.5 MHz	100.0	0.0	95.5	0.2	75.2	0.8	35.9	2.2	8.1	3.6	4.4
1.0 MHz	99.8	0.2	86.1	10.5	59.7	33.6	32.5	51.9	12.5	63.5	73.4

Table 6.3: Acceptance in % of the deconvolution for simulated pulses (left value) and wrongly identifying noise instead of signal in the same timeline (right value), with given energies (top row) at several cut frequencies σ (left column) and a threshold for peak identification of 15 mV (the peak of the deconvoluted signal is beyond -15 mV in Fig. 6.14b). The timelines containing the signal are accepted if at least a peak passes the threshold in the deconvolution. The most right column contains the acceptance for timelines with only noise.

With this condition, photon pulses become prominent, contributing to discriminating even low-energy pulses from the noise. Table 6.3 shows different thresholds and cut frequencies results.

The power of this technique is evident, allowing the detection of pulses with energies as low as 0.3 eV with 30 % acceptance while rejecting almost all the noise samples. This could be applied in the planned efforts for direct dark matter detection in the TES group, where detecting low-energy photon-like pulses becomes important to increase the sensitivity to low masses [84].

6.5 Signal simulation based on SST

With a fitting procedure that can find the 1064 nm pulse parameters corresponding to the SST and an algorithm that can find the position of a pulse in a timeline very precisely, the method to recreate the 1064 nm pulse in the signal simulation discussed in section 5.2.1 can be revisited.

The mean pulse of measured 1064 nm photons gives a good approximation of how a 1064 nm photon signal would look without the electronic noise. To avoid contamination of low-energy photons only pulses with a pulse height and pulse integral within 1-sigma of the Gaussian distributions shown in Fig. 6.5 and 6.2 respectively are selected to compute the average of the 1064 nm signal. The uncertainty is calculated as the standard deviation of the mean at every timeline point. With enough statistics, the uncertainty of the fit parameters becomes sufficiently small, so the effect of their variations on the worsening of the energy resolution is smaller than the energy resolution of the sensor. As shown in Fig. 6.15a, the phenomenological function does not fit well to the mean pulse, with a reduced chi-squared $\chi_{\text{red}} = 173.2 \gg 1$. This happens mainly because the rise of the phenomenological function is slow compared to the sharp rise of the pulse in the data.

In order to obtain the most precise mean pulse possible, the deconvolution method is implemented to correct the position of the pulses in the timeline and reject timelines with

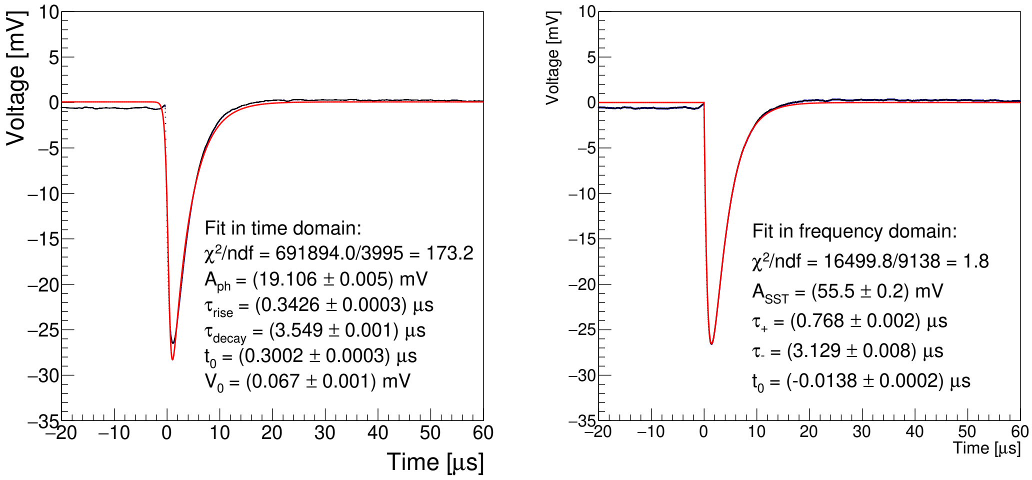

(a) (b)

Figure 6.15: (a) The mean of trigger windows containing measured 1064 nm pulses fitted to the phenomenological model and the computed fit parameters. The uncertainty of a point in the signal is the uncertainty of the mean of the distribution of values at that point. (b) The mean of the same trigger windows, but shifted by the t_0 computed with the deconvolution, so that every pulse starts simultaneously. The resulting pulse is fitted in the frequency domain, and the fit parameters are used to represent the signal in the time domain using Eq. 6.1.

more than one pulse. Therefore, this method is used twice, first with a good signal-to-noise ratio with a cut frequency of $\sigma = 0.2$ MHz and a threshold at 15 mV to recognize the possible pulses in the timeline and secondly, with a good time resolution of 0.12 µs (cut frequency of $\sigma = 3.0$ MHz) and a threshold of 30 mV, requiring that the highest peak from the deconvolution in the timeline is at a maximum distance of 0.1 µs from the pulse found in the previous step. As shown in section 6.4, the high cut frequency in the last step would give the correct positioning of the pulse in the timeline to a precision of single samples. The pulses are shifted according to the found arrival time t_0 in the frequency domain using the following expression:

$$\mathscr{F}'[U_{SST}(t)](f) = \mathscr{F}[U_{SST}(t)](f) \exp\{2\pi i \cdot f \cdot t_0\} \tag{6.14}$$

where $\mathscr{F}[U_{SST}(t)](f)$ was defined in Eq. 6.3. Using the shift defined by Eq. 6.14, every pulse starts at the same point in the timeline. The mean pulse is then computed and fitted to Eq. 6.3 in the frequency domain, and the transformation results to the time domain are shown in Fig. 6.15b.

Even though the uncertainties for every point in the signal are very small, the signal is relatively well-fitted by the function from the SST, with a $\chi_{red} = 1.8$. The differences are probably caused by the high-pass filter discussed in section 3.3, producing the shift in the base voltage before and after the pulse observed in Fig. 6.15a and 6.15b.

The fit parameters A_{SST}, τ_+ and τ_- are computed with an uncertainty below 0.4 %, and they can be used to produce a signal in the simulation using Eq. 6.1. The simulation results are compared to the measured data in Fig. 6.16 and 6.17. The distributions are in good agreement in both the time domain and the frequency domain parameters. The results of the energy resolution in data and simulation are shown in Table 6.4.

While the simulation agrees with data concerning the pulse integral's energy resolution, the

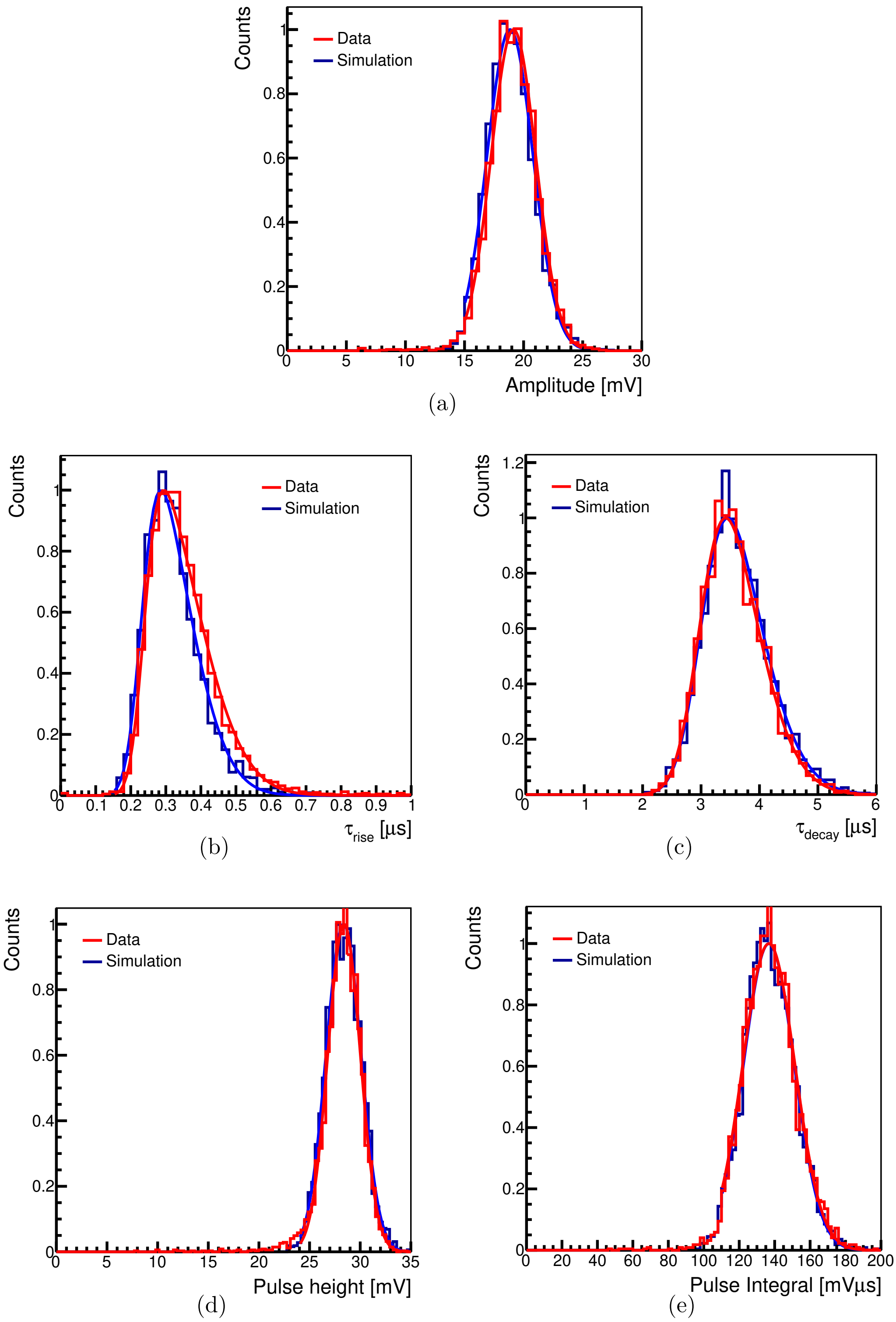

(a)

(b)

(c)

(d)

(e)

Figure 6.16: Distribution of parameters obtained by fitting the phenomenological model to measured 1064 nm pulses and simulated pulses: (a) Amplitude, (b) Rise time, (c) Decay time, (d) Pulse height, and (e) Pulse integral

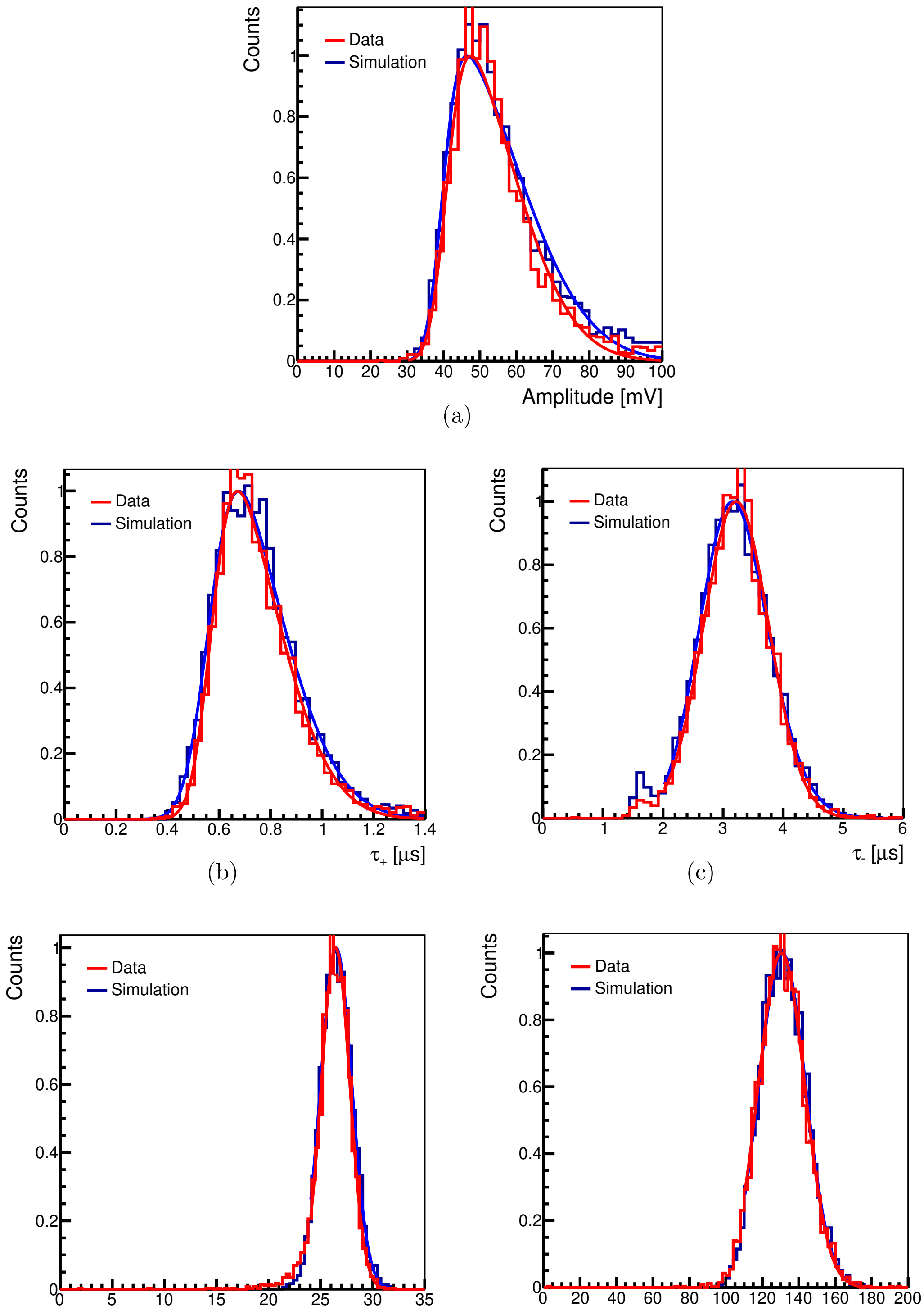

(a)

(b)

(c)

(d)

(e)

Figure 6.17: Distribution of parameters obtained by fitting the frequency domain SST model to measured 1064 nm pulses and simulated pulses: (a) Amplitude, (b) Rise time, (c) Decay time, (d) Pulse height, and (e) Pulse integral

	Data	Simulation	Simulation/Data
Pulse integral time domain	$(10.8 \pm 0.2)\%$	$(10.5 \pm 0.2)\%$	0.97 ± 0.03
Pulse height time domain	$(5.63 \pm 0.07)\%$	$(6.09 \pm 0.08)\%$	1.08 ± 0.02
Pulse integral frequency domain	$(9.8 \pm 0.2)\%$	$(9.8 \pm 0.2)\%$	1.00 ± 0.03
Pulse height frequency domain	$(5.12 \pm 0.08)\%$	$(5.63 \pm 0.09)\%$	1.10 ± 0.02

Table 6.4: Comparison of the computed energy resolution in measured 1064 nm photons and their simulation.

pulse height's energy resolution is slightly worse. This discrepancy could be explained by the differences in data with respect to the model used for the simulation. As Fig. 6.15b shows, there is a shift in the baseline before and after the pulse. This is produced by a high-pass filter as a consequence of the readout electronics of the TES. However, the proper shape of the filter is still under study.

6.6 Reduction of extrinsic background

In chapter 4, the extrinsics data was analyzed in the time domain, with an energy resolution of 11.3 % computed from the time integral. This can be revisited now, including the enhancements explained in this chapter. To the cut analysis based on the rise time, decay time and reduced χ^2 mentioned in section 4.3 based on the time domain, cuts in the parameters τ_+, τ_- and χ^2_{red} from the frequency domain can be added to improve the rejection of non-photon pulses at low energies. Details can be found in appendix C. The resulting calibrated spectrum is shown in Fig. 6.18 for the pulse integral in the time domain and the pulse height in the frequency domain.

Range (σ)	Analysis efficiency	Rate (I_{Ph})	Rate (h_{FFT})
$-1, 1$	67.2%	$1.7 \cdot 10^{-3}$cps	$1.2 \cdot 10^{-4}$cps
$-2, 2$	93.9%	$5.6 \cdot 10^{-3}$cps	$4.1 \cdot 10^{-4}$cps
$-3, 3$	98.1%	$1.1 \cdot 10^{-2}$cps	$1.5 \cdot 10^{-3}$cps
$0, 3$	49.1%	$4.2 \cdot 10^{-4}$cps	$6.9 \cdot 10^{-5}$cps
$-1, 3$	82.6%	$1.9 \cdot 10^{-3}$cps	$1.6 \cdot 10^{-4}$cps

Table 6.5: Comparison of the rates computed for measured extrinsics data using the pulse integral from the time domain analysis (I_{Ph}) and the pulse height from the frequency domain analysis (h_{FFT}) to calculate the energy of the photons. The analysis efficiency combines a cut efficiency of 98.4 % and the efficiency resulting from excluding 1064 nm photons outside the σ ranges, as defined in section 4.4. The cut efficiency is reduced compared to Table 4.1 due to the additional cuts in the frequency domain explained in appendix C.

As predicted in section 4.4, improving energy resolution narrows the BBR spectrum and

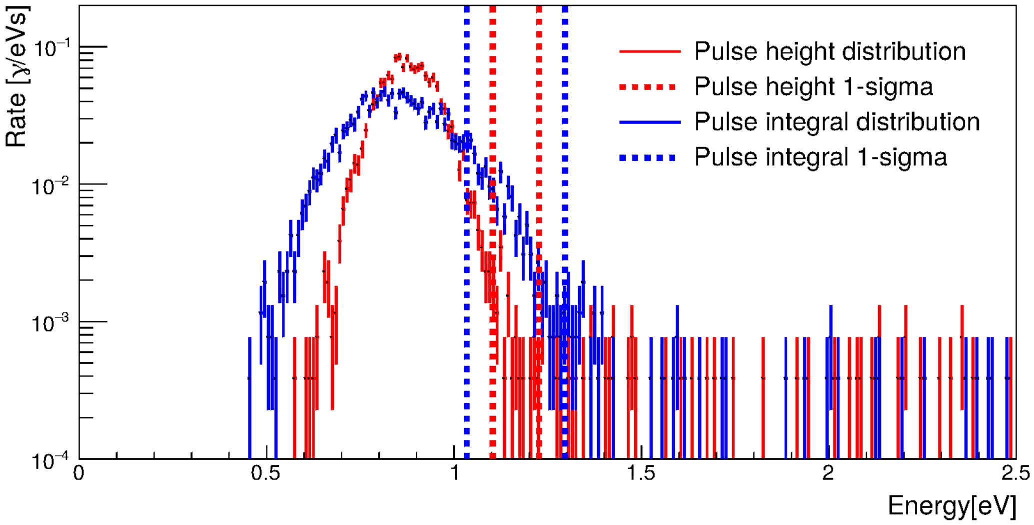

Figure 6.18: Measured extrinsics spectrum computed using the pulse integral from the time domain analysis (blue) and the pulse height from the frequency domain analysis (red).

reduces the 1064 nm photon signal region, effectively reducing the extrinsic background rates in the 1064 nm region. The results of the measured rates with the optimized analysis are summarized in Table 6.5 for the same σ ranges defined before.

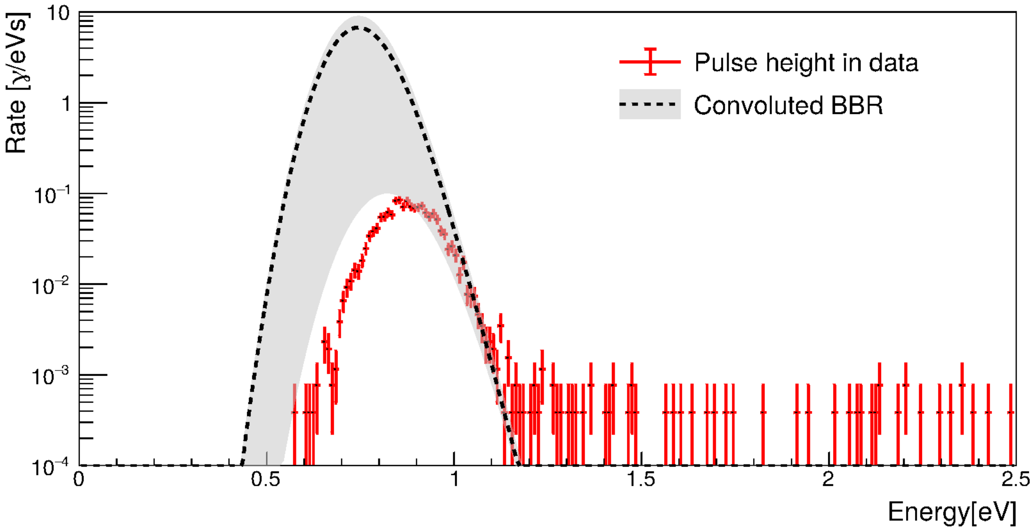

Figure 6.19: Simulated spectrum in Fig. 4.11, folded with the new energy resolution, compared to the measured rates from data. The pulse height computed from the analysis was scaled to energy using a 1064 nm sample as a reference.

Comparing the simulation results, considering the improved energy resolution, in Fig. 6.19, it can be seen that the right part of the spectrum is less influenced by the uncertainty of fiber curling. The simulation resembles the data tendency in the region between 0.95 eV and 1.2 eV. Above 1.2 eV, the presence of events remains, possibly events from intrinsic backgrounds surviving the cut discrimination. The cause of the excess events in the 1-sigma signal region (between 1.10 eV and 1.22 eV) with respect to the simulation should be investigated, as this indicates that their origin is not BBR.

Overall, the improvement in energy resolution by a factor of 2, as the result of the enhancement in the analysis explained in this chapter, reduces the background rate in every range by an order of magnitude compared to the computed in chapter 4, but still does not satisfy the requirements for ALPS II.

CHAPTER

7

CONCLUSION AND OUTLOOK

This thesis discusses the optimization of a Transition Edge Sensor (TES) for the Any Light Particle Search II (ALPS II) experiment with the goal of employing it in the search for axions and ALPs. Axions and ALPs are well motivated by theoretical facts and experimental observations; for instance, they provide an elegant solution to the strong CP problem [5], and they are a good dark matter candidate [9]. Furthermore, they provide a feasible explanation for the anomalies observed in the stellar evolution [20].

The TES is a superconducting detector that operates in the transition region between superconducting and normal conducting states [41]. In this region, a signal is produced when an energy deposition induces a temperature change which translates into a change in the resistance of the sensor. The TES studied in the present work is a tungsten microchip provided by the NIST of dimensions 25 µm × 25 µm × 20 nm, with a critical temperature around 140 mK. Its properties make it sensitive to energies in the order of 1 eV, and it is optimized for the efficient detection of 1064 nm photons. To reach the operating temperatures, the TES is placed in the coldest stage of a cryostat at approximately 25 mK.

The ALPS II experiment may produce a signal coming from an axion/ALP at a rate of one 1064 nm photon per day [28]. Reducing the background level as much as possible is a determinant to enhance the significance at this low signal rate. With this goal in mind, this thesis focused on different approaches.

A deep understanding of the TES system is needed in order to propose modifications to the measurement setup for background reduction. Experimentally, the background can be investigated in two main setups: intrinsics, where the TES is isolated inside the cryostat, and extrinsics, where an optical fiber is connected to the TES, with the other end placed in the dark at room temperature outside the cryostat. A two-fold simulation was deployed to study the intrinsic background, comprising two components. First, a Geant4-based framework was developed to describe the energy depositions induced by cosmic ray muons and radioactivity produced by zirconia in the fiber sleeve used to couple the optical fiber to the TES. This framework was named GELB-TES, standing for Geant4-based Events from Low Backgrounds in a Transition Edge Sensor. The second component employs COMSOL Multiphysics to simulate the effect produced in the TES by the energy deposition computed with GELB-TES. Notably, the background produced by zirconia was found to be the dominant contribution, and the total rate is provided as a function of the manufacturing conditions of the zirconia. The obtained background rate range is compatible with the measured intrinsics rate.

In the extrinsics configuration, compared to intrinsics, an additional contribution to the background coming from Black Body Radiation (BBR) is expected [86]. A framework named "BBR Spectrum Builder" was deployed to simulate the propagation of the BBR to the TES. This framework was designed to have the flexibility to adapt to different experimental conditions. The low-energy part of the computed Black Body spectrum is found to be rather sensitive to the bending of the optical fiber as it passes towards the TES. An important conclusion from the BBR simulation is that the background can be reduced by improving the energy resolution. This motivates the simulation of the TES signal to evaluate the contribution of the baseline noise to the energy resolution and the optimization of the TES data analysis.

The signal simulation was performed by superposing simulated noise and an ideal 1064 nm photon pulse. The simulated noise recreates the power spectral density of the noise extracted from data. The parameters that describe the shape of a 1064 nm pulse are obtained from the mean pulse generated by averaging a set of measured 1064 nm photon data samples. Without any further tuning, the energy resolution computed for the simulated signal agrees with the one from the measured data. This implies that the baseline noise can explain the energy resolution in the TES system studied in this thesis.

Based on the ideas extracted from the BBR simulation, another path for optimizing the TES system was enhancing the data analysis. A frequency domain-based analysis was introduced with this goal in mind. As a result, the energy resolution improved by 10 % for the analyzed sample. A further improvement by a factor of two was achieved by computing the pulse height analytically from the fitted function procedure instead of the pulse integral. This quantity has less linear behavior than the pulse integral. Nevertheless, the power to discriminate 1064 nm photons from lower wavelengths increased due to the improvement in energy resolution. Furthermore, a pulse finding algorithm based on signal deconvolution was implemented for the determination of the arrival time of pulses and the identification of piled-up pulses. Finding the arrival time of pulses allowed for speeding up and improving the stability of the fitting procedure in the frequency domain. The pulse finding algorithm allows the rejection of two simulated pulses with a wavelength of 2128 nm, adding one 1064 nm pulse, with good efficacy. Moreover, tuning the parameters of the pulse finding algorithm allows the rejection of background events before the fitting procedure is done, speeding up the data analysis. In addition, it enables the identification of pulses with an energy as low as 0.2 eV while rejecting most of false triggers due to electronic noise. Finally, as a result of the improvement in energy resolution, the measured rate of extrinsic events was reduced by an order of magnitude, confirming the predictions of the BBR simulation. The measured spectrum indicates the existence of non-Black Body events in the region around 1064 nm, although the evidence is statistically limited.

The libraries containing the signal simulation and the optimized data analysis were organized in a framework named TESPASS, which is based on ROOT [54] and stands for TES pulse analysis and signal simulation.

Taking the results of the intrinsic background simulation into account, three approaches are proposed for its mitigation. Firstly, the source of background could be reduced, i.e., by substituting the zirconia for more radio-pure material or removing the zirconia fiber sleeve. The latter is not feasible for ALPS II as this reduces to almost zero the efficiency of fiber coupling to the TES, but could be used in the case of direct dark matter searches with the TES system [84]. Secondly, the reduction of the area where an energy deposition produces a signal in the TES by, for instance, placing the TES in a membrane as described in [85]. Finally, a veto detector which shares the active area with the TES could be implemented for background discrimination.

The accuracy of the simulation with COMSOL could be further improved by considering the effects of individual high-energy phonons and the formation of electron-hole pairs in the silicon substrate. Furthermore, rarer events could appear in the simulation by also taking into account the energy deposition along the tracks of the particles in the silicon substrate where the TES is located. The signal resultant from the COMSOL simulation could also be combined with the baseline noise simulated with TESPASS. These aspects will be addressed in the future.

The signal simulation included in TESPASS has been additionally used to estimate the trigger threshold acceptance of low energy pulses [84], as well as the performance of cut-based analyses to reject background while accepting as many low energy events as possible [100]. These simulations take part in the direct dark matter searches currently ongoing in the TES group. The pulse finding algorithm based on the deconvolution method could be used to improve the acceptance of low energy photons reported in [100].

The improvement in energy resolution as a result of the optimization of the data analysis allowed to get closer to the background rate goal for ALPS II. Further efforts will be dedicated to preparing the TES for a successful ALPS II data taking.

Appendices

APPENDIX

A

VERIFICATION OF MATHEMATICAL ASSUMPTIONS

A.1 Alpha beta ratio from Small Signal Theory

The ratio between the temperature sensitivity α and the current sensitivity β can be obtained from the decay time τ_- of a TES pulse in the SST.

Proof. Starting from Eq. 2.17 and the definition of the low-frequency feedback loop gain under constant current $\mathscr{L}_I \equiv P_{J_0}\alpha/GT_0$:

$$\tau_- = \tau \frac{1+\beta+R_L/R_0}{1+\beta+R_L/R_0+(1-R_L/R_0)\mathscr{L}_I}$$

For a voltage-biased TES, as is the case for this thesis, $R_L \ll R_0$.

$$\tau_- = \tau \frac{1+\beta}{1+\beta+\frac{P_{J_0}\alpha}{GT_0}}$$

$$\tau_- = \tau \frac{1}{1+\frac{P_{J_0}\alpha}{GT_0(1+\beta)}}$$

Solving for $\alpha/(1+\beta)$:

$$\frac{\alpha}{1+\beta} = \frac{\tau-\tau_-}{\tau_-}\frac{GT_0}{I_0^2R_0}$$

The value of $P_{J_0} = I_0^2R_0$ is calculated from the current I_0 and the R_0 at the TES working point. τ and G can be computed as $\tau \equiv C/G$ and $G = 5T_c^4\Sigma_W V_W$ (from section 3.3), respectively, assuming the temperature of the TES in the working point $T_0 = T_c$ given the small width of the TES transition from superconducting to normal conducting state.

□

A.2 Collection efficiency from Small Signal Theory

The energy collection efficiency η of the TES for an energy deposition from a 1064 nm photon can be computed starting from the parameter in Eq. 2.16 from the solution in the SST.

Proof. Starting from Eq. 2.16 and assuming that only a fraction η of the photon energy E changes the TES temperature by ΔT:

$$A = \frac{\mathscr{L}_I}{I_0 L \tau} \frac{C \Delta T}{1/\tau_+ - 1/\tau_-}$$

$$A = \frac{\mathscr{L}_I \tau_+ \tau_-}{I_0 L \tau} \frac{\eta E}{\tau_- - \tau_+}$$

$A(\tau_- - \tau_+)$ corresponds to the absolute value of the time integral I_{SST} of a TES pulse as shown in section 6.2 and $\tau_+ = \tau_{el}$ from Eq. 2.17. τ_{el} is defined in Eq. 2.13. Therefore,

$$I_{SST} = \frac{\mathscr{L}_I \tau_-}{I_0 L \tau} \frac{L}{R_0(1+\beta)} \eta E$$

$\mathscr{L}_I$ can be solved from the pulse decay time in Eq. 2.17 with $R_L \ll R_0$, as mentioned before:

$$\tau_- = \tau \frac{1+\beta}{1+\beta+\mathscr{L}_I}$$

$$\mathscr{L}_I = (1+\beta)\frac{\tau - \tau_-}{\tau}$$

Then,

$$I_{SST} = \frac{\tau_-}{I_0 L \tau} \frac{L}{R_0(1+\beta)} (1+\beta) \frac{\tau - \tau_-}{\tau_-} \eta E$$

$$I_{SST} = \frac{\eta E}{I_0 R_0} \frac{\tau - \tau_-}{\tau}$$

Solving for η:

$$\eta = \frac{I_0 R_0 I_{SST}}{E} \frac{\tau}{\tau - \tau_-}$$

The parameters to compute η are known as explained in the previous section.

□

A.3 Mean of the magnitude of the sum of periodic and non-periodic noise

If the PSD of noise is composed of periodic and non-periodic noise, then the mean of the total PSD is the sum of the mean of the two components.

Proof. The noise's Fourier transform can be written as a two-dimensional vector, with one component being the real part and the other the imaginary party of the Fourier transform. As the Fourier transform is a linear operator, the vector of the total noise $\vec{v}_{total}$ can be written as the addition of the periodic noise $\vec{v}_{per}$ and the non-periodic noise $\vec{v}_{nonper}$:

$$\vec{v}_{total} = \vec{v}_{per} + \vec{v}_{nonper}$$

The square of the noise magnitude is then given by:

$$|\vec{v}_{total}|^2 = |\vec{v}_{per}|^2 + 2\vec{v}_{per} \cdot \vec{v}_{nonper} + |\vec{v}_{nonper}|^2$$

The mean value, in N noise samples, of the square of the noise magnitude is:

$$\frac{\sum_{i=1}^{N} |\vec{v}_{total}|^2}{N} = \frac{\sum_{i=1}^{N} |\vec{v}_{per}|^2}{N} + \frac{\sum_{i=1}^{N} 2\vec{v}_{per} \cdot \vec{v}_{nonper}}{N} + \frac{\sum_{i=1}^{N} |\vec{v}_{nonper}|^2}{N}$$

The direction of the vector $\vec{v}_{nonper}$ is random, given that the noise is non-periodic, then the term $\sum_{i=1}^{N} 2\vec{v}_{per} \cdot \vec{v}_{nonper}/N$ vanishes. Therefore:

$$\frac{\sum_{i=1}^{N} |\vec{v}_{total}|^2}{N} = \frac{\sum_{i=1}^{N} |\vec{v}_{per}|^2}{N} + \frac{\sum_{i=1}^{N} |\vec{v}_{nonper}|^2}{N}$$

As the PSD is proportional to the square of the noise magnitude, this is equivalent to:

$$PSD_{total}(f) = PSD_{per}(f) + PSD_{nonper}(f)$$

□

A.4 Response of a low-pass filter

Considering a digital first-order low-pass filter with the form:

$$V_i^{(1)} = \beta_L V_i^{(0)} + (1 - \beta_L) V_{i-1}^{(1)}$$

The filter scales the signal in the frequency domain according to:

$$|H_L(f)|^2 = \frac{\beta_L^2}{1 + 2\left(\beta_L - 1\right)\cos\left(2\pi f \Delta t\right) + \left(\beta_L - 1\right)^2}$$

Proof. If a linear digital first-order low-pass filter has the form:

$$y[n] = \frac{1}{a_0} \sum_{k=0} b_k x[n-k] - \sum_{j=1} a_j y[n-j]$$

where y[n] corresponds to the nth filtered sample, x[n] the nth unfiltered samples, and a and b are coefficients, then the response of this filter in the frequency domain [98] is given by:

$$H_L(f) = \frac{\sum_{k=0} b_k \exp\{i2\pi f/f_s\}}{\sum_{j=0} a_j \exp\{i2\pi f/f_s\}}$$

where $f_s = 1/\Delta t$ is the sampling rate. The coefficients for the first-order low-pass filter defined before are $a_0 = 1$, $a_1 = \beta_L$ and $b_0 = \beta_L$. Then, the response of this filter can be written as:

$$H(f) = \beta \frac{1 + (\beta_L - 1)\cos(2\pi f \Delta t) + i(\beta_L - 1)\sin(2\pi f \Delta t)}{1 + 2(\beta_L - 1)\cos(2\pi f \Delta t) + (\beta_L - 1)^2}$$

The square of the absolute value of the filter response is:

$$|H_L(f)|^2 = \beta_L^2 \frac{(1 + (\beta_L - 1)\cos(2\pi f \Delta t))^2 + (\beta_L - 1)^2 \sin^2(2\pi f \Delta t)}{\left(1 + 2(\beta_L - 1)\cos(2\pi f \Delta t) + (\beta_L - 1)^2\right)^2}$$

$$|H_L(f)|^2 = \beta_L^2 \frac{1 + 2(\beta_L - 1)\cos(2\pi f \Delta t) + (\beta_L - 1)^2\cos^2(2\pi f \Delta t) + (\beta_L - 1)^2 \sin^2(2\pi f \Delta t)}{\left(1 + 2(\beta_L - 1)\cos(2\pi f \Delta t) + (\beta_L - 1)^2\right)^2}$$

$$|H_L(f)|^2 = \frac{\beta_L^2}{1 + 2(\beta_L - 1)\cos(2\pi f \Delta t) + (\beta_L - 1)^2}$$

□

A.5 Description of current from SST transformed to the frequency domain

The Fourier transform of the fitting function Eq. 6.1, which describes the TES response to a photon, corresponds to:

$$\mathscr{F}[U_{SST}(t)](f) = -A(\tau_- - \tau_+)\frac{[1 - (2\pi f)^2\tau_+\tau_-] - i2\pi f(\tau_+ + \tau_-)}{[1 + \tau_+^2(2\pi f)^2][1 + \tau_-^2(2\pi f)^2]}\exp\{-2\pi f i t_0\}$$

Proof. The Fourier transform of the function in Eq. 6.1 with $t_0 = 0$ is computed as:

$$\mathscr{F}[U_{SST}(t)](f) = \int_{-\infty}^{\infty} U_{SST}(t) \cdot e^{-i2\pi f t}\, dt$$

$$\begin{aligned}\mathscr{F}[U_{SST}(t)](f) = A \Bigg[\int_0^{\infty} \exp\left\{-\frac{t}{\tau_+} - i2\pi f t\right\} dt - \int_0^{\infty} \exp\left\{-\frac{t}{\tau_-} - i2\pi f t\right\} dt + \\ \int_{-\infty}^{\infty} V_0 \exp\{-i2\pi f t\}\, dt\Bigg]\end{aligned}$$

The term containing V_0 becomes a Dirac delta centered at zero frequency. Removing the voltage offset from the pulse for fitting is convenient but not necessary, as this does not affect the final fit result.

Solving the integrals:

$$\mathscr{F}[U_{SST}(t)](f) = A\left[\frac{\tau_+}{1 + i2\pi f\tau_+} - \frac{\tau_-}{1 + i2\pi f\tau_-}\right]$$

$$\mathscr{F}[U_{SST}(t)](f) = A\left[\frac{\tau_+(1 - i2\pi f\tau_+)}{1 + (2\pi f\tau_+)^2} - \frac{\tau_-(1 - i2\pi f\tau_-)}{1 + (2\pi f\tau_-)^2}\right]$$

$$\mathscr{F}[U_{SST}(t)](f) = A\left[\frac{Q}{(1 + (2\pi f\tau_+)^2)(1 + (2\pi f\tau_-)^2)}\right]$$

where

$$\begin{aligned}
Q &= \tau_+\left(1 + (2\pi f\tau_-)^2\right) - i2\pi f\tau_+^2\left(1 + (2\pi f\tau_-)^2\right) - \tau_-\left(1 + (2\pi f\tau_+)^2\right) + i2\pi f\tau_-^2\left(1 + (2\pi f\tau_+)^2\right) \\
&= \tau_+ + (2\pi f)^2\tau_-\tau_+\tau_- - \tau_- - (2\pi f)^2\tau_-\tau_+\tau_+ - i2\pi f\tau_+^2\left(1 + \cancel{(2\pi f\tau_-)^2}\right) + i2\pi f\tau_-^2\left(1 + \cancel{(2\pi f\tau_+)^2}\right) \\
&= (\tau_+ - \tau_-)(1 - (2\pi f)^2\tau_+\tau_-) - i2\pi f(\tau_+ + \tau_-)(\tau_+ - \tau_-) \\
&= (\tau_+ - \tau_-)\left((1 - (2\pi f)^2\tau_+\tau_-) - i2\pi f(\tau_+ + \tau_-)\right)
\end{aligned}$$

Then

$$\mathscr{F}[U_{SST}(t)](f) = -A(\tau_- - \tau_+)\frac{[1 - (2\pi f)^2\tau_+\tau_-] - i2\pi f(\tau_+ + \tau_-)}{[1 + \tau_+^2(2\pi f)^2][1 + \tau_-^2(2\pi f)^2]}$$

Finally, from the time-shifting property of the Fourier transform:

$$\mathscr{F}[g(t - t_0)](f) = \mathscr{F}[g(t)](f)\exp\{-2\pi f i t_0\}$$

Therefore if $t_0 \neq 0$ in Eq. 6.1, then:

$$\mathscr{F}[U_{SST}(t)](f) = -A(\tau_- - \tau_+)\frac{[1 - (2\pi f)^2\tau_+\tau_-] - i2\pi f(\tau_+ + \tau_-)}{[1 + \tau_+^2(2\pi f)^2][1 + \tau_-^2(2\pi f)^2]}\exp\{-2\pi f i t_0\}$$

□

APPENDIX

B

ENERGY RESOLUTION WITH LOWER SIMULATED NOISE

Two simulation runs were performed to evaluate the contribution of the low and high frequencies to the noise.

First, one of the noise components in Fig. 5.7 was removed to evaluate the contribution of the low-frequency noise. The removed noise component was the fourth-order low-pass filter noise with parameters $\sigma = 14.6$ mV and $f_c = 66.6$ kHz. The PSD of the simulated noise is shown in Fig. B.1. Although the resultant simulated TES pulse in Fig. B.2a is very similar to the one in Fig. 5.9a, however the energy resolution computed from a sample of 1000 pulses corresponds to 8.6 %.

Secondly, the contribution of the high-frequency noise is evaluated by removing it from the noise production process. For this, only one fourth-order low-pass filter noise with parameters $\sigma = 25.1$ mV and $f_c = 66.6$ kHz is used. The PSD of the simulated noise is shown in Fig. B.3. The simulated TES pulse in Fig. B.4a lacks high-frequency noise in Fig. 5.9a, and the energy resolution computed from a sample of 1000 pulses corresponds to 10.6 %.

From the two simulations, it can be concluded that the low-frequency part of the PSD exerts the most significant influence on the energy resolution computed from the pulse integral. The drastic reduction of the high-frequency part of the spectrum in Fig. B.3 only reduces the energy resolution by 4 %. In comparison, a relatively small reduction of the low frequency part of the spectrum in Fig. B.1, reduces the energy resolution by 22 %.

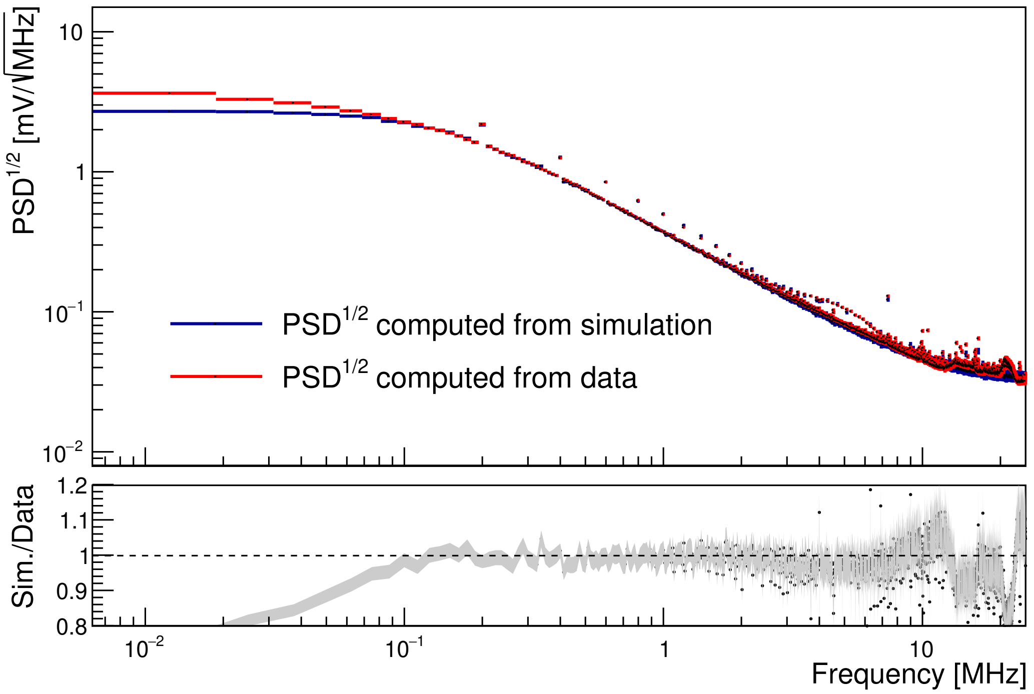

Figure B.1: Comparison of the PSD of simulated and measured noises. The lower plot shows the ratio between the PSDs with the PSD of the measured noise in the denominator with its corresponding uncertainty. The PSD of the simulated noise is lower than the data at frequencies lower than 100 kHz.

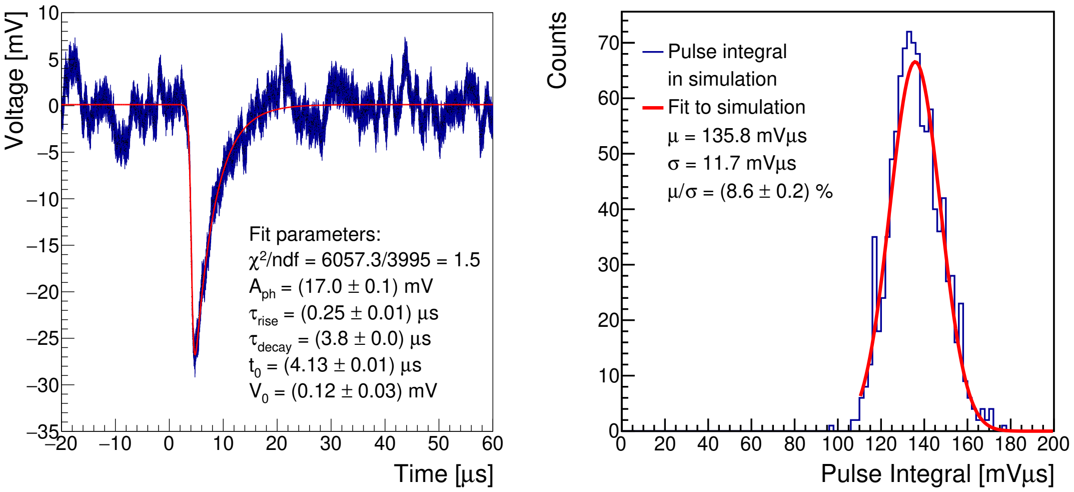

(a) (b)

Figure B.2: (a) Simulated 1064 nm pulse fitted to the phenomenological model and parameters obtained from the fitting procedure, (b) pulse integral distribution of simulated 1064 nm photons and Gaussian function fitted to the distribution. The energy resolution is calculated from the Gaussian function's mean and sigma, resulting in (8.6 ± 0.2)%.

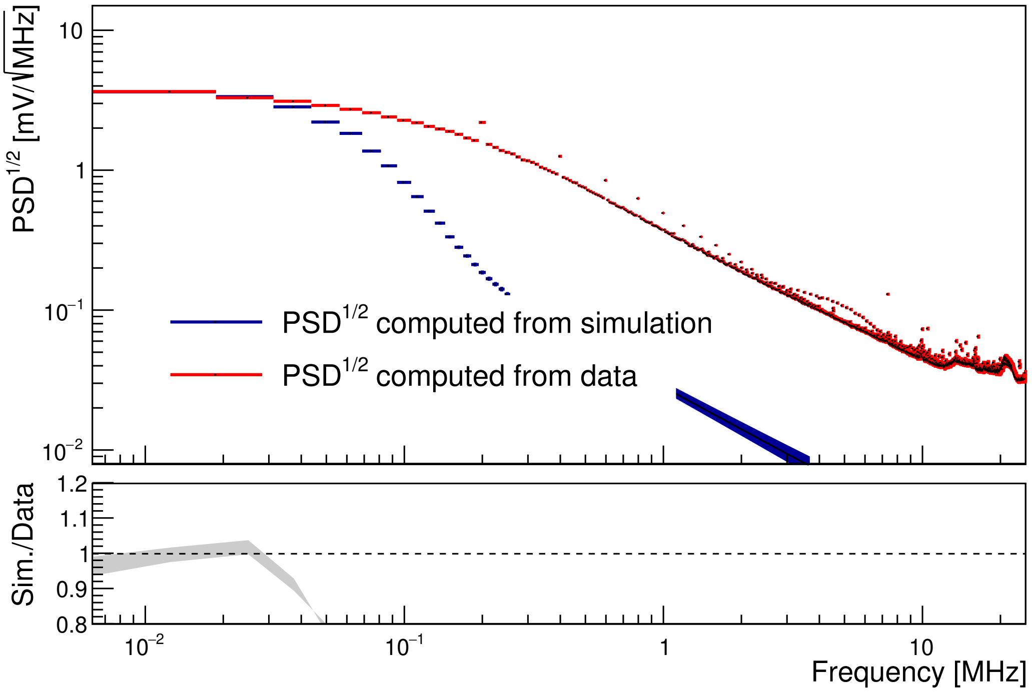

Figure B.3: Comparison of the PSD of simulated and measured noises. The lower plot shows the ratio between the PSDs with the PSD of the measured noise in the denominator with its corresponding uncertainty. The PSD of the simulated noise is much lower than the data at frequencies higher than 100 kHz.

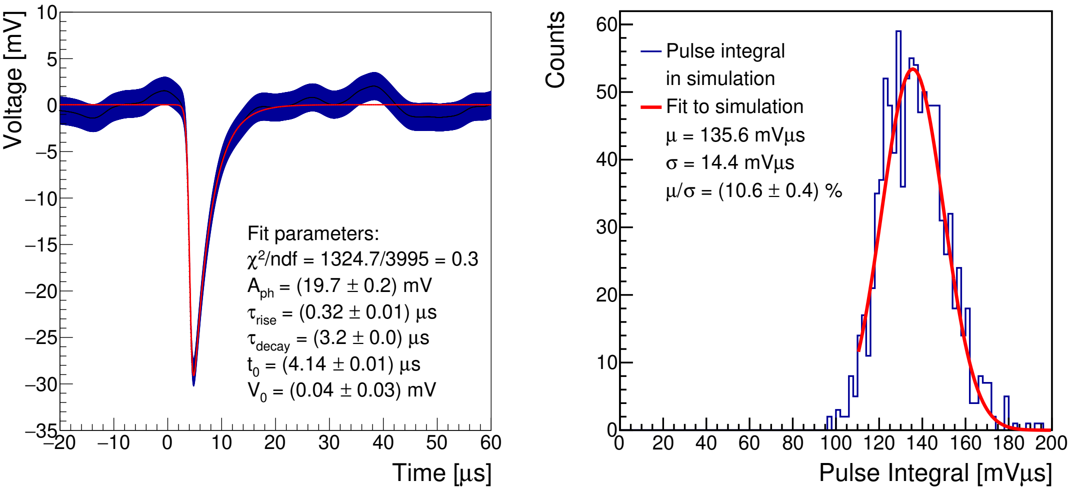

(a) (b)

Figure B.4: (a) Simulated 1064 nm pulse fitted to the phenomenological model and parameters obtained from the fitting procedure, (b) pulse integral distribution of simulated 1064 nm photons and Gaussian function fitted to the distribution. The energy resolution is calculated from the Gaussian function's mean and sigma, resulting in (10.6 ± 0.2)%.

APPENDIX

C

CUT ANALYSIS IN EXTRINSICS DATA

For the extrinsic background distribution in chapter 4, and analogously to work previously performed within the TES group [43], cuts were imposed in the rise and decay times of the pulses and the reduced χ^2 from the fitting procedure based on the time domain. These parameters were chosen given that they should not depend on the energy of the arriving photon. The cuts were performed on the interval $[-3\sigma, 3\sigma]$ to keep the acceptance of 1064 nm photons high. In Fig. C.1a, C.1c, and C.1e, the distributions of rise time, decay time and reduced chi-squared for 1064 nm photons, and the corresponding cuts, can be seen. This results in an acceptance of 99.2 %. The cuts are then applied to the results of the analysis of the extrinsics dataset. With this, the background rate drops from $4.4 \cdot 10^{-2}$ cps to $1.8 \cdot 10^{-2}$ cps.

For the extrinsic background distribution in chapter 6, in addition to the cuts in the time domain, cuts were imposed in the rise and decay times of the pulses and the reduced χ^2 from the fitting procedure based on the frequency domain. The cuts were also performed on the interval $[-3\sigma, 3\sigma]$. In Fig. C.1b, C.1d, and C.1f, the distributions of rise time, decay time and reduced chi-squared for 1064 nm photons, and the corresponding cuts, can be seen. The acceptance is then 98.4 % for the cuts in the six distributions of 1064 nm photon parameters. The additional cuts are applied to the results of the analysis of the extrinsics dataset, resulting in a reduction of the background rate to $1.5 \cdot 10^{-2}$ cps.

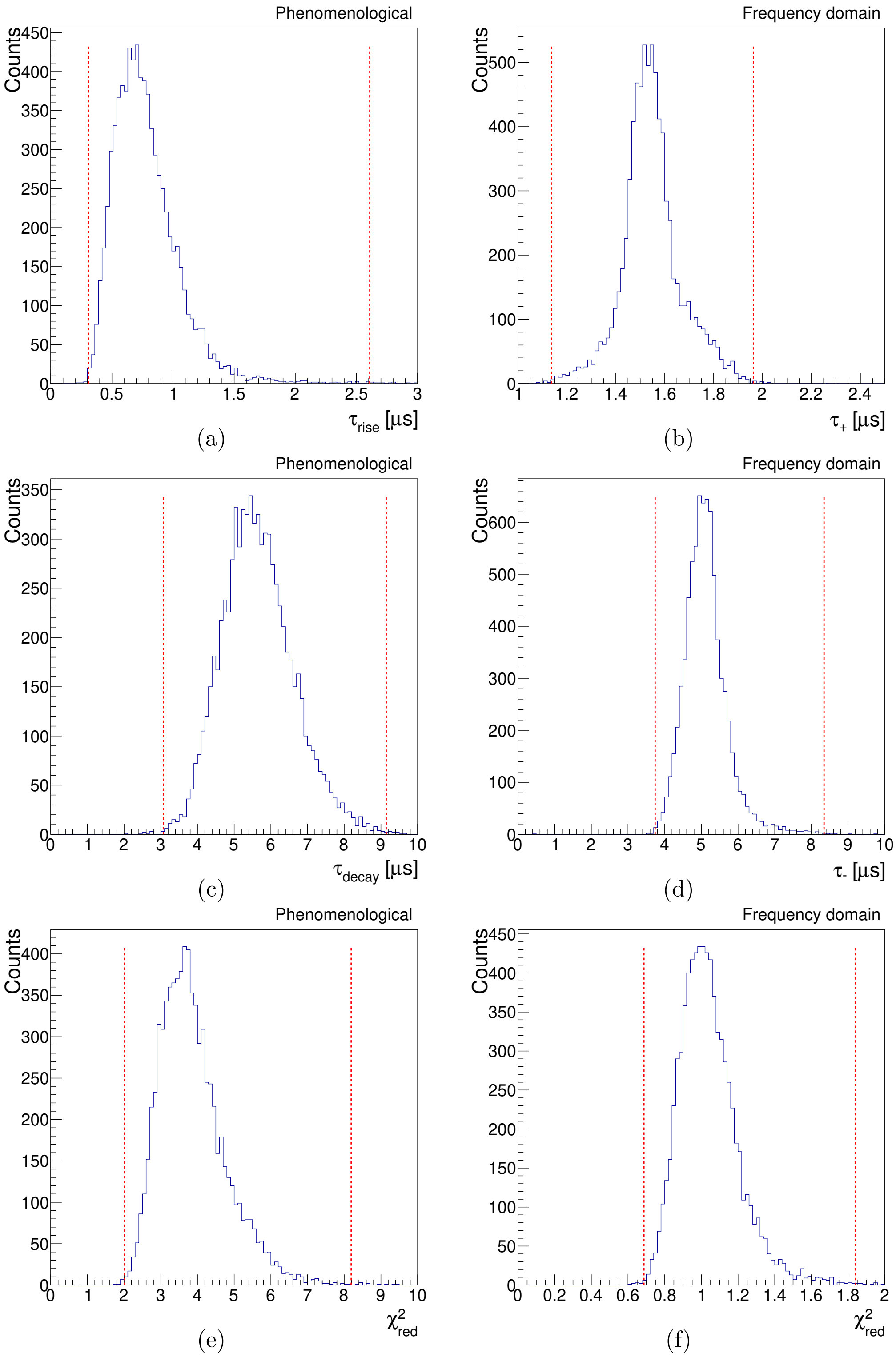

(a) (b) (c) (d) (e) (f)

Figure C.1: Distribution of parameters obtained by fitting the phenomenological model in a, c and e, and the frequency domain SST model in b, d and f, to measured 1064 nm pulses. The cuts (dashed red lines) exclude the pulses that lie outside the $[-3\sigma, 3\sigma]$ region of the parameters: (a) τ_{rise}, (c) τ_{decay} and (e) χ^2_{red} in the time domain, and (b) τ_+, (c) τ_- and (e) χ^2_{red} in the frequency domain.

APPENDIX

D

ALAZARGUI UPGRADE

This section describes the upgrades implemented in the AlazarGui, the software which controls the Alazar DAQ card, within this thesis. The main goal of the upgrade was to add the possibility of taking data using the two input channels of the card at the same time, in contrast to only one channel, which was the previous configuration. This was implemented with a trigger system with an OR logic, i.e. if one channel triggers, the information in both channels is recorded. This was done with the idea of looking for coincidence events when operating two TESs.

In addition, other features were implemented, listed below:

- The possibility of multi-core triggering in the acquired data allowed a boost in the processing of the data in the pseudo-triggered mode.
- Another optimization in the data processing was performed by reordering the operations while saving the triggered data. Before, the raw data was converted to the format used in the ROOT file and then placed in a queue which manages the data recording. The triggering cannot be performed until the data is placed in the queue. If the conversion happens after the raw data is placed in the queue, the trigger's wait time is greatly reduced.
- Before the upgrade, a trigger rate high enough to saturate the card's memory produced a crash in the AlazarGui. Even when taking data at low rates, the SQUID readout could suffer external interference and produce fluctuation that would trigger at a high rate for a short time, therefore crashing the DAQ system. These events are rare but can happen during a data taking time of several days. This was solved by implementing a dead time where the software stops triggering until the card is not saturated.
- As mentioned in section 6.3, the possibility of triggering on filtered samples was added. This would reduce the amount of data taken due to triggering high-frequency fluctua-

tions, such as the produced by the 200 kHz noise when the SQUID readout is configured to a high GBWP.

- The possibility of saving metadata in the ROOT file of the acquired data was added. It records the parameters present in the "Take data" section shown in Fig. D.1b as metadata.

The implementation of all the features also required the modification of the AlazarGui interface. Fig. D.1 shows the interface before and after the upgrade.

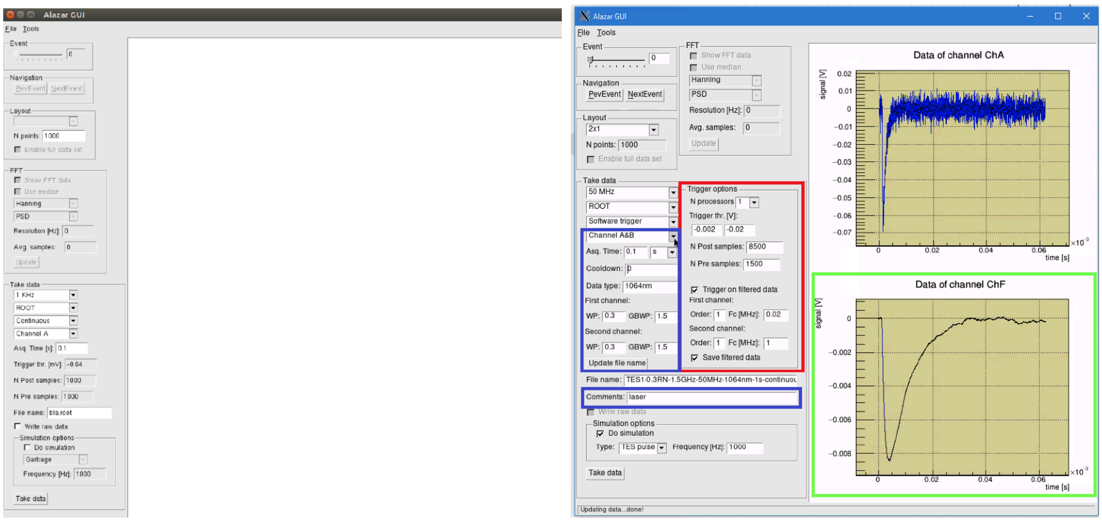

Event: 0
Layout:
N points: 1000
☐ Enable full data set
FFT:
☐ Show FFT data
☐ Use median
Hanning
PSD
Resolution [Hz]: 0
Avg. samples: 0
Take data:
1 KHz
ROOT
Continuous
Channel A
Asq. Time [s]: 0.1
Trigger thr. [mV]: -0.04
N Post samples: 1000
N Pre samples: 1000
File name: bla.root
☐ Write raw data
Simulation options:
☐ Do simulation
Garbage
Frequency [Hz]: 1000

Event: 0
Layout: 2x1
N points: 1000
☐ Enable full data set
FFT:
☐ Show FFT data
☐ Use median
Hanning
PSD
Resolution [Hz]: 0
Avg. samples: 0
Take data:
50 MHz
ROOT
Software trigger
Channel A&B
Asq. Time: 0.1 s
Cooldown: 0
Data type: 1064nm
First channel:
WP: 0.3 GBWP: 1.5
Second channel:
WP: 0.3 GBWP: 1.5
Trigger options:
N processors 1
Trigger thr. [V]:
-0.002 -0.02
N Post samples: 8500
N Pre samples: 1500
☑ Trigger on filtered data
First channel:
Order: 1 Fc [MHz]: 0.02
Second channel:
Order: 1 Fc [MHz]: 1
☑ Save filtered data
File name: TES1-0.3RN-1.5GHz-50MHz-1064nm-1s-continuou
Comments: laser
☐ Write raw data
Simulation options:
☑ Do simulation
Type: TES pulse Frequency [Hz]: 1000
Updating data...done!

(a) (b)

Figure D.1: AlazarGui interface (a) before and (b) after the upgrade. The section inside the blue boxes shows the new data which can be saved in the file. This includes the information on the cooldown corresponding to the data taking, a short description of the measurement setup, and the SQUIDs and the TES working parameters. The section inside the red box shows the new parameters to configure the triggers in the pseudo-triggered mode. The pulse inside the green box corresponds to the filtered samples used for triggering while avoiding high-frequency fluctuations.

APPENDIX

E

LIST OF ACRONYMS

ALP axion-like particle

ALPS Any Light Particle Search

BBR Black Body Radiation

CP charge parity

DAQ Data Acquisition

DESY Deutsches Elektronen-Synchrotron

DFSZ Dine-Fischler-Srednicki-Zhitnitsky

ETF Electrothermal feedback

FFT Fast Fourier Transform

FLL flux-locked loop

FWHM Full Width Half at Maximum

GBWP Gain Bandwidth Product

GELB-TES Geant4-based Events from Low Backgrounds in a Transition Edge Sensor

HERA Hadron-Elektron-Ring-Anlage

HPF high-pass filter

KSVZ Kim-Shifman-Vainshtein-Zakharov

LPF low-pass filter

LSW light shining through a wall

LTI Linear Time-Invariant

NIST National Institute of Standards and Technology

PSD power spectral density

PTB Physikalisch-Technische Bundesanstalt

QCD quantum chromodynamics

SNSPD superconducting nanowire single-photon detector

SQUID Superconducting Quantum Interference Device

SST Small Signal Theory

TES Transition Edge Sensor

TESPASS TES pulse analysis and signal simulation

TFN thermal fluctuation noise

WGN white Gaussian noise

WP working point

BIBLIOGRAPHY

[1] Planck Collaboration, "Planck 2018 results - VI. Cosmological parameters", *AA* **641** (2020) A6, `doi:10.1051/0004-6361/201833910`. 1

[2] E. Corbelli and P. Salucci, "The extended rotation curve and the dark matter halo of M33", *Monthly Notices of the Royal Astronomical Society* **311** (01, 2000) 441–447, `doi:10.1046/j.1365-8711.2000.03075.x`. 1

[3] A. Amruth et al., "Einstein rings modulated by wavelike dark matter from anomalies in gravitationally lensed images", `doi:10.1038/s41550-023-01943-9`. 1

[4] R. D. Peccei and H. R. Quinn, "Constraints imposed by CP conservation in the presence of pseudoparticles", *Phys. Rev. D* **16** (Sep, 1977) 1791–1797, `doi:10.1103/PhysRevD.16.1791`. 1, 3

[5] S. Weinberg, "A New Light Boson?", *Phys. Rev. Lett.* **40** (Jan, 1978) 223–226, `doi:10.1103/PhysRevLett.40.223`. 1, 92

[6] T. W. Donnelly et al., "Do axions exist?", *Phys. Rev. D* **18** (Sep, 1978) 1607–1620, `doi:10.1103/PhysRevD.18.1607`. 1

[7] M. A. Shifman, A. I. Vainshtein, and V. I. Zakharov, "Can Confinement Ensure Natural CP Invariance of Strong Interactions?", *Nucl. Phys. B* **166** (1980) 493–506, `doi:10.1016/0550-3213(80)90209-6`. 2, 3

[8] M. Dine, W. Fischler, and M. Srednicki, "A simple solution to the strong CP problem with a harmless axion", *Physics Letters B* **104** (1981), no. 3, 199–202, `doi:10.1016/0370-2693(81)90590-6`. 2, 3

[9] F. Chadha-Day, J. Ellis, and D. J. E. Marsh, "Axion dark matter: What is it and why now?", *Science Advances* **8** (2022), no. 8, eabj3618, `doi:10.1126/sciadv.abj3618`, `arXiv:https://www.science.org/doi/pdf/10.1126/sciadv.abj3618`. 2, 4, 92

[10] A. Ringwald, “Axions and Axion-Like Particles”, `arXiv:1407.0546`. 2, 3

[11] R. Shah, “A TES detector for ALPS II”. PhD thesis, Johannes Gutenberg-Universität Mainz, 2022. `doi:10.25358/OPENSCIENCE-8558`. 2, 17, 19, 20, 23, 24, 28, 59, 77

[12] R. D. Peccei and H. R. Quinn, “CP Conservation in the Presence of Pseudoparticles”, *Phys. Rev. Lett.* **38** (Jun, 1977) 1440–1443, `doi:10.1103/PhysRevLett.38.1440`. 3

[13] S. Dar, “The Neutron EDM in the SM: A Review”, `arXiv:hep-ph/0008248`. 3

[14] C. Abel et al., “Measurement of the Permanent Electric Dipole Moment of the Neutron”, *Phys. Rev. Lett.* **124** (Feb, 2020) 081803, `doi:10.1103/PhysRevLett.124.081803`. 3

[15] F. Wilczek, “Problem of Strong P and T Invariance in the Presence of Instantons”, *Phys. Rev. Lett.* **40** (Jan, 1978) 279–282, `doi:10.1103/PhysRevLett.40.279`. 3

[16] A. V. Sokolov and A. Ringwald, “Photophilic hadronic axion from heavy magnetic monopoles”, *Journal of High Energy Physics* **2021** (Jun, 2021) `doi:10.1007/jhep06(2021)123`. 3, 8

[17] L. Di Luzio, M. Giannotti, E. Nardi, and L. Visinelli, “The landscape of QCD axion models”, *Physics Reports* **870** (2020) 1–117, `doi:10.1016/j.physrep.2020.06.002`. The landscape of QCD axion models. 3, 4

[18] M. Cicoli, M. D. Goodsell, and A. Ringwald, “The type IIB string axiverse and its low-energy phenomenology”, `doi:10.1007/JHEP10(2012)146`. 3

[19] J. E. Kim and G. Carosi, “Axions and the strong CP problem”, *Rev. Mod. Phys.* **82** (Mar, 2010) 557–601, `doi:10.1103/RevModPhys.82.557`. 4

[20] L. Di Luzio et al., “Stellar evolution confronts axion models”, *Journal of Cosmology and Astroparticle Physics* **2022** (February, 2022) 035, `doi:10.1088/1475-7516/2022/02/035`. 4, 92

[21] M. Meyer, D. Horns, and M. Raue, “First lower limits on the photon-axion-like particle coupling from very high energy gamma-ray observations”, *Phys. Rev. D* **87** (Feb, 2013) 035027, `doi:10.1103/PhysRevD.87.035027`. 4, 8

[22] Q. Yu, “Searching for signals of photon-ALP mixing effects with gamma-ray spectra of AGNs”. PhD thesis, U. Hamburg (main), 2023. 4

[23] P. Sikivie, “Experimental Tests of the "Invisible" Axion”, *Phys. Rev. Lett.* **51** (Oct, 1983) 1415–1417, `doi:10.1103/PhysRevLett.51.1415`. 4

[24] A. A. Anselm, “Arion ↔ Photon Oscillations in a Steady Magnetic Field. (In Russian)”, *Yad. Fiz.* **42** (1985) 1480–1483. 4

[25] K. Van Bibber et al., “Proposed experiment to produce and detect light pseudoscalars”, *Phys. Rev. Lett.* **59** (Aug, 1987) 759–762, `doi:10.1103/PhysRevLett.59.759`. 4

[26] C. O'Hare, "cajohare/AxionLimits: AxionLimits". `https://cajohare.github.io/AxionLimits/`, July, 2020. `doi:10.5281/zenodo.3932430`. 5

[27] P. Arias, J. Jaeckel, J. Redondo, and A. Ringwald, "Optimizing light-shining-through-a-wall experiments for axion and other weakly interacting slim particle searches", *Phys. Rev. D* **82** (Dec, 2010) 115018, `doi:10.1103/PhysRevD.82.115018`. 4

[28] R. Bähre et al., "Any light particle search II Technical Design Report", *Journal of Instrumentation* **8** (Sep, 2013) T09001T09001, `doi:10.1088/1748-0221/8/09/t09001`. 7, 8, 9, 76, 92

[29] T. C. Kozlowski, "Characterization and Control of Optical Cavities Towards a First Science Run of the ALPS II Experiment". PhD thesis, Florida U., Florida U., 2022. 7

[30] A. Ringwald, "Production and detection of very light bosons in the HERA tunnel", *Physics Letters B* **569** (Sep, 2003) 5156, `doi:10.1016/j.physletb.2003.07.015`. 7

[31] ALPS II Collaboration, "Axion and ALP search with the Any Light Particle Search II experiment at DESY", *PoS* **EPS-HEP2023** (2024) 117, `doi:10.22323/1.449.0117`. 7, 8

[32] F. Hoogeveen and T. Ziegenhagen, "Production and detection of light bosons using optical resonators", *Nuclear Physics B* **358** (1991), no. 1, 3–26, `doi:https://doi.org/10.1016/0550-3213(91)90528-6`. 8

[33] M. D. Ortiz et al., "Design of the ALPS II optical system", *Phys. Dark Univ.* **35** (2022) 100968, `doi:10.1016/j.dark.2022.100968`, `arXiv:2009.14294`. 8

[34] I. G. Irastorza and J. Redondo, "New experimental approaches in the search for axion-like particles", *Progress in Particle and Nuclear Physics* **102** (Sep, 2018) 89159, `doi:10.1016/j.ppnp.2018.05.003`. 8

[35] OSQAR Collaboration, "New exclusion limits on scalar and pseudoscalar axionlike particles from light shining through a wall", *Phys. Rev. D* **92** (2015), no. 9, 092002, `doi:10.1103/PhysRevD.92.092002`, `arXiv:1506.08082`. 8

[36] I. G. Irastorza et al., eds., "Proceedings, 11th Patras Workshop on Axions, WIMPs and WISPs (Axion-WIMP 2015)", DESY-PROC, 11th Patras Workshop on Axions, WIMPs and WISPs, Zaragoza (Spain), 22 Jun 2015 - 26 Jun 2015. Verlag Deutsches Elektronen-Synchrotron, Hamburg, (Jun, 2015). `doi:10.3204/DESY-PROC-2015-02`. 8

[37] ALPS II Collaboration, "Approaching the first any light particle search II science run", *SciPost Phys. Proc.* **12** (2023) 039, `doi:10.21468/SciPostPhysProc.12.039`. 8

[38] A. Hallal et al., "The heterodyne sensing system for the ALPS II search for sub-eV weakly interacting particles", *Physics of the Dark Universe* **35** (Mar, 2022) 100914, `doi:10.1016/j.dark.2021.100914`. 8

[39] K.-S. Isleif, “The Any Light Particle Search experiment at DESY”, `arXiv:2202.07306`. 8

[40] Z. R. Bush et al., “Coherent detection of ultraweak electromagnetic fields”, *Phys. Rev. D* **99** (Jan, 2019) 022001, `doi:10.1103/PhysRevD.99.022001`. 8, 9

[41] K. Irwin and G. Hilton, “Transition-Edge Sensors”, pp. 63–150. Springer Berlin Heidelberg, Berlin, Heidelberg, 2005. `doi:10.1007/10933596_3`. 9, 10, 15, 92

[42] A. Lita, A. Miller, and S. Nam, “Counting near-infrared single-photons with 95% efficiency”, *Optics express* **16** (04, 2008) 3032–40, `doi:10.1364/OE.16.003032`. 9, 45

[43] R. Shah et al., “TES Detector for ALPS II”, *Proceedings of The European Physical Society Conference on High Energy Physics PoS(EPS-HEP2021)* (Jan, 2022) `doi:10.22323/1.398.0801`. 9, 55, 59, 78, 104

[44] M. A. Lindeman, “Microcalorimetry and the transition-edge sensor”. PhD thesis, University of California, Davis, 4, 2000. `doi:10.2172/15009469`. 13

[45] M. A. Lindeman et al., “Impedance measurements and modeling of a transition-edge-sensor calorimeter”, *Review of Scientific Instruments* **75** (05, 2004) 1283–1289, `doi:10.1063/1.1711144`. 14, 15, 26, 28

[46] K. Hattori, R. Kobayashi, S. Takasu, and D. Fukuda, “Complex impedance of a transition-edge sensor with sub-s time constant”, *AIP Advances* **10** (03, 2020) 035004, `doi:10.1063/1.5127100`. 14

[47] D. McCammon, “Thermal Equilibrium Calorimeters An Introduction”, p. 134. Springer Berlin Heidelberg, July, 2005. `doi:10.1007/10933596_1`. 16

[48] A. Lita et al., “Tuning of tungsten thin film superconducting transition temperature for fabrication of photon number resolving detectors”, *IEEE Transactions on Applied Superconductivity* **15** (2005), no. 2, 3528–3531, `doi:10.1109/TASC.2005.849033`. 16, 28

[49] F. Pobell, “Matter and methods at low temperatures”, Springer, 3rd rev. and expanded edition, 2007, ISBN 978-3-5404-6360-3. 17

[50] J. Clarke and A. Braginski, “The SQUID Handbook”, pp. i–xvi. John Wiley Sons, Ltd, 2004. `doi:3527603646.fmatter`. 18

[51] J. Dreyling-Eschweiler, “A superconducting microcalorimeter for low-flux detection of near-infrared single photons”. Dr., University of Hamburg, Hamburg, 2014. University of Hamburg, Diss., 2014. `doi:10.3204/DESY-THESIS-2014-016`. 19, 20, 23, 28, 46

[52] D. Drung, “Advanced SQUID Read-Out Electronics”, Springer Netherlands, Dordrecht, 1996, ISBN 978-9-4011-5674-5. 19

[53] C. Weinsheimer, “Light-Shining-through-a-Wall: Searching for Axion-Like Particles with the OSQAR and ALPS II experiment”. PhD thesis, Mainz U., 2018. `doi:10.25358/openscience-2629`. 20

[54] R. Brun and F. Rademakers, “ROOT An object oriented data analysis framework”, *Nuclear Instruments and Methods in Physics Research Section A: Accelerators, Spectrometers, Detectors and Associated Equipment* **389** no. 1, 81–86, `doi:10.1016/S0168-9002(97)00048-X`. 20, 59, 70, 93

[55] M. López et al., “Single-Photon Avalanche Detector Calibration at PTB”, in *2018 Conference on Precision Electromagnetic Measurements (CPEM 2018)*, pp. 1–2. 2018. `doi:10.1109/CPEM.2018.8500968`. 22

[56] J. A. Rubiera Gimeno et al., “A TES system for ALPS II - Status and Prospects”, *PoS* **EPS-HEP2023** (2023) 567, `doi:10.22323/1.449.0567`. 22, 69, 77

[57] COMSOL AB, “COMSOL Multiphysics® v. 6.2”. www.comsol.com, 2023. 23, 25, 33

[58] S. Agostinelli and et.al., “Geant4a simulation toolkit”, *Nuclear Instruments and Methods in Physics Research Section A: Accelerators, Spectrometers, Detectors and Associated Equipment* **506** (2003), no. 3, 250–303, `doi:10.1016/S0168-9002(03)01368-8`. 23, 35

[59] M. Meyer et al., “A first application of machine and deep learning for background rejection in the ALPS II TES detector”, `doi:10.1002/andp.202200545`, `arXiv:2304.08406`. 24, 78

[60] J. Dreyling-Eschweiler et al., “Characterization, 1064 nm photon signals and background events of a tungsten TES detector for the ALPS experiment”, *Journal of Modern Optics* **62** (2015), no. 14, 1132–1140, `doi:10.1080/09500340.2015.1021723`. 24, 25

[61] N. Bastidon and D. Horns, “Radioactivity induced dark count rate for single near-infrared photon detection with a tungsten transition edge sensor at 80 mK”, `arXiv:2206.14654`. 25

[62] M. Tinkham, “Introduction to superconductivity”, Dover books on physics, Dover Publ, Mineola, NY, 2nd edition, 2015, ISBN 978-0-4864-3503-9. 26, 27

[63] C. Kittel, “Introduction to solid state physics”, Wiley, Hoboken, NJ, 8th ed edition, 2005, ISBN 978-0-4714-1526-8. 26, 27

[64] G. R. Stewart, “Measurement of low-temperature specific heat”, *Review of Scientific Instruments* **54** (01, 1983) 1–11, `doi:10.1063/1.1137207`. 26, 27

[65] B. Cabrera, “Introduction to TES Physics”, *Journal of Low Temperature Physics* **151** (April, 2008) 82–93, `doi:10.1007/s10909-007-9632-2`. 26, 27

[66] A. Lita. Personal communication, 2023. National Institute of Standards and Technology, USA. 27

[67] G. Masetti, M. Severi, and S. Solmi, “Modeling of carrier mobility against carrier concentration in arsenic-, phosphorus-, and boron-doped silicon”, *IEEE Transactions on Electron Devices* **30** (July, 1983) 764–769, `doi:10.1109/t-ed.1983.21207`. 27

[68] C. J. Glassbrenner and G. A. Slack, “Thermal Conductivity of Silicon and Germanium from 3°K to the Melting Point”, *Phys. Rev.* **134** (May, 1964) A1058–A1069, `doi:10.1103/PhysRev.134.A1058`. 27

[69] H. M. Rosenberg, “The Thermal Conductivity of Germanium and Silicon at Low Temperatures”, *Proceedings of the Physical Society. Section A* **67** (sep, 1954) 837, `doi:10.1088/0370-1298/67/9/312`. 27

[70] J. Thompson and B. Younglove, “Thermal conductivity of silicon at low temperatures”, *Journal of Physics and Chemistry of Solids* **20** (1961), no. 1, 146–149, `doi:10.1016/0022-3697(61)90146-9`. 27, 33

[71] A. McConnell and K. Goodson, “Thermal conduction in silicon micro-and nanostructures”, *Annual review of heat transfer* **14** (01, 2005) `doi:10.1615/AnnualRevHeatTransfer.v14.120`. 27

[72] L. Salerno, P. Kittel, and A. Spivak, “Thermal conductance of pressed metallic contacts augmented with indium foil or Apiezon grease at liquid helium temperatures”, *Cryogenics* **34** (1994), no. 8, 649–654, `doi:10.1016/0011-2275(94)90142-2`. 27

[73] A. Lita, A. Miller, and S. Nam, “Energy Collection Efficiency of Tungsten Transition-Edge Sensors in the Near-Infrared”, *Journal of Low Temperature Physics* **151** (04, 2008) 125–130, `doi:10.1007/s10909-007-9627-z`. 30

[74] B. Cabrera et al., “Detection of single infrared, optical, and ultraviolet photons using superconducting transition edge sensors”, *Applied Physics Letters* **73** (08, 1998) 735–737, `doi:10.1063/1.121984`. 30, 77

[75] A. Majumdar, “Microscale Heat Conduction in Dielectric Thin Films”, *Journal of Heat Transfer* **115** (02, 1993) 7–16, `doi:10.1115/1.2910673`. 33

[76] A. T. Ramu and Y. Ma, “An enhanced Fourier law derivable from the Boltzmann transport equation and a sample application in determining the mean-free path of nondiffusive phonon modes”, *Journal of Applied Physics* **116** (09, 2014) 093501, `doi:10.1063/1.4894087`. 33

[77] M. Kelsey and et.al., “G4CMP: Condensed matter physics simulation using the Geant4 toolkit”, *Nuclear Instruments and Methods in Physics Research Section A: Accelerators, Spectrometers, Detectors and Associated Equipment* **1055** (2023) 168473, `doi:j.nima.2023.168473`. 33

[78] A. J. Miller et al., “Compact cryogenic self-aligning fiber-to-detector coupling with losses below one percent”, *Opt. Express* **19** (May, 2011) 9102–9110, `doi:10.1364/OE.19.009102`. 36

[79] P. Shukla and S. Sankrith, “Energy and angular distributions of atmospheric muons at the Earth”, `arXiv:1606.06907`. 36

[80] Particle Data Group Collaboration, “Review of Particle Physics”, *Phys. Rev. D* **98** (Aug, 2018) `doi:10.1103/PhysRevD.98.030001`. 36

[81] “Radiation protection and norm residue management in the zircon and zirconia industries”,. Includes bibliographical references. 37, 38

[82] M. Chapellier, “Physics of electrons and phonons in low-temperature detectors”, *Nuclear Instruments and Methods in Physics Research Section A: Accelerators, Spectrometers, Detectors and Associated Equipment* **520** (2004), no. 1, 21–26, `doi:10.1016/j.nima.2003.11.211`. Proceedings of the 10th International Workshop on Low Temperature Detectors. 38

[83] R. Leadon and J. A. Naber, “Recombination Lifetimes in HighPurity Silicon at Low Temperatures”, *Journal of Applied Physics* **40** (05, 1969) 2633–2638, `doi:10.1063/1.1658046`. 38

[84] C. Schwemmbauer et al., “Direct dark matter searches using ALPS II’s TES detection system”, in *Proceedings of The European Physical Society Conference on High Energy Physics — PoS(EPS-HEP2023)*, volume 449, p. 120. 2024. `doi:10.22323/1.449.0120`. 41, 85, 94

[85] A. Lita, A. Miller, and S. Nam, “Energy Collection Efficiency of Tungsten Transition-Edge Sensors in the Near-Infrared”, *Journal of Low Temperature Physics* **151** (04, 2008) 125–130, `doi:10.1007/s10909-007-9627-z`. 42, 94

[86] A. J. Miller et al., “Superconducting photon number resolving detectors: Performance and promise”, in *Proc. 8th Int. Conf. Quantum Communication, Measurement and Computing (QCMC06)*, pp. 445–450. 2007. 43, 48, 93

[87] W. Greiner, L. Neise, and H. Stöcker, “Thermodynamics and statistical mechanics”, Classical theoretical physics, Springer, 1995, ISBN 978-1-4612-0827-3. 44

[88] C. Kittel and H. Kroemer, “Thermal physics”, W. H. Freeman, 2nd edition, 1980, ISBN 978-0-7167-1088-2. 44

[89] H. O. McMahon, “Thermal Radiation from Partially Transparent Reflecting Bodies”, *J. Opt. Soc. Am.* **40** (Jun, 1950) 376–380, `doi:10.1364/JOSA.40.000376`. 44

[90] A. E. Lita et al., “Superconducting transition-edge sensors optimized for high-efficiency photon-number resolving detectors”, in *Advanced Photon Counting Techniques IV*, M. A. Itzler and J. C. Campbell, eds., volume 7681, p. 76810D, International Society for Optics and Photonics. SPIE, 2010. `doi:10.1117/12.852221`. 45, 53

[91] M. A. Arshad, A. Hartung, and M. Jäger, “A stimulated Stokes Raman scattering-based approach for continuous wave supercontinuum generation in optical fibers”, *Laser Physics Letters* **16** (03, 2019) 035108, `doi:10.1088/1612-202X/aaff53`. 47

[92] D. Marcuse, “Influence of curvature on the losses of doubly clad fibers”, *Appl. Opt.* **21** (Dec, 1982) 4208–4213, `doi:10.1364/AO.21.004208`. 48

[93] K. Smirnov et al., "Dependence of dark count rates in superconducting single photon detectors on the filtering effect of standard single mode optical fibers", *Applied Physics Express* **8** (Jan, 2015) 022501, `doi:10.7567/APEX.8.022501`. 48

[94] C. Eckart and F. R. Shonka, "Accidental Coincidences in Counter Circuits", *Phys. Rev.* **53** (May, 1938) 752–756, `doi:10.1103/PhysRev.53.752`. 53

[95] J. A. Rubiera Gimeno et al., "The TES detector of the ALPS II experiment", *Nuclear Instruments and Methods in Physics Research Section A: Accelerators, Spectrometers, Detectors and Associated Equipment* **1046** (January, 2023) 167588, `doi:10.1016/j.nima.2022.167588`. 58, 63

[96] R. Shah et al., "Characterising a Single-Photon Detector for ALPS II", *Journal of Low Temperature Physics* **209** (November, 2022) 355–362, `doi:10.1007/s10909-022-02720-0`. 59, 70

[97] R. Brun et al., "root-project/root: v6.18/02". `doi:10.5281/ZENODO.3895860`. 59, 70

[98] J. Smith, "Introduction to Digital Filters: With Audio Applications", Music signal processing series, W3K, 2007, ISBN 978-0974560717. 64, 99

[99] T. O'Haver, "A Pragmatic Introduction to Signal Processing", 05, 2020, ISBN 979-8611266687. 80, 81

[100] C. Schwemmbauer et al., "Simulations for direct dark matter searches using ALPS II's TES detection system", *PoS* **COSMICWISPers** (2024) 055, `doi:10.22323/1.454.0055`. 94

ACKNOWLEDGMENTS

I would like to thank everyone who helped me make this thesis possible.

I am very grateful to the ALPS group for letting me be part of a great research environment. I appreciate the supervision of Axel Lindner and Erika Garutti, who guided me to complete this thesis. I would like to dedicate a special thanks to Friederike Januschek for providing guidance and support, especially during the end of my PhD, and for the constant feedback concerning this thesis.

I would like to express my gratitude to Katharina for her guidance and support at the beginning of my PhD. I greatly appreciate the help from Rikhav, which also gave me a lot of insight into the work in the lab with the TES and SQUID system. I would also like to thank the other members of the TES group: Christina, Joule, Manuel and Elmeri, for their help and support, especially at the moment I had to focus the most on writing this thesis.

I also thank my fellow Cubans in Hamburg who graduated from my same university, who gave me tons of advice and supported me along my PhD path.

I would like to thank my family for their motivation and support during my PhD studies. I especially thank my father for inspiring me to pursue a scientific career. I wish to thank Diana and Gustavo for their constant help and guidance during the PhD.

Finally, but most importantly, I would like to thank my wife, who made the PhD journey with me and has supported me even in the most difficult times. I have greatly enjoyed this journey with her and I am looking forward to what the future holds.